SPARC 2004

Contract No. 18307/04/NL/FF

SPARC Data Acquisition Report

Contents

PART II: DATA PROCESSING

PART III: DATA BASE

List of Participants

European Spatial Agency (ESA)

Malcolm Davidson
Remo Bianchi

University of Valencia - Remote Sensing Unit

Jose F. Moreno
Luis Alonso
Gloria Fernández
Juan C. Fortea
Soledad Gandia
M. Carmen González
Luis Guanter
David Moreno

Joaquin Melia
Fernando Camacho de Coca
Javier García-Haro
Beatriz Martínez
Aleixandre Verger

University of Valencia - Global Change Unit

José A. Sobrino
Juan Cuenca
Mónica Gomez
Juan C. Jiménez
Yves Julien
Guillem Sòria
Mireia Romaguera
Malena Zaragoza

University of Valencia - Solar Radiation Unit

Jose A. Martínez-Lozano
María P. Utrillas
Victor Estellés
Jose Luís Gómez
Eduardo Sañudo

University of Valencia – GPDS

Javier Calpe-Maravilla
Julia Amoros
Luis Gomez-Chova
Maria Navarro
Emilio Ribes

Juan Manual Talavera

DIELMO 3D S.L. , Valencia

Jose Carlos García

University Jaume I, Catellón

Arnaud Klaren

University of Castilla-La Mancha

Francisco J. Montero Riquelme
Antonio Brasa Ramos
Fran Montero
Sonia López Bonilla

University of Castilla-La Mancha. Institute of Regional Development (IDR), Albacete

Alfonso Calera
Eva Rubio
Jose González
Andrés Cuesta
Ángel Miranda
Nieves Sánchez

ITAP

Prudencio López Fuster
Ramón López Urrea
Amelia Montoro

Centro de Investigaciones Energéticas, Medioambientales y Tecnológicas (CIEMAT), Madrid

Manuel Pujadas
Francisco Molero
Alberto Herranz

CEDEX, Madrid

Ramón Peña
Antonio Ruiz

EEAD-CSIC, Zaragoza

Fermín Morales

INTA

Alix Fernandez-Renau

Jose Antonio Gomez
Eduardo de Miguel

Universitá degli Studi di Napoli "Federico II", Italy

Guido d'Urso
Rosaria Caterina Giorgio Gaggia
Ugo Lazzaro
Francesco Vuolo

LURE, Paris, France

Ismael Moya
Abderrahmane Ounis
Roberto Pedrós
Nicolae Moise
Yves Goulas
Juliette Louis

ALTERRA-WUR, Holland

Z. Bob Su (Alterra)
Li Jia (Alterra)
Xiaomei Jin (WU)
Jan Elbers (Alterra)
Wim Timmermans (ITC)
Ambro Gieske (ITC)
Hans van der Kwast (UU)

University of Washington, U.S.A.

Guillespie
Don Sabol

LSIIT, Strasbourg, France

F.Nerry

INRA, Avignon, France

A. Olioso

RM-CNR, Italy

Stefano Pignatti
Rosa Maria Cavalli
Cristiana Bassani

SPARC-2004
Data Acquisition Report

Overview of the campaign

The activities carried out in Barrax last summer 2004 originated from the combination of a number of initially not connected initiatives:

- Field activities in the framework of the EU projects DEMETER, EAGLE and SmartSPECTRA
- MERIS / ASAR synergy studies within an ENVISAT AO project,
- MERIS validation activities within the framework of another ESA project,
- CHRIS/PROBA acquisitions and data analysis under the framework of another initiative,
- MSG/SEVIRI validation activities under funding by EUMETSAT LSA SAF,
- Barrax as an additional site for VALERI activities,
- Background activities for vegetation fluorescence modelling and validation studies,
- Background activities for SPECTRA studies,
- Other national projects

Moreover, parallel activities related to definition of core sites for satellite validations for CHRIS and ENVISAT data have motivated the interest in getting involved in this activity by other people, with activities also related to AATSR and ASTER thermal data validation.

Most of the activities performed in the campaign are highly relevant for SPECTRA, but in particular the issues related to retrieval of biophysical parameters from CHRIS and MERIS data are of particular relevance, while scaling issues and complementary between SPECTRA (covering only local sites) and global sensors such as MERIS / SEVIRI are also key elements. Another aspect of the campaign is the use of CHRIS data to test geometric and atmospheric processing procedures to be developed for SPECTRA. CHRIS data also serves for SPECTRA simulation studies, as model-simulated Barrax scenes can be compared with actual data

The reason for the selection of the days 14th, 15th, 16th, 17th of July to carry out the campaign was the coincidence with two consecutive days of CHRIS/PROBA overpasses. Since most of the other planned activities were somehow flexible in dates (more continuous satellite overpasses) the particular orbit of PROBA was the driver in choosing the preferable dates for the campaign.

PROBA was launched in a kind of orbit that has some special features. It makes possible to have coverage over a given site for 2 or 3 consecutive days, and then several days (around 6 at the latitude of Barrax) in between where access to the site is not possible due to the orbital coverage. Each orbit provided 5 images with different view angles (-55º, -36º, 0º, +36º, +55º along-track zenith angles). Overpass times were 11:12 and 11:24 (UT) for the two days, 15-16 July respectively:

Date	Time	Minimum Satellite Zenith Angle	Solar Azimuth Angle	Solar Zenith Angle
15 July	11:12	+18	138.86	22.04
16 July	11:24	+8	145.45	20.81

Specific atmospheric measurements were planned for each PROBA overpass on each day.

For MERIS it was possible to get Full Resolution data for two days during the campaign, 14th and 17th of July:

Orbit	Track	Frame	Date	Time
12401	323	2835	2004/07/14	10:31:16
12444	366	2835	2004/07/17	10:37:01

INTA was in charge of the flights, with aircraft availability exactly for the days of CHRIS/PROBA overpass. The sensor used was INTA-AHS 80Airborne Hyperspectral Scanner.

Concerning atmospheric measurements, we launched 2 radiosounding balloons every day of the campaign, one in the early morning (to get stable atmospheric condition) and the other just at the time of satellite/aircraft overpass. The combination of radiosoundings / LIDAR / sunphotometers / high spectral resolution sky radiance measurements allowed addressing a number of issues such as:

1. Aerosols optical thickness retrievals (and other related aerosols parameters), by different methods and techniques.
2. Atmospheric correction of the satellite data, with several algorithms to be tested for CHRIS and MERIS.
3. High spectral resolution radiance measurements in the O2-A band for validation of MERIS pressure retrievals for Rayleigh corrections.

Vegetation measurements were focused on three main parameters: LAI, fCover, Chlorophyll. These three parameters were the official products being validated in the context of MERIS and SEVIRI activities. Obviously, for validation it was convenient to measure additional information about canopy architecture: canopy height, leaf size, etc. and other relevant information about phenology of each type of crop.

Radiometric measurements at the leaf and canopy levels were performed by using the several available radiometers with different fields of view and different setups. Four radiometers (two GER and two ASD) participated in the campaign, two of them mounted in adapted hoist, with angular FOV ranging from 1 to 25 degrees. Different methods to measure LAI and chlorophyll were used, as well as for fCover, including regular, hemispheric and stereoscopic digital photos.

Maps of the status of vegetation were prepared as part of the background DEMETER activities already on going, and other satellite data (Landsat) were also available as part of the DEMETER project.

Measurements of canopy fluxes and relevant variables used for modeling heat, water and CO_2 transfer inside and above canopy were collected by the Alterra Team (one of the EAGLE partners) over vineyard, bare soil, reforestation, sunflower, corn in Barrax during 12-21 July 2004. The measurements were grouped into the following categories in terms of their functions in radiative, heat, water and CO_2 fluxes modeling inside and above the canopy:

- Measurements of sensible, latent, and CO_2 fluxes together with radiation and soil fluxes will be useful to understand the characteristics of turbulent fluxes of different canopies, especially the sparse canopy, e.g. vineyard. Such data are also necessary for model validation.
- Measurements of gradients of air temperature and wind speed.
- Measurements of sunlit/shaded leaf/soil component temperatures, critical for understanding anisotropy of the thermodynamically heterogeneous canopy to be used for validation of a radiative transfer model and a convective transfer model of a 3D-canopy.
- Measurements of photosynthesis, leaf conductance and transpiration, helpful for the validation of a complete model.
- Roughness length, a dynamic parameter determining the height of momentum transfer as well as the source height of heat transfer through the relation with roughness length for heat transfer.

One of the new activities incorporated was the use of the SPARC2004 data as a "real world" test for the newly developed ESA Campaign Data Base (ESA-CDB) that will collect all the data from ESA supported field campaigns. In order to comply with the requirements of the database, the data acquired by the scientific teams must be submitted in a very specific format. Because each data set usually was composed of several measurements, and each measurement involves several variables, the organization of the data was very relevant.

PART I- Data Acquisition

1 - DESCRIPTION OF THE STUDY AREA: BARRAX

1.1. OVERALL DESCRIPTION OF THE AREA

The chosen test area for data collection is located in Barrax in the south of Spain ca. 200 km away from Valencia and ca. 20 km away from Albacete. The area around Barrax has been used for agricultural research for many years. The test area has a rectangular form and an extent of 5 km x 10 km = 50 km².

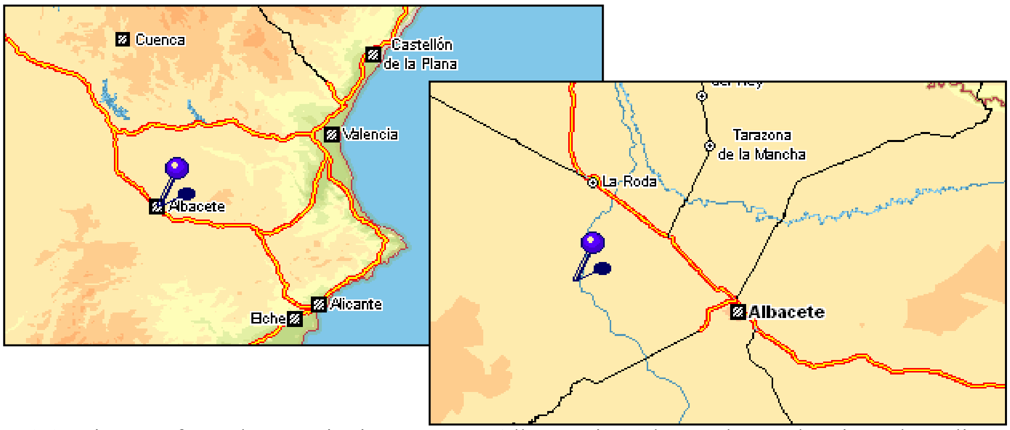

Figure 1.1. Distance from the test site in Barrax to Albacete is 20 km and to Valencia and Mediterranean ca. 200 km.

Barrax test site is situated within La Mancha, a plateau 700 m above sea level. The test site is located in the west of province of Albacete. It is 20 km far away from the capital town Albacete (coordinates 30°3' N, 2° 6' W). The area is characterised by a flat morphology and large, uniform land-use units. Differences in elevation range up to 2 m only. The regional water table is about 20-30 m below the land surface.

The climatic conditions accord the Mediterranean features: high precipitations in spring and autumn and the minimum in summer. The annual rainfall averages is about 400 mm. Furthermore, the region has high continentally with high thermal oscillations during all seasons. La Mancha represents one of the driest regions of Europe.

The region consists of approximately 65% dry land and 35% irrigated land with different agricultural fruits.

The test area has the following co-ordinates (related to UTM, Zone 30, DATUM WGS84):

Geographical corner coordinates:

Corner1: 575505.9523E 4323210.7146N
Corner2: 585226.6519E 4325555.7469N
Corner3: 575039.5028E 4325144.3194N
Corner4: 584760.2034E 4327489.3472N

Figures 1.2 and 1.3 give an impression of the test site.

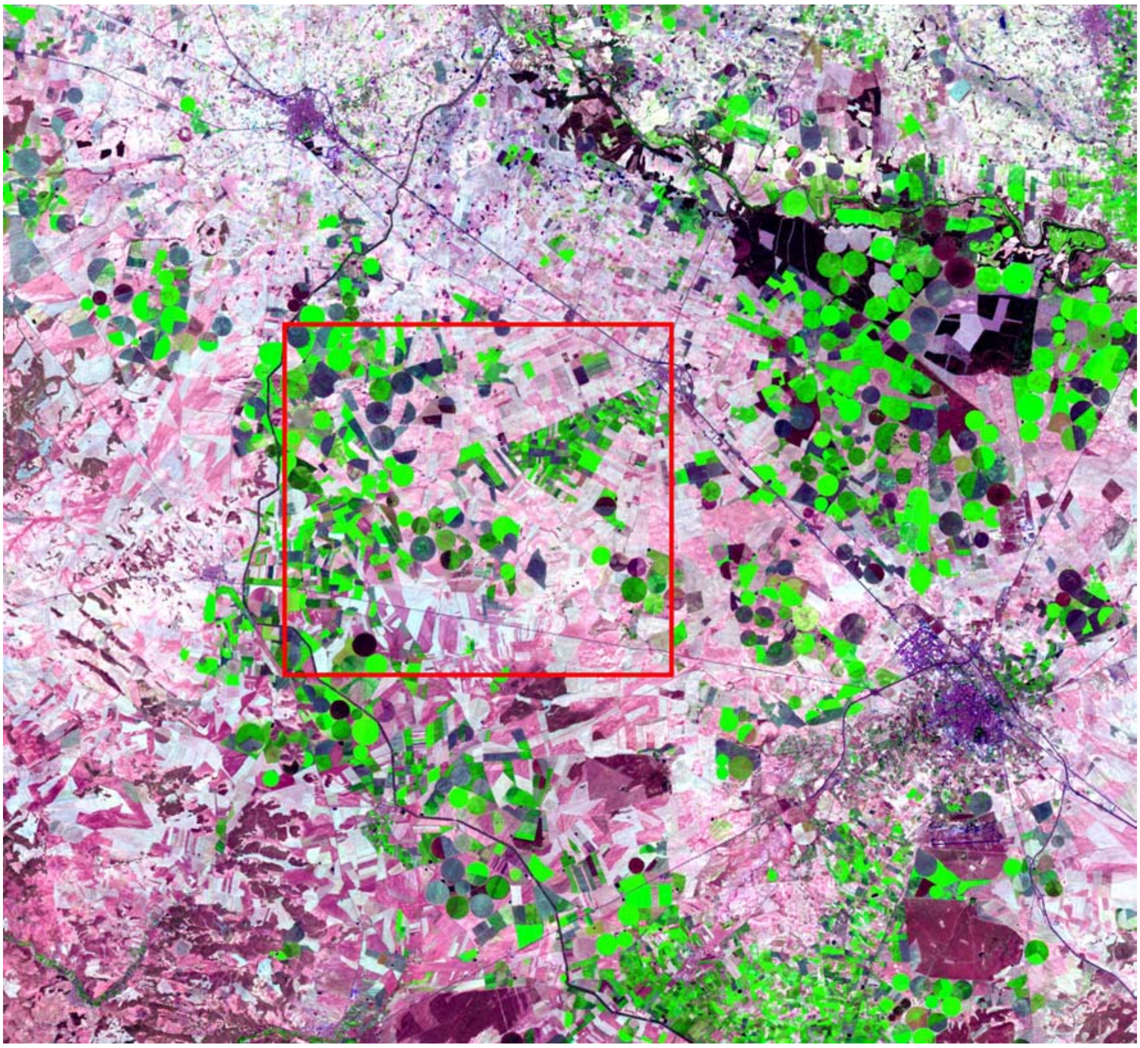

Figure 1.2. Landsat TM Satellite image of the test site in summer. Study area is shown as a red square.

(a) (b)

Figure 1.3. Test site from CHRIS-PROBA images acquired at 30/06/04: (a)VIS and (b) NIR.

1.2. PARTICULAR DESCRIPTION OF THE DIFFERENT STUDY AREAS CONSIDERED FOR DIFFERENT RESOLUTION SENSORS

The Barrax test site is included in a bigger area used in EC's DEMETER project. The DEMETER study area is defined so that it takes advantage of overlaps of coverage among different satellite orbits to get more frequently images of the area. As it can be seen in Figure 1.4, the Barrax area is in the overlap between LANDSAT reference grid images 200-33 and 199-33, what makes easier to get coverage of the area from two different satellite orbits.

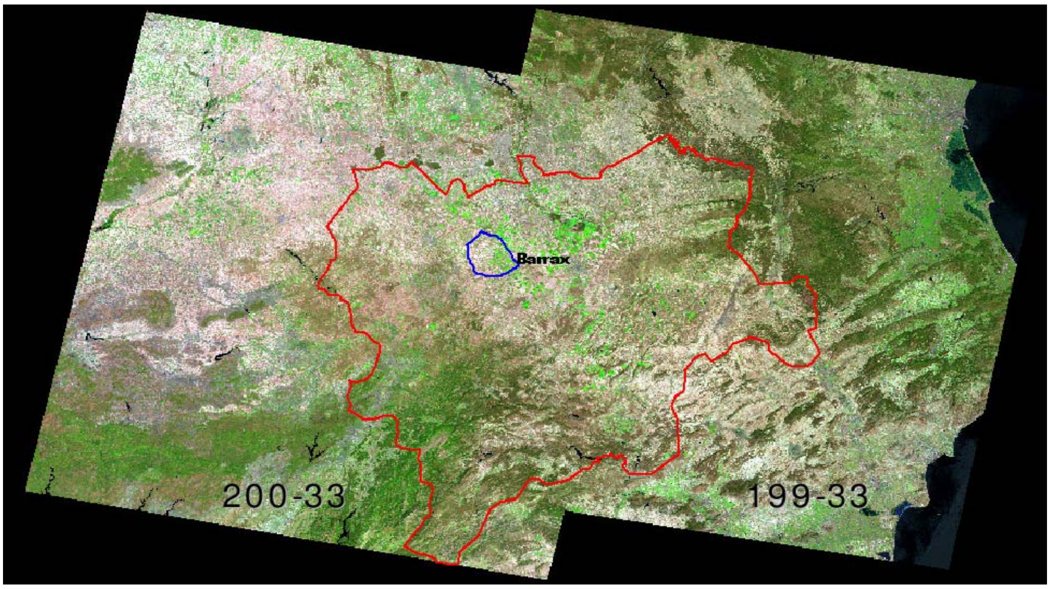

Figure 1.4. Barrax area is in the overlap between LANDSAT reference grid images 200-33 and 199-33.

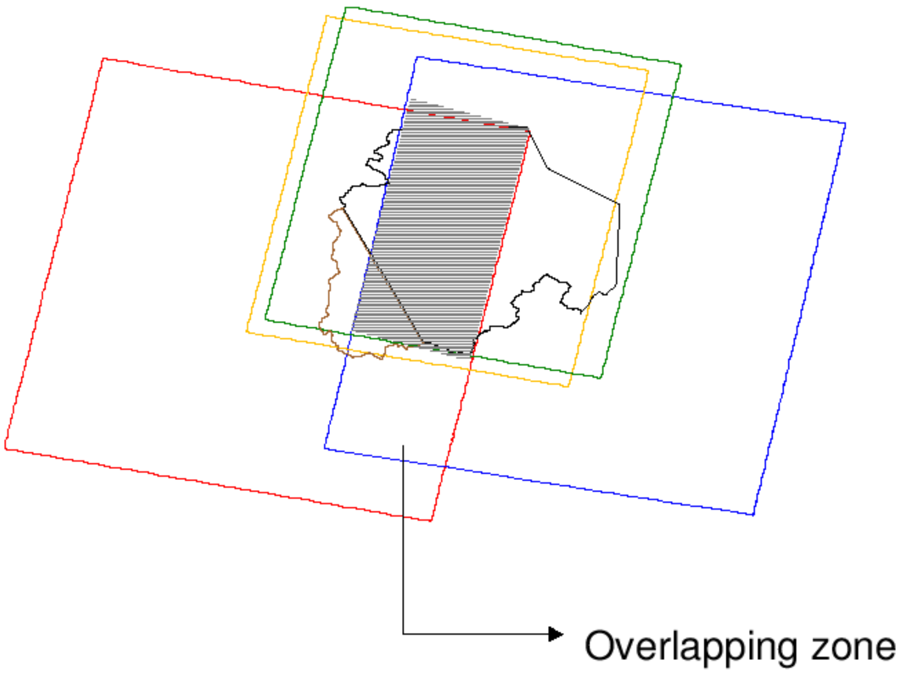

Figure 1.5. Overlapping zone from different satellite images.

When combining coverages from different satellites, an overlapping zone is defined where most intensive field activities are focused. This overlap zone is about 30 by 30 square kilometres, and is representative of the hydrological system and agricultural practices in the whole management area.

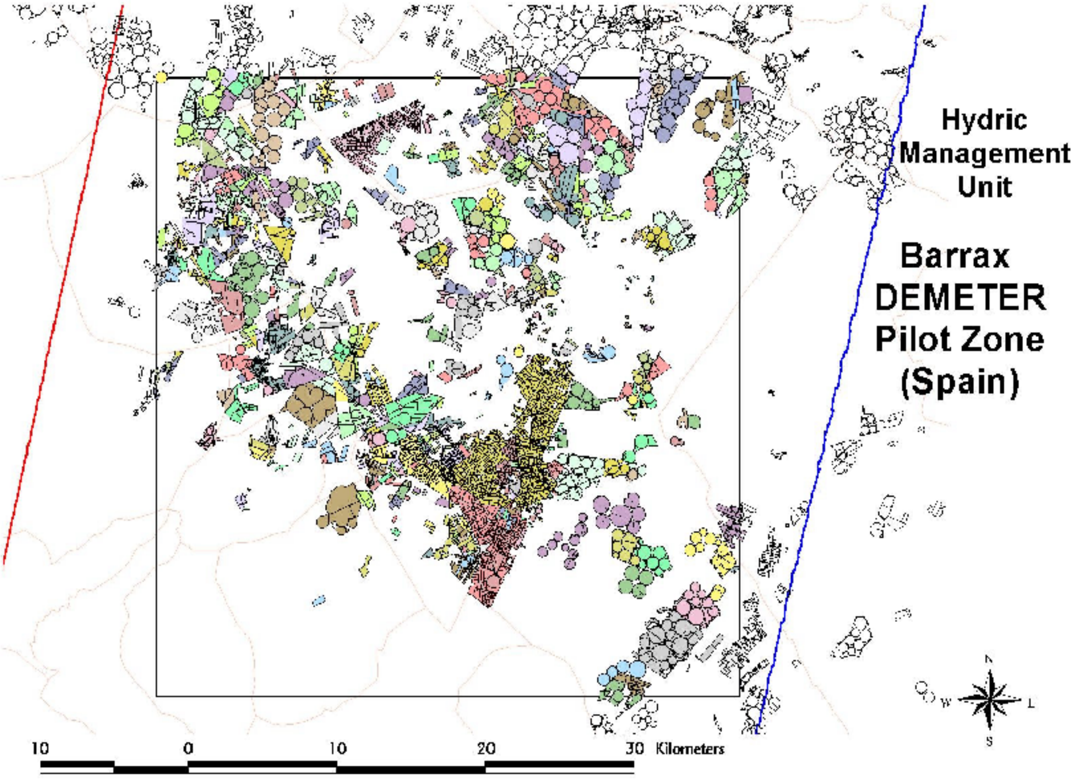

Figure 1.6. Location of the most intensive field activities.

2 - SATELLITE DATA ACQUISITIONS

2.1 CHRIS/PROBA ACQUISITIONS

CHRIS (Compact High Resolution Imaging Spectrometer) is a physically compact payload as its name implies (weighing less than 15 kg) and operates in the 'push-broom' mode. Its main applications will be in environmental monitoring, forestry inventory and precision farming.

From a 600 km orbit, CHRIS can image the Earth in a 14 km swath with a spatial resolution of 18 m (this is somewhat variable as the altitude varies around the orbit). Using PROBA's agile steering capabilities in along and across track directions enables observation of selectable targets well outside the nominal field of view of 1.3°. Images will generally be acquired in sets of 5, these being taken at along track angles of ± 55 degrees, ± 36 degrees, and as close to nadir as possible.

CHRIS operates over the visible/near infrared band from 400 nm to 1050 nm and can operate in 63 spectral bands at a spatial resolution of 36m, or with 18 bands at full spatial resolution. Spectral sampling varies from 2-3 nm at the blue end of the spectrum, to about 12 nm at 1050nm. Sampling is about 7nm near the red edge (~690-740nm). The instrument is very flexible and different sets of bands can be used for different applications.

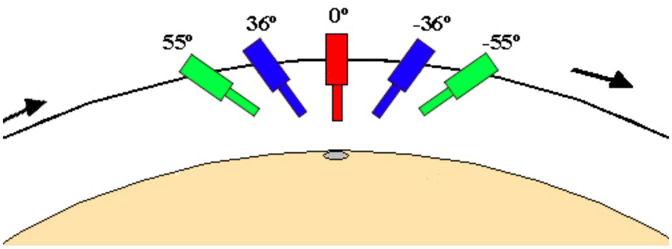

Figure 2.1. Illustration of how CHRIS can hold a target in view by using PROBA's pitch control.

Key Characteristics:

Table 2.1. Key characteristics of CHRIS/PROBA.

Spatial sampling interval	18m on ground at nadir
Image area	14 km X 14 km (748 X 748 pixels)
Number of images	Nominal is 5 downloads at different view angles
Data per image (for a 14x14 km^2)	131 Mbytes
Spectral range	410nm to 1050 nm
Number of spectral bands	19 bands at a spatial resolution of 18m 63 bands at a spatial resolution of 36m
Spectral resolution	1.3 nm @ 410nm to 12 nm @ 1050nm (i.e. it varies across the spectrum)

Programmable operation:

Across track pixel size	18m or 36m
Along track pixel size	finest resolution is 18m but can be made coarser by changing the integration time
Spectral	variable bandwidth and band location
Digitisation	12 bits
Signal-to-noise ratio	200 @ a target albedo of 0.2

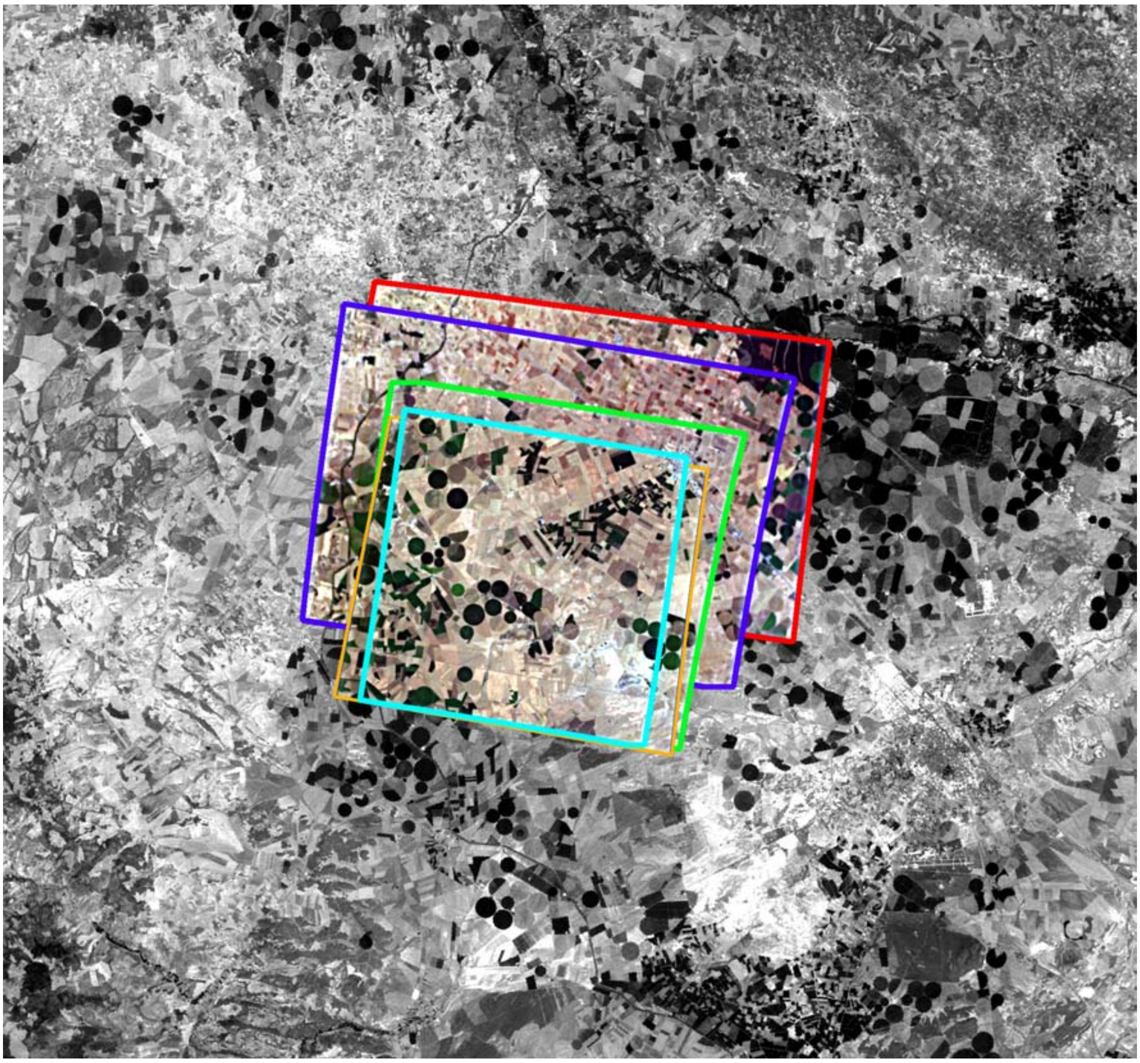

Figure 2.2. The different five CHRIS-PROBA acquired images (16/07/04) overlaped to LANDSAT image (17/07/04).

Next table shows more detailed information for each FZA corresponding to 15th and 16th PROBA acquisitions.

Table 2.2. CHRIS-PROBA acquisition programmed during the SPARC campaign.

FZA	Date	Time	Minimum Satellite Zenith Angle	Solar Azimuth Angle	Solar Zenith Angle
+55	15 July	11:11	55	138.86	22.04
+36	15 July	11:11	38	138.86	22.04
+-0	15 July	11:12	18	138.86	22.04
-36	15 July	11:13	38	138.86	22.04
-55	15 July	11:14	55	138.86	22.04
+55	16 July	11:22	55	145.45	20.81
+36	16 July	11:23	36	145.45	20.81
+-0	16 July	11:24	8	145.45	20.81
-36	16 July	11:25	36	145.45	20.81
-55	16 July	11:26	55	145.45	20.81

2.2 MERIS ACQUISITIONS

MERIS is a programmable, medium-spectral resolution, imaging spectrometer operating in the solar reflective spectral range installed on board of ESA's Earth Observation satellite ENVISAT. Fifteen spectral bands can be selected by ground command, each of which has a programmable width and a programmable location in the 390 nm to 1040 nm spectral range.

The instrument scans the Earth's surface by the so-called 'push broom' method. CCDs arrays provide spatial sampling in the across track direction, while the satellite's motion provides scanning in the along-track direction.

MERIS is designed so that it can acquire data over the Earth whenever illumination conditions are suitable. The instrument's 68.5^o field of view around nadir covers a swath width of 1150 km. This wide field of view is shared between five identical optical modules arranged in a fan shape configuration. In the calibration mode, correction parameters such as offset and gain are generated, which are then used to correct the recorded spectra. This correction can be carried out either on board or on the ground.

The Earth is imaged with a spatial resolution of 300 m (at nadir). This resolution is reduced to 1200 m by the on board combination of four adjacent samples across track over four successive lines.

The scene is imaged simultaneously across the entire spectral range, through a dispersing system, onto the CCD array. Signals read out from the CCD pass through several processing steps in order to achieve the required image quality. These CCD processing tasks include dumping of spectral information from unwanted bands, and spectral integration to obtain the required bandwidth. On-board analogue electronics perform pre-amplification of the signal and correlated double sampling and gain adjustment before digitisation. The on-board digital electronics has three major functions: it completes the spectral integration, performs offset and gain corrections in full processed mode, and creates the reduced-resolution data when required.

The calibration of MERIS is performed at the orbital south pole, where the calibration diffuser is illuminated by the sun by rotating a calibration mechanism.

The engineering requirements on the instrument, which have been derived from the ENVISAT mission requirements, are as follows:

- Spectral range: 390 nm to 1040 nm
- Spectral resolution: 1.8 nm
- Band transmission capability: Up to 15 spectral bands, programmable in position and width
- Band-to-band registration: Less than 0.1 pixel
- Band-centre knowledge accuracy: Less than 1 nm
- Polarisation sensitivity: Less than 0.3%
- Radiometric accuracy: Less than 2% of detected signal, relative to sun
- Band-to-band accuracy: Less than 0.1%
- Dynamic range: Up to albedo 1.0
- Field of view: 68.5^o
- Spatial resolution: 300 m at nadir

Figure 2.3 shows the area that was covered by the MERIS image of the days 14/07/2004 and 17/07/2004, and table 2.2 indicates the details of the acquisition.

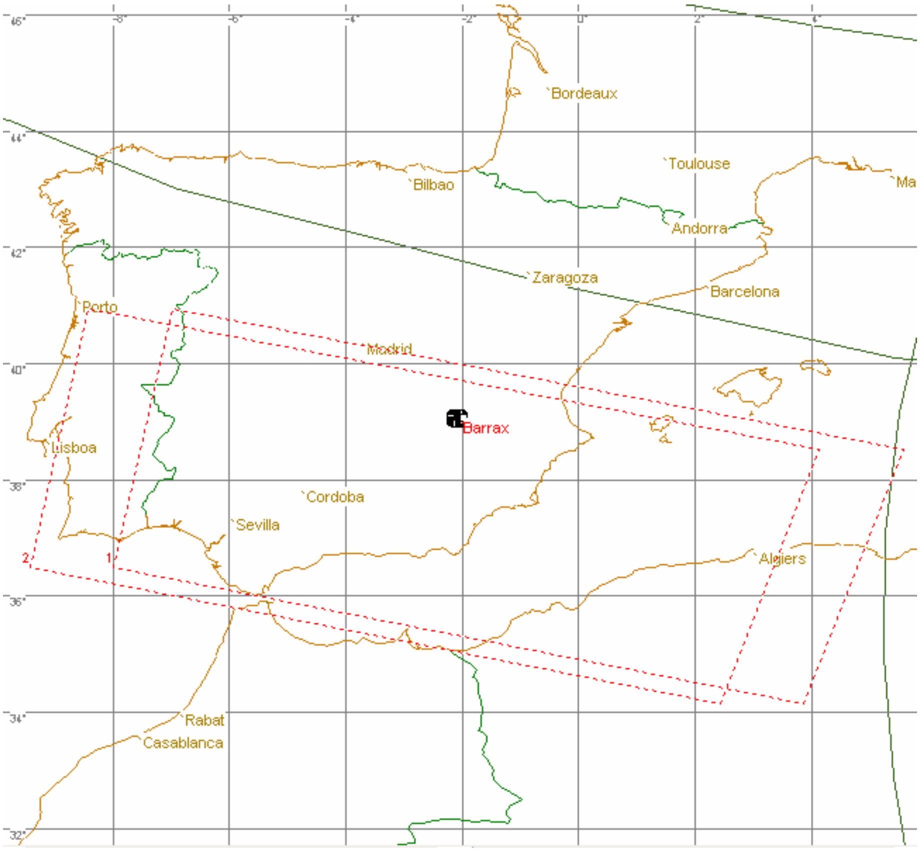

Figure 2.3. Area that will be covered by the MERIS image of the days 14/07/2003 and 17/07/2004.

Table 2.3. MERIS acquisition programmed during the SPARC-2004 campaign (in blue) and other MERIS acquisitions.

Orbit	Track	Frame	Date	Time (UT)	Solar Azimuth angle	Solar zenith angle
12344	266	2745	2004/07/10	10:55:53		
12358	280	2835	2004/07/11	10:25:31		
12401	**323**	**2835**	**2004/07/14**	**10:31:16**	**121.6º**	**27.8º**
12444	**366**	**2835**	**2004/07/17**	**10:37:01**	**124.3º**	**27.3º**
12487	409	2835	2004/07/20	10:11:10		
12501	423	2835	2004/07/21	10:42:46		

2.3 MODIS ACQUISITIONS

MODIS (or Moderate Resolution Imaging Spectroradiometer) is a key instrument aboard the Terra (EOS AM) and Aqua (EOS PM) satellites. Terra's orbit around the Earth is timed so that it passes from north to south across the equator in the morning, while Aqua passes south to north over the equator in the afternoon. Terra MODIS and Aqua MODIS are viewing the entire Earth's surface every 1 to 2 days, acquiring data in 36 spectral bands, or groups of wavelengths (see MODIS Technical Specifications). These data will improve our understanding of global dynamics and processes occurring on the land, in the oceans, and in the lower atmosphere. MODIS is playing a vital role in the development of validated, global, interactive Earth system models able to predict global change accurately enough to assist policy makers in making sound decisions concerning the protection of our environment.

The MODIS instrument provides high radiometric sensitivity (12 bit) in 36 spectral bands ranging in wavelength from 0.4 µm to 14.4 µm. The responses are custom tailored to the individual needs of the user community and provide exceptionally low out-of-band response. Two bands are imaged at a nominal resolution of 250 m at nadir, with five bands at 500 m, and the remaining 29 bands at 1 km. A ±55-degree scanning pattern at the EOS orbit of 705 km achieves a 2,330-km swath and provides global coverage every one to two days. The Scan Mirror Assembly uses a continuously rotating double-sided scan mirror to scan ±55-degrees and is driven by a motor encoder built to operate at 100 percent duty cycle throughout the 6-year instrument design life. The optical system consists of a two-mirror off-axis afocal telescope, which directs energy to four refractive objective assemblies; one for each of the VIS, NIR, SWIR/MWIR and LWIR spectral regions to cover a total spectral range of 0.4 to 14.4 µm. A high-performance passive radiative cooler provides cooling to 83K for the 20 infrared spectral bands on two HgCdTe Focal Plane Assemblies (FPAs). Novel photodiode-silicon readout technology for the visible and near infrared provides unsurpassed quantum efficiency and low-noise readout with exceptional dynamic range. Analog programmable gain and offset and FPA clock and bias electronics are located near the FPAs in two dedicated electronics modules, the Space-viewing Analog Module (SAM) and the Forward-viewing Analog Module (FAM). A third module, the Main Electronics Module (MEM) provides power, control systems, command and telemetry, and calibration electronics. The system also includes four on-board calibrators as well as a view to space: a Solar Diffuser (SD), a v-groove Blackbody (BB), a Spectroradiometric calibration assembly (SRCA), and a Solar Diffuser Stability Monitor (SDSM).

The first MODIS Flight Instrument, ProtoFlight Model or PFM, is integrated on the Terra (EOS AM-1) spacecraft. Terra successfully launched on December 18, 1999. The second MODIS flight instrument, Flight Model 1 or FM1, is integrated on the Aqua (EOS PM-1) spacecraft; it was successfully launched on May 4, 2002. These MODIS instruments will offer an unprecedented look at terrestrial, atmospheric, and ocean phenomenology for a wide and diverse community of users throughout the world.

<u>MODIS Technical Specifications:</u>

- Orbit: 705 km, 10:30 a.m. descending node (Terra) or 1:30 p.m. ascending node (Aqua), sun-synchronous, near-polar, circular
- Scan Rate: 20.3 rpm, cross track
- Swath Dimensions: 2330 km (cross track) by 10 km (along track at nadir)
- Telescope: 17.78 cm diam. off-axis, afocal (collimated), with intermediate field stop
- Size:1.0 x 1.6 x 1.0 m
- Weight: 228.7 kg
- Power:162.5 W (single orbit average)
- Data Rate: 10.6 Mbps (peak daytime); 6.1 Mbps (orbital average)
- Quantization: 12 bits
- Spatial Resolution: 250 m (bands 1-2), 500 m (bands 3-7), 1000 m (bands 8-36)

Table 2.4. Primary use, bandwidth and spectral radiance specifications for each MODIS band.

Primary Use	Band	Bandwidth[1]	Spectral Radiance[2]	Required SNR[3]
Land/Cloud/Aerosols Boundaries	1	620 - 670	21.8	128
	2	841 - 876	24.7	201
Land/Cloud/Aerosols Properties	3	459 - 479	35.3	243
	4	545 - 565	29.0	228
	5	1230 - 1250	5.4	74
	6	1628 - 1652	7.3	275
	7	2105 - 2155	1.0	110
Ocean Color/ Phytoplankton/ Biogeochemistry	8	405 - 420	44.9	880
	9	438 - 448	41.9	838
	10	483 - 493	32.1	802
	11	526 - 536	27.9	754
	12	546 - 556	21.0	750
	13	662 - 672	9.5	910
	14	673 - 683	8.7	1087
	15	743 - 753	10.2	586
	16	862 - 877	6.2	516
Atmospheric Water Vapor	17	890 - 920	10.0	167
	18	931 - 941	3.6	57
	19	915 - 965	15.0	250
Primary Use	Band	Bandwidth[1]	Spectral Radiance[2]	Required NE[delta]T(K)[4]
Surface/Cloud Temperature	20	3.660 - 3.840	0.45(300K)	0.05
	21	3.929 - 3.989	2.38(335K)	2.00
	22	3.929 - 3.989	0.67(300K)	0.07
	23	4.020 - 4.080	0.79(300K)	0.07
Atmospheric Temperature	24	4.433 - 4.498	0.17(250K)	0.25
	25	4.482 - 4.549	0.59(275K)	0.25
Cirrus Clouds Water Vapor	26	1.360 - 1.390	6.00	150(SNR)
	27	6.535 - 6.895	1.16(240K)	0.25
	28	7.175 - 7.475	2.18(250K)	0.25
Cloud Properties	29	8.400 - 8.700	9.58(300K)	0.05
Ozone	30	9.580 - 9.880	3.69(250K)	0.25
Surface/Cloud Temperature	31	10.780 - 11.280	9.55(300K)	0.05
	32	11.770 - 12.270	8.94(300K)	0.05
Cloud Top Altitude	33	13.185 - 13.485	4.52(260K)	0.25
	34	13.485 - 13.785	3.76(250K)	0.25
	35	13.785 - 14.085	3.11(240K)	0.25
	36	14.085 - 14.385	2.08(220K)	0.35

[1] Bands 1 to 19 are in nm; Bands 20 to 36 are in µm
[2] Spectral Radiance values are (W/m^2 -µm-sr)
[3] SNR = Signal-to-noise ratio
[4] NE(delta)T = Noise-equivalent temperature difference

Note: Performance goal is 30-40% better than required

MODIS acquisitions programmed for SPARC-2004 campaign:

Track	Frame	Date	Time (UT)
205	31	12-jul-04	11:36
196	32	13-jul-04	10:42
203	31	14-jul-04	11:24
194	32	15-jul-04	10:29
201	31-32	16-jul-04	11:12
192	32	17-jul-04	10:17
208	31	17-jul-04	11:54
199	32	18-jul-04	11:00
206	31	19-jul-04	11:42
197	32	20-jul-04	10:48

2.4 AATSR ACQUISITIONS:

The AATSR (Advanced Along Track Scanning Radiometer) instrument is an imaging radiometer primarily designed to measure global Sea Surface Temperature (SST) to the high levels of accuracy and stability required for climate research and modelling. Like its predecessors, ATSR 1 & 2 it will also produce high quality visible and thermal images.

AATSR is the third in the ATSR series, and is to be a payload instrument on ESA's ENVISAT-1 polar-orbiting mission (due for launch in 2000). It is primarily funded by the UK Department of Environment, Transport and the Regions (DETR) with contributions from the Natural Environment Research Council and from Australia. On behalf of the DETR, the Principal Investigator is Professor David Llewellyn-Jones of the University of Leicester.

AATSR has the same signal channels and embodies exactly the same viewing principle as ATSR-2. These are: thermal channels at 3.7, 10.8, and 12 microns wavelength; and reflected visible/near infrared channels at 0.555, 0.659, 0.865, and 1.61 microns wavelength.
The main objective of AATSR is to contribute to the long-term climate record of global Sea Surface Temperature by extending the current ATSR-1 and -2 global data-sets well into the next decade. This could eventually provide the climate research community with uniformly high quality global SST data over a period of 12-15 years (depending on the lifetime of AATSR).

Like its predecessors, ATSR-1 and ATSR-2, it will carry on-board calibration systems for the thermal channels, using two black bodies, viewed every scan, and for the visible channels a sample of solar radiation scattered from a diffuser plate is viewed once per orbit. Unlike ATSR-2 it maintains full digitisation of all channels all the time and has no limited-data-rate operating modes.

The AATSR instrument, in contrast to its predecessors (funded by SERC/NERC), is primarily funded by the DETR's Global Atmosphere Division, in order to complete a data-set of accurate global SST, lasting over ten years, which will contribute to The Climate Record and help provide quantitative assessments of possible climate change. The DETR is funding AATSR as a potential operational user of the data - the first environment ministry in Europe to take such a step - as part of a UK Government drive to direct the development and deployment of Earth Observation satellite missions more specifically towards the requirements of end-users of the data.

The ATSR (Along Track Scanning Radiometer) instruments produce infrared images of the Earth at a spatial resolution of one kilometre. The data from these instruments is useful for scientific studies of the land surface, atmosphere, clouds, oceans, and the cryosphere.
The first ATSR instrument, ATSR-1, was launched on board the European Space Agency's (ESA) European Remote Sensing Satellite (ERS-1) in July 1991, as part of their Earth Observation Programme.

An enhanced version of ATSR, ATSR-2, was successfully launched on board ESA's ERS-2 spacecraft on 21st April 1995. ATSR-2 is equipped with additional visible channels for vegetation monitoring.

The AATSR (Advanced Along Track Scanning Radiometer) instrument has been successfully launched on board the ENVISAT spacecraft on 1st March 2002 at 01:07 GMT from the Kourou spaceport in French Guiana.

AATSR programmed acquisitions:

Table 2.5. AATSR acquisition programmed during the SPARC campaign.

Orbit	Track	Frame	Date	Time (UT)
12401	323	2835	2004/07/14	10:31:16
12408	330	0765	2004/07/14	21:46:33
12444	366	2835	2004/07/17	10:37:01
12487	409	2835	2004/07/21	10:42:46

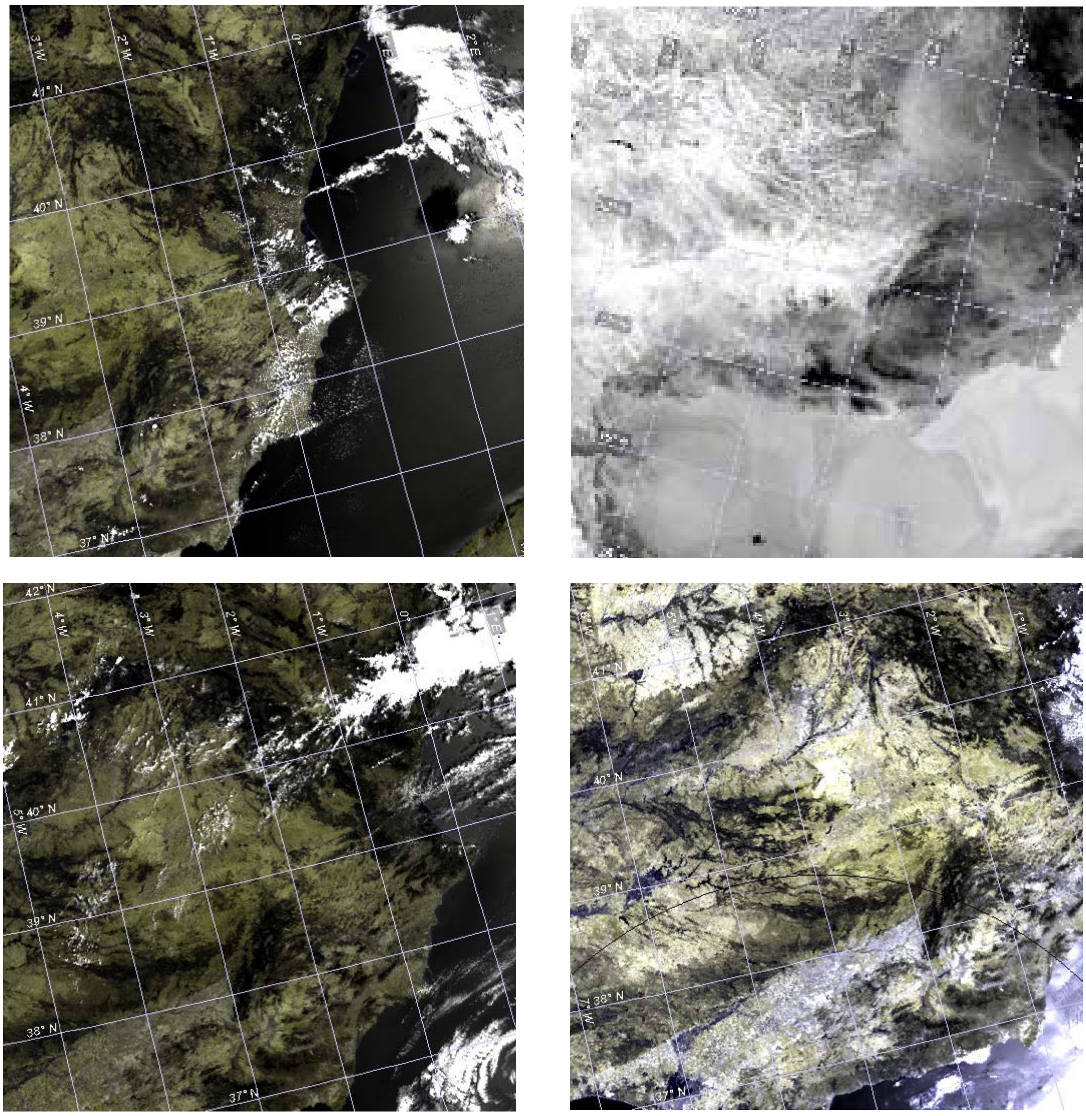

Figure 2.4. AATSR acquired images during SPARC-2004 campaign:a) VIS 14/07/04 (10:31:16 UT); b) VIS 14/07/04 .(21:46:33 UT); c) VIS 17/07/04 (10:37:01UT);d) VIS 21/07/04 (10:42:46 UT).

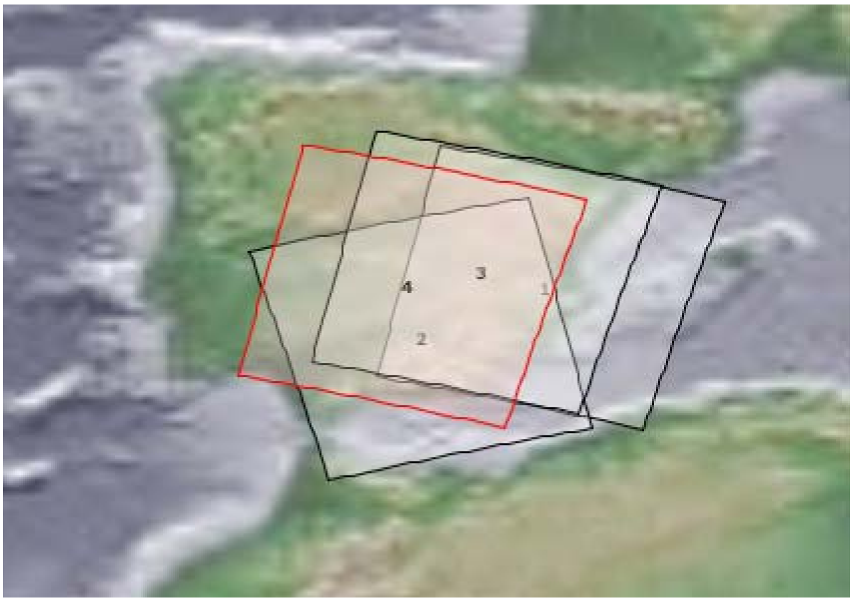

Figure 2.5. Four AATSR images were acquired over BARRAX test site during SPARC-2004 campaign.

2.5 ASTER ACQUISITIONS:

The ASTER image was acquired at 18/07/04 over the Barrax test site at 11:00 GMT. ASTER products are provided in hierarchical data format (HDF), and are defined by level:

Level 1B: at-sensor radiance (geometric and radiometric coefficients applied)
Level 2 (AST09): at-surface radiance (atmospherically corrected) in the VNIR and SWIR regions
Level 2 (AST09T): at-surface radiance (atmospherically corrected) in the TIR region
Level 2 (AST08): land surface temperature (obtained with the TES algorithm)
Level 2 (AST05): land surface emissivity (obtained with the TES algorithm)

Other level 2 products are also available, as cloud mask, decorrelation stretch, DEM, etc.

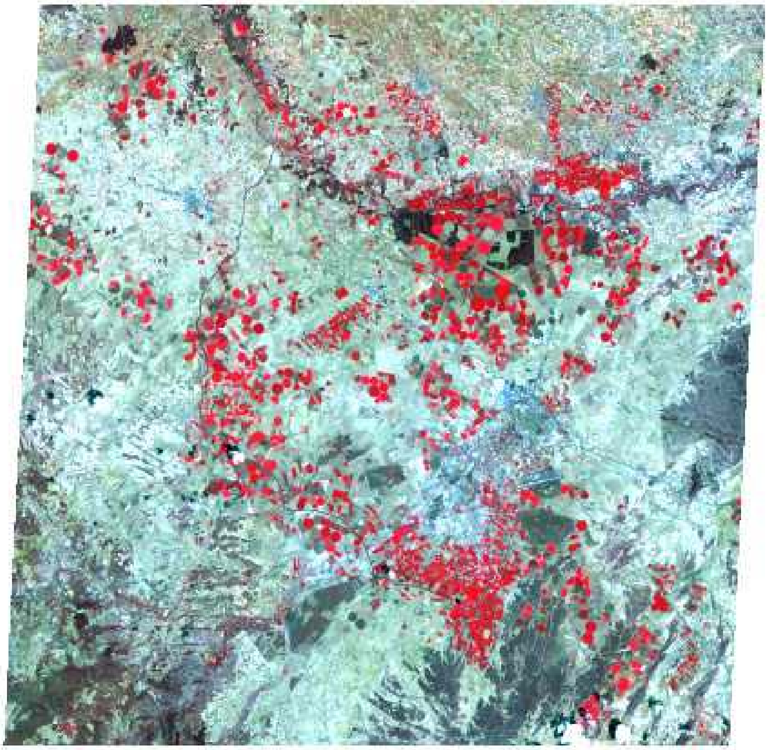

Figure 2.6. Quick look of ASTER acquired image at 18/07/04 over BARRAX test site.

2.6 SEVIRI ACQUISITIONS:

The images are received as a series of wavelet compressed segments (e.g. 8 segments for bands 1-11 and 24 segments for band 12, the High Resolution Visible, HRV). There are also Epilogue (*.epi) and Prologue files (*.pro) which contain important information with regard to the SEVIRI settings. These epilogues and prologue files are in binary format but not compressed. The compressed segment files are in fact made up of two parts: first, a header which contains information with regard to coordinates and radiometric settings and which is not compressed, and second the actual wavelet compressed image segment.

The wavelet decompression is described by Eumetsat HRIT/LRIT global and mission specific documents (Eumetsat, 1999, Eumetsat, 2001a and Eumetsat, 2001b). Processing steps for the uncompressed Native Data Format are also described in the Seviri Processing Toolbox (SPT, Govaerts and Clerici, 2004). After decompression, the segments have to be combined and provided with a coordinate and a georeference system. After that, radiometric calibration coefficients have to be used to transform the two-byte per integer pixel values into radiances. For the thermal bands 4 to 11, radiances can also be converted into brightness (top-of-the-atmosphere) temperatures using Planck's Law. Finally, subwindows may be defined for parts of the full disc (fd) scene. All these instructions are implemented in the **ShellMSG** software developed by Ambro Gieske.

The SEVIRI radiometric characteristics are displayed in Table 2.6. The noise is expressed in Signal to Noise Ratio (SNR) at a referenced target for the solar channels (MDR standing for Maximum of the Dynamic Range) and in Kelvin for the IR channels at a referenced source brightness temperature (Noise Equivalent Temperature difference or NEdT). The specified radiometric SNR or NEdT is the one between parentheses.

Table 2.6. (adapted from Aminou et al 2003). SEVIRI Radiometric specifications. ***The noise specification refers to End of Life conditions whereas the actual noise results are for Beginning of Life.

channel	**Spectral bandwidth (µm)**	**Central wavelength (µm)**	**In-Flight Radiometric Noise results** (specifications***)
HRV	Broad band -	0.6 to 0.9	**2.84** (1.20) at 0.28% of the MDR
VIS 0.6	0.56 to 0.71	0.6	**159** (10.1) at 1% of the MDR
VIS 0.8	0.74 to 0.88	0.8	**53** (7.28) at 1% of the MDR
NIR1.6	1.50 to 1.78	1.6	**10** (3.00) at 1% of the MDR
IR 3.9	3.48 to 4.36	3.9	**0.105 K** (0.35) at 300 K
WV 6.2	5.35 to 7.15	6.2	**0.05 K** (0.75) at 250 K
WV 7.3	6.85 to 7.85	7.3	**0.060 K** (0.75) at 250 K
IR 8.7	8.30 to 9.10	8.7	**0.07 K** (0.28) at 300 K
IR 9.7	9.38 to 9.94	9.7	**0.11 K** (1.50) at 255 K
IR10.8	9.80 to 11.80	10.8	**0.074 K** (0.25) at 300 K
IR12.0	11.00 to 13.00	12.0	**0.11 K** (0.37) at 300 K
IR13.4	12.40 to 14.40	13.4	**0.295 K** (1.80) at 270 K

SEVIRI pixels are sampled at 3Km (1Km HRV) at subsatellite point, and a complete image including the 12 channels, is acquired every 15 minutes.

For SPARC 2004 campaign it has been acquired images between the 10th of july to the 24th , this fact implies 96 SEVIRI images diarly acquired and a total amount of 1440 multiespectral images.

2.7 LANDSAT ACQUISITIONS:

The Landsat Project is a joint initiative of the U.S. Geological Survey (USGS) and the National Aeronautics and Space Administration (NASA) to gather Earth resource data using a series of satellites. NASA was responsible for developing and launching the spacecrafts, while the USGS is responsible for flight operations, maintenance, and management of all ground data reception, processing, archiving, product generation, and distribution.

The primary objective of the Landsat Project is to ensure a collection of consistently calibrated Earth imagery. Landsat's Global Survey Mission is to establish and execute a data acquisition strategy that ensures repetitive acquisition of observations over the Earth's land mass, coastal boundaries, and coral reefs; and to ensure the data acquired are of maximum utility in supporting the scientific objectives of monitoring changes in the Earth's land surface and associated environment.

LANDSAT-7 was launched on April 15, 1999 from the Western Test Range at Vandenberg Air Force Base on a Delta-II launch vehicle. At launch, the satellite weighed approximately 4, 800 pounds (2,200 kilograms). The spacecraft is about 14 feet long (4.3 meters) and 9 feet (2.8 meters) in diameter. It consists of a spacecraft bus, built by Lockheed Martin Missiles and Space in Valley Forge, Pa., and the Enhanced Thematic Mapper Plus (ETM+) instrument developed by Hughes Santa Barbara Research Center in Santa Barbara, CA.

The ETM+ instrument is an eight-band multispectral scanning radiometer capable of providing high-resolution image information of the Earth's surface. It detects spectrally-filtered radiation at visible, near-infrared, short-wave, and thermal infrared frequency bands from the sun-lit Earth. Nominal ground sample distances or "pixel" sizes are 49 feet (15 meters) in the panchromatic band; 98 feet (30 meters) in the 6 visible, near and short-wave infrared bands; and 197 feet (60 meters) in the thermal infrared band.
The satellite orbits the Earth at an altitude of approximately 438 miles (705 kilometers) with a sun-synchronous 98-degree inclination and a descending equatorial crossing time of 10 a.m. Landsat Worldwide Reference System will be maintained with periodic adjustments for the life of the mission. A three-axis attitude control subsystem stabilizes the satellite and keeps the instrument pointed toward Earth to within 0.05 degrees. The Landsat World-Wide-Reference system catalogues the world's landmass into 57,784 scenes, each 115 miles (183 kilometers) wide by 106 miles (170 kilometers) long. The ETM+ will produce approximately 3.8 gigabits of data for each scene, which is roughly equivalent to nearly 15 sets of encyclopedias at 29 volumes per set.

A silicon cell solar array, nickel hydrogen battery power subsystem provides 1,550 watts of load power to the satellite. A communications subsystem provides two-way communications with the ground. The command uplink and the housekeeping telemetry downlink is via s-band while all the science data is downlinked via x-band. A command and data handling subsystem provides onboard commanding, data collection, processing and storage. A state-of-the-art solid state recorder capable of storing 380 gigabits of data (100 scenes) is used to store selected scenes from around the world for playback over a U.S. ground station. In addition to stored data, real-time data from the ETM+ can be transmitted to cooperating international ground stations or to the U.S. ground station.

Orbital Characteristics

Altitude: 705 km
Inclination: sun-synchronous, 98.2 degrees
Descending Node: 10:00 a.m. (+/- 15 minute equitorial crossing time)
Repeat cycle: 16 days, 233 orbits/cycle
Period: 98.884 minutes
Argument of Perigee: 90 degress (+/- 40 degress)

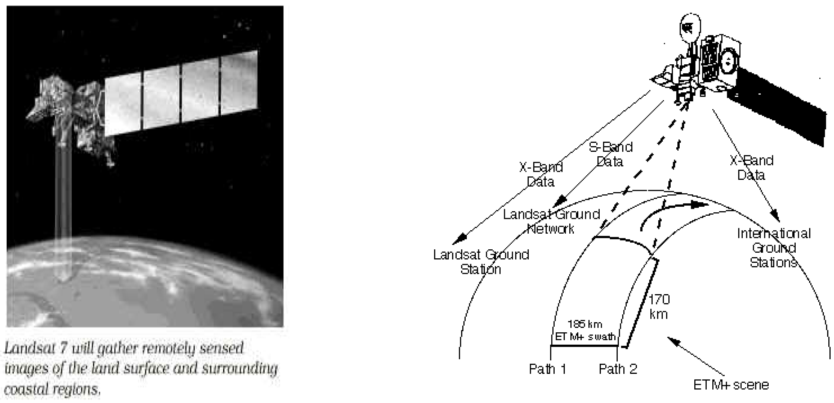

Figure 2.7. LANDSAT communication data.

Description of the ETM+ Instrument

The ETM+ instrument on the Landsat 7 spacecraft contains sensors to detect earth scene radiation in three specific bands:

1. visible and near infrared (VNIR) bands - bands 1,2,3,4,and 8 (PAN) with a spectral range between 0.4 and 1.0 micrometer.
2. short wavelength infrared (SWIR) bands - bands 5 and 7 with a spectral range between 1.0 and 3.0 micrometer.
3. thermal long wavelength infrared (LWIR) band - band 6 with a spectral range between 8.0 and 12.0 micrometer.

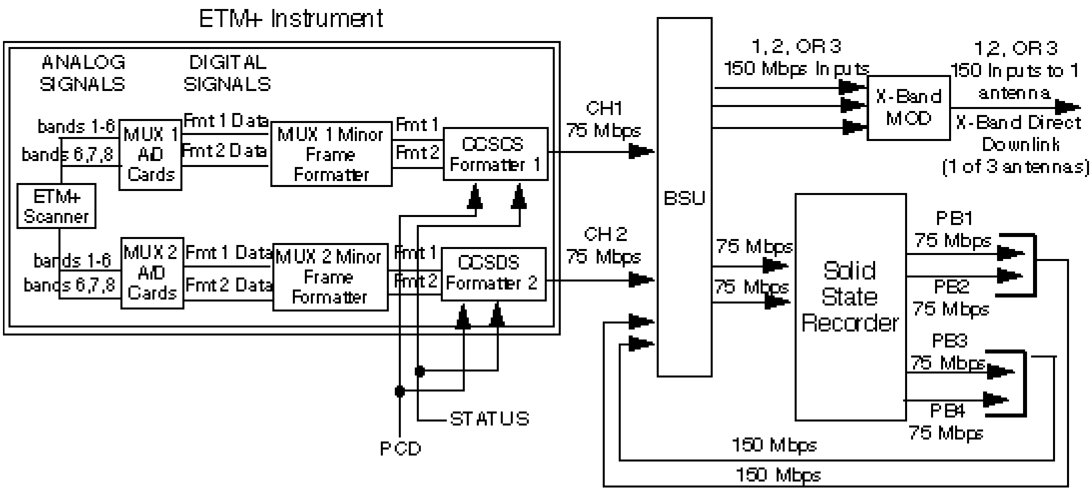

Figure 2.8.Description of the ETM+ instrument

The ETM+ scanner contains 2 focal planes that collects, filters, and detects the scene radiation in a swath, 185 km wide, as it passes over the earth. The primary focal plane consists of optical filters, detectors, and preamplifiers for 5 of the 8 ETM+ spectral bands (bands 1-4, 8). The second focal plane is the cold focal plane which includes the optical filters, infrared detectors, and input stages for ETM+ spectral bands 5,6, and 7.

Once the data is scanned, the data from the focal planes are separated into Bands 1-6 and Bands 6,7, and PAN for both multiplexers 1 and 2. Each of the two high speed multiplexers simultaneously output both scene data formats. Only one multiplexer is activated to provide the required ETM+ output data while the other remains in unpowered standby mode as selected by an external node. The Analog/Digital (A/D) converter converts the analog data to digital data which is transferred to the minor frame formatters. The MUX 1 and MUX 2 Minor frame formatters receive format 1 data and format 2 data and formats the data into the minor frame structure. The PCD status words are added and the data is BCH encoded and sent to the CCSDS formatter as format 1 and format 2. Each data stream consists of 8 bits. The CCSDS formatter then transfers the data to the Baseband Switching Unit (BSU) where it will be downlinked to the Landsat ground station or recorded on the SSR to be later downlinked.

Description of wideband data downlinked from the Satellite to the Landsat Ground System

The satellite contains the ETM+ instrument and a solid state recorder (SSR). The ETM+ instrument takes the data and separates the data into two formats. Format 1 (channel 1 also referred to as channel I contains bands 1-6 and format 2 (channel 2 also referred to as channel Q contains bands 6, 7, and 8 (PAN). Each format is transferred at 75 Mbps to a baseband switching unit (BSU) where the data is modulated and either downlinked in real-time to the Landsat Ground Station located at Sioux Falls, South Dakota, via an X-band link at a combined aggregate rate of 150 Mpbs, or recorded on the SSR. The data recorded on the

SSR can be played back using one or two 150 Mbps bitstreams and downlinked to the LGS via the X-band link. When the spacecraft flies over LGS, it downlinks two 150 Mbps data streams, either 1 real-time and 1 playback, or 2 playbacks. Therefore, when the data is transmitted to the LGS, it is a combined rate of 300 Mbps, 150 Mbps bitstreams from the ETM+ and 150 Mbps bitstreams from the SSR or two 150 Mbps bitstreams from the SSR. Once the data is received at the LGS, the data is demodulated and transmitted to the LPS as 4 physical channels. Each of the 4 channels is transferred as 75 Mbps bitstream to the LPS.

The LANDSAT image acquired within the SPARC campaign over the Barrax test site corresponds to 17/07/04.

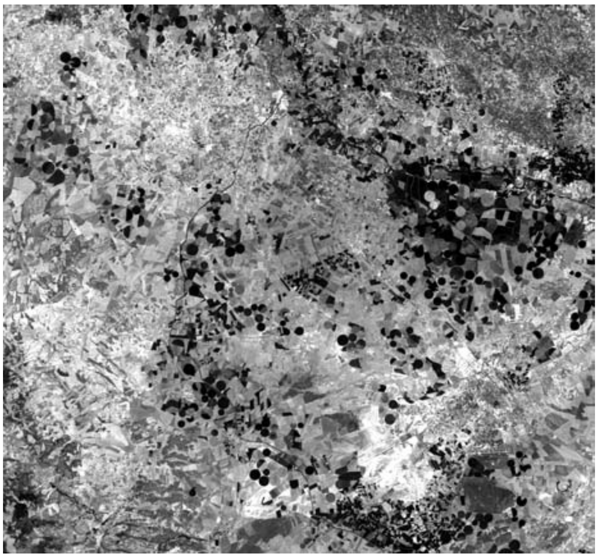

Figure 2.9.Resize of LANDSAT image acquired at 17/07/04:Barrax test site

3- AIRBONE DATA ACQUISITION

3.1 AHS (INTA)

The INTA-AHS 80Airborne Hyperspectral Scanner (AHS) is based on the integration of many advanced technologies developed by SenSyTech under R & D contracts over the past few years. While the combination of these components is offered here for the first time, each of the individual items has been delivered and field-tested in operational use. The AHS incorporates advanced components to ensure high performance while maintaining the ruggedness to provide operational reliability in a survey aircraft.

Figure 3.1. The Airborne Hyperspectral Scanner (AHS)

AHS technical specifications:

- 80 bands in 4 ports (VIS, NIR, SWIR, MWIR and LWIR)
- FOV: 90º
- IFOV: 2,5 mrad
- GFOV: 2 ÷ 6 m at 140 Kt cruise speed
- Scan Speed: 6.25, 12.5, 18.75, 25; 31.25, 35 r.p.s.
- 12 bits digitised
- 750 samples per line
- Black Body thermal references

Arrangement of spectral bands:

Table 3.1. AHS spectral bands.

Optical port	Number of bands	Spectral region	Band width
Visible and Near Infrared	20	430 to 1030 nm	30 nm
Near Infrared	1	1.550 to 1.750 µm	200 nm
Near Infrared	42	1.994 to 2.540 µm	13 nm
Mid Infrared	7	3.3 to 5.4 µm	300 nm
Long Wave Infrared	10	8.20 to 12.7 µm	400 nm

FLIGHT DATA & SENSORS SETTINGS

Aircraft	CASA 212-200 N/S 270, *"Paternina"*
Nominal aircraft ground speed	GS 140 kts (72 ms^{-1})
Altitude above ground level	AGL 975 m (3 200 ft) / AGL 2 745 m (9 000 ft)
Mean ground elevation	700 m (2 300 ft)
AHS installation	on main cabin floor back window
AMDC installation	on main cabin floor front window / on WILD PA\
IMU installation	on AMDC chassis (see note below)
WILD PAV-10 configuration	roll, yaw & pitch corrections were NOT ACTIVE drift was not compensated
AHS scan rate	35 rps (max. AHS scan rate) / 12.5 rps
AHS IFOV/FOV	2.5 mrad / 90°
AHS pixel size @nadir - GIFOV	2.5 m @ 3 200 ft AGL (max. GIFOV @140 kts) 6.86 m @ 9 000 ft AGL
AHS along-track scanline overlap	16% @ 140 kts
AHS nominal coverage	1 961 m @ 3 200 AGL / 5 491 m @ 9 000 ft A(
AHS internal thermal reference sources	T_{BB1}= 15°C & T_{BB2} = 55°C
AHS spectral configuration	Port 1+ Port 2A + Port 3 + Port 4 (Optical Port 2 was not available)
AMDC spectral configuration	B+G+R+NIR+P (5 spectral bands)
AMDC IFOV/FOV	0.3 mrad / 37.4°
AMDC diaphragm	8
AMDC shutter speed	10 ms
AMDC frame period	8 seconds
AMDC nominal coverage	660 m x 660 m @ 3 200 ft AGL 1 857 m x 1 857 m @ 9 000 ft AGL
AMDC channel shift along track	25 m (350 ms @ 140 kts)
AMDC along track overlap	13% @ 3 200 ft AGL & 140 kts (72 ms^{-1}) 69% @ 9 000 ft AGL & 140 kts (72 ms^{-1})
AMDC pixel size @ nadir - GIFOV	0.29 m @ 3 200 ft AGL 0.82 m @ 9 000 ft AGL

3.2 FLIGHTLINES COORDINATES

AHS-INTA was operated onboard a CASA aircraft. To obtain the flight coordinates we have used the overlap between the MERIS image (Figure 2.3) and the most likely expected area to be included in all the views for the different CHRIS/PROBA acquisitions during SPARC (Figure 2.2).

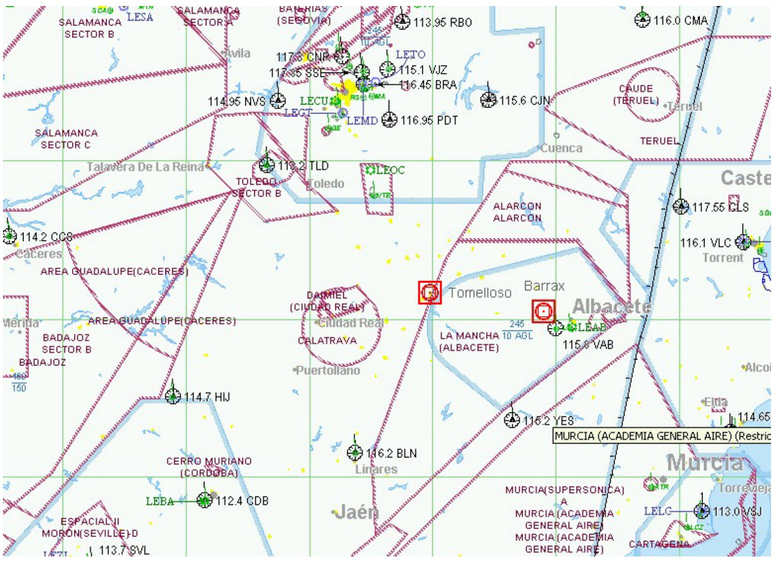

Figure 3.2. Sketch showing the use of airspace over the test area.

Figure 3.2 indicates that the test site is located in special use airspace. This Temporarily Restricted Airspace (TRA) is managed by the Spanish Airforce. INTA had to request permission for entering this airspace before each mission.

The flights took place the 15th of July 2004, at the same time as the CHRIS/PROBA acquisition (11:02), and 18th of July 2004, simultaneously to MODIS acquisition (11:00). The flights were parallel to the principal plane (in the sun direction), in order to reduce angular effects in the images. The final configurations are shown in Figures 3.3 and 3.4. The areas delimited in blue and red correspond to the overlapping areas of principal plane (red) and the perpendicular plane (blue) where the angular effects can be observed. The eight flight lines are shown in dotted green lines.

Flight lines start and ending coordinates for the programmed acquisition days (15th and 18th) reported by INTA:

FLIGHT 1 - CO-ORDINATES OF THE FLIGHT LINES CARRIED OUT ON JULY 15th 2004

	PnN ED-50 CO-ORDINATES			PnS ED-50 CO-ORDINATES		
	Easting	Northing	ZONE	Easting	Northing	ZONE
Line 1	578 117	4 328 401	30 S	572 442	4 323 476	30 S
Line 2	578 542	4 327 901	30 S	572 867	4 322 976	30 S
Line 3	578 942	4 327 451	30 S	573 267	4 322 526	30 S
Line 4	574 642	4 329 226	30 S	581 242	4 321 676	30 S
Line 5	573 317	4 328 076	30 S	579 917	4 320 526	30 S
Line 6	571 992	4 326 926	30 S	578 592	4 319 376	30 S

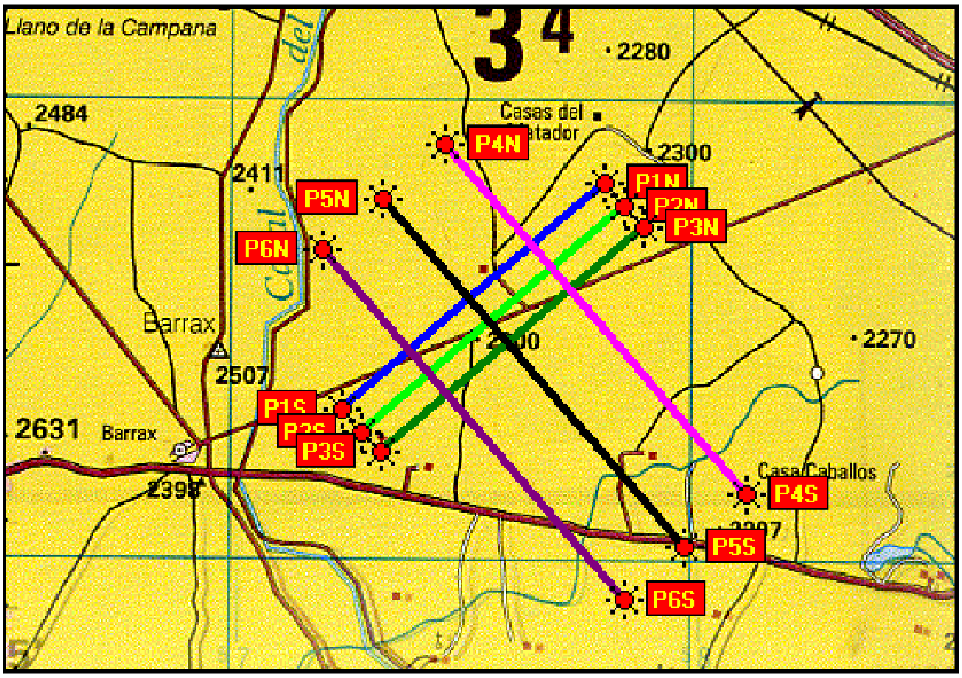

SPARC 2004 AHS FLIGHT CAMPAIGN
Flight 1 - lines at 5 500 ft & 11 300 ft MSL - July 15, 2004
Flight line sketch (E 1:250 000)
AHS sensor GIFOV = 2 5 m @ 3 200ft AGL (975 m)
GIFOV = 7 m @ 9 000 ft AGL (2 745 m)
AMDC sensor GIFOV = 0.3 m @ 3 200 ft AGL (975 m)
GIFOV = 0.8 m @ 9 000 ft AGL (2 745 m)

FLIGHT 2 - CO-ORDINATES OF THE FLIGHT LINES CARRIED OUT ON JULY 18th 2004

	PnN ED-50 CO-ORDINATES			PnS ED-50 CO-ORDINATES		
	Easting	Northing	ZONE	Easting	Northing	ZONE
Line 1	579 592	4 327 176	30 S	574 817	4 321 401	30 S
Line 2	580 092	4 326 751	30 S	575 317	4 320 976	30 S
Line 3	580 562	4 326 401	30 S	575 792	4 320 601	30 S
Line 4	573 867	4 329 301	30 S	581 592	4 322 951	30 S
Line 5-8	572 742	4 327 951	30 S	580 492	4 321 576	30 S
Line 6	571 617	4 326 601	30 S	579 367	4 320 251	30 S
Line 7	581 142	4 324 701	30 S	573 742	4 323 301	30 S

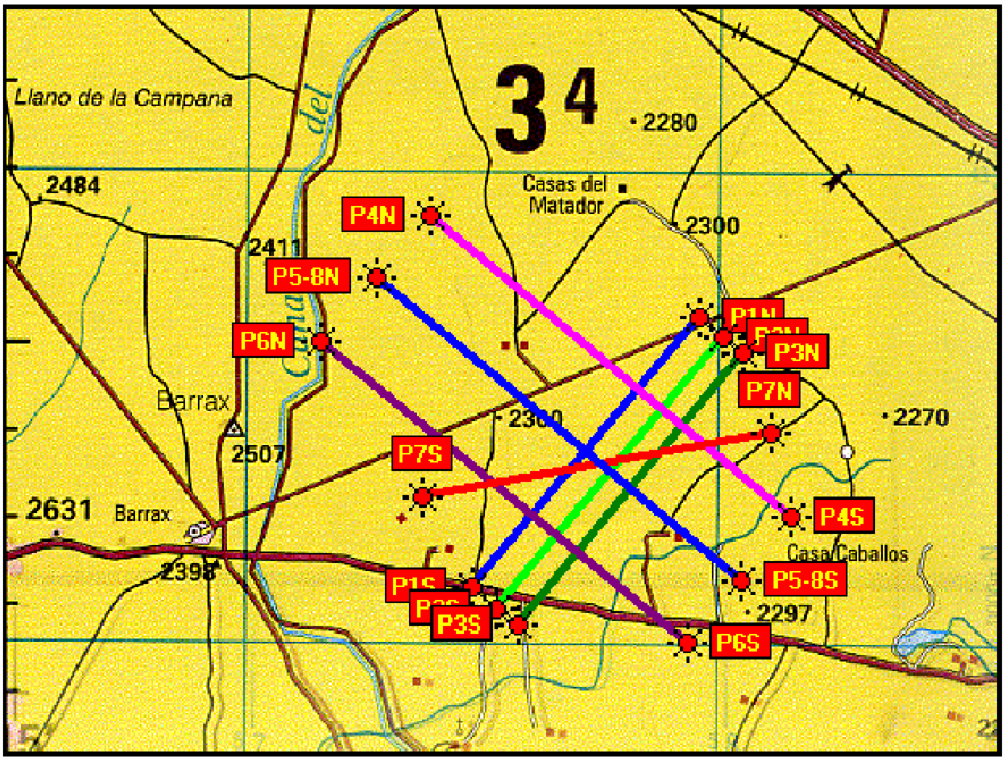

SPARC 2004 AHS FLIGHT CAMPAIGN
Flight 2 - lines at 5 500 ft & 11 300 ft MSL - July 18, 2004
Flight line sketch (E 1:250 000)
AHS sensor GIFOV = 2 5 m @ 3 200ft AGL (975 m)
GIFOV = 7 m @ 9 000 ft AGL (2 745 m)
AMDC sensor GIFOV = 0.3 m @ 3 200 ft AGL (975 m)
GIFOV = 0.8 m @ 9 000 ft AGL (2 745 m)

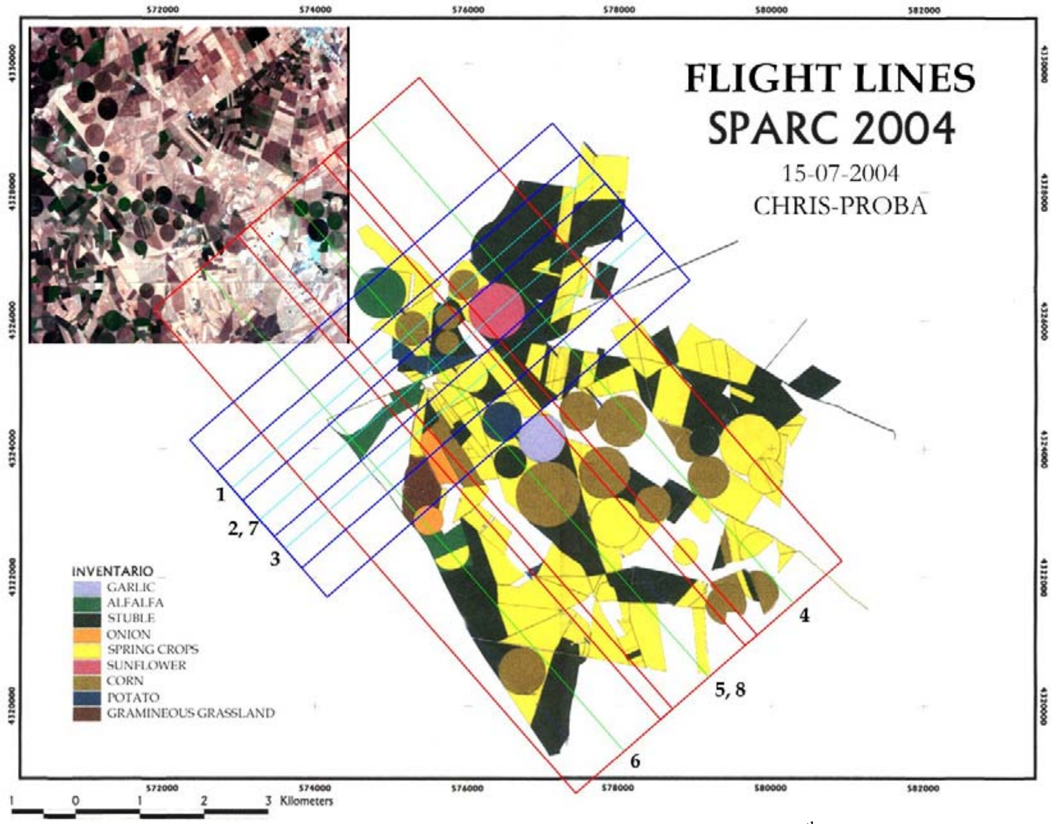

Figure 3.3. Flight configuration for SPARC campaign corresponding to the 15th of July. CHRIS-PROBA quick-look from image acquired at 30/06/04.

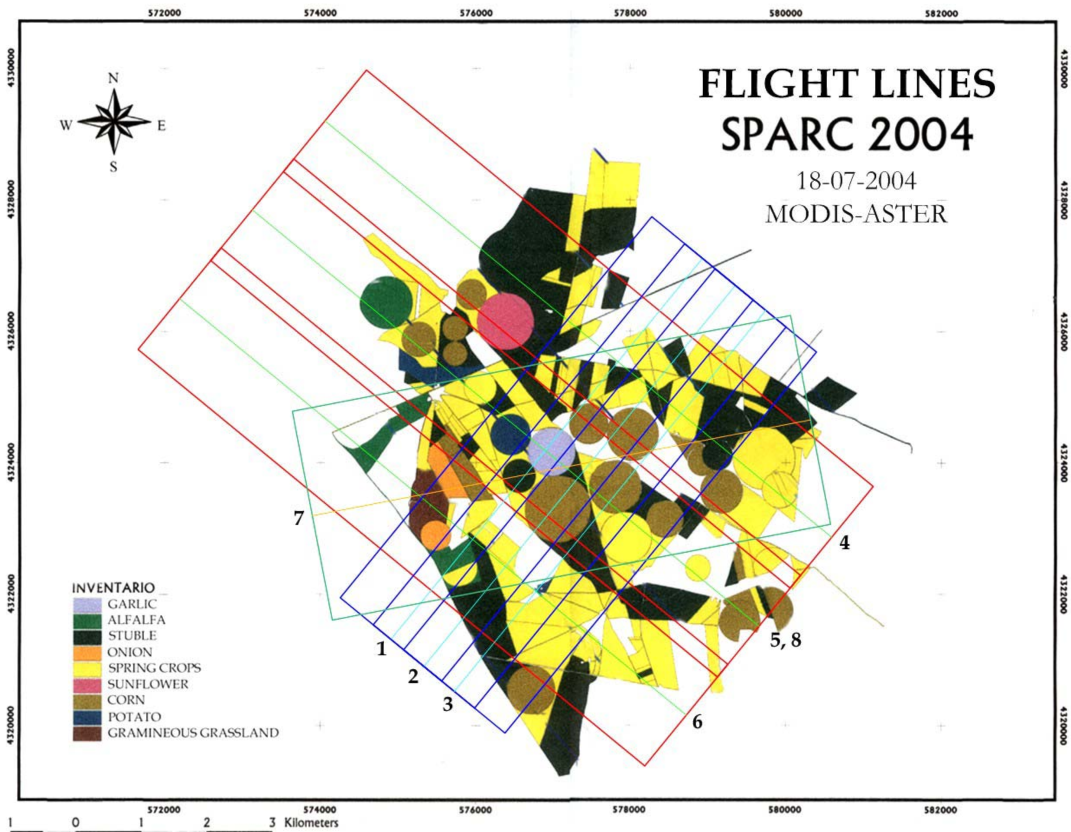

Figure 3.4. Flight configuration for SPARC campaign corresponding to the 18th of July.

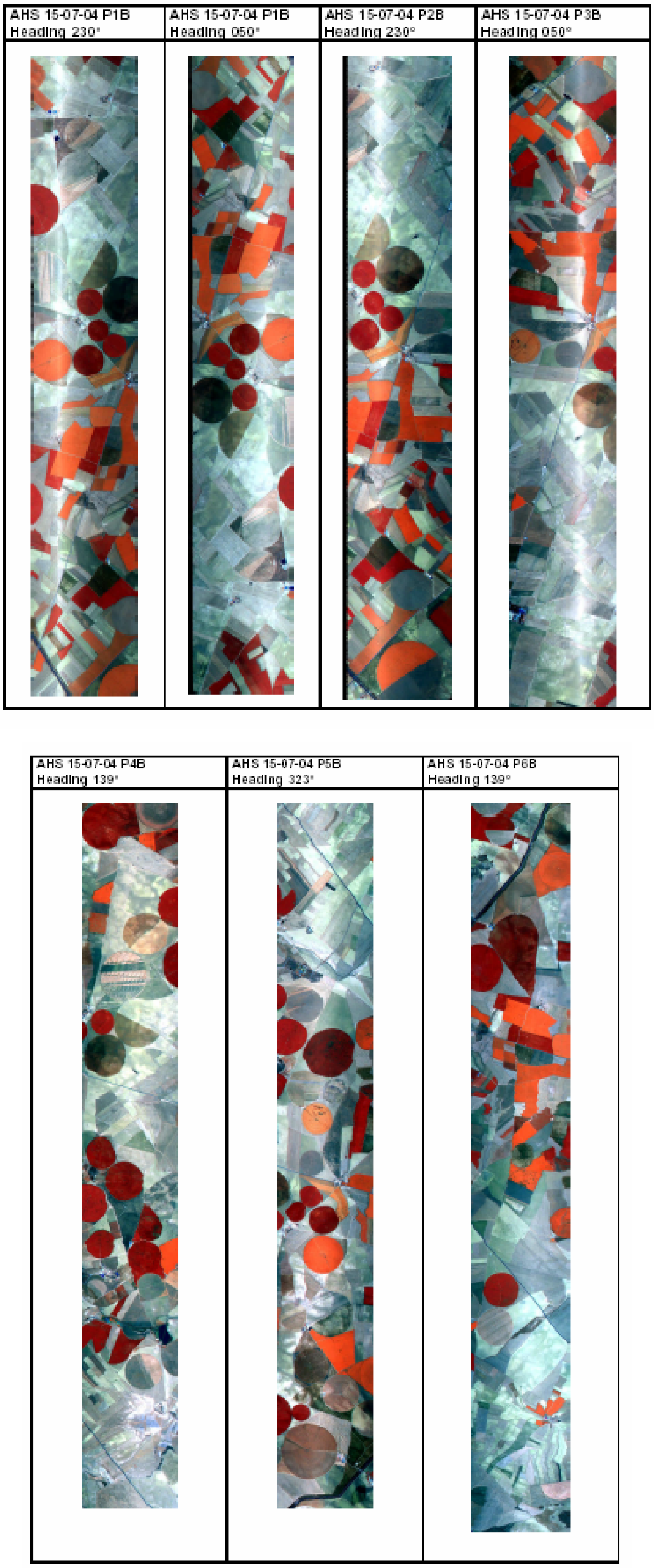

Figure 3.5. Quick looks reported by INTA
of AHS acquired images.15/07/04

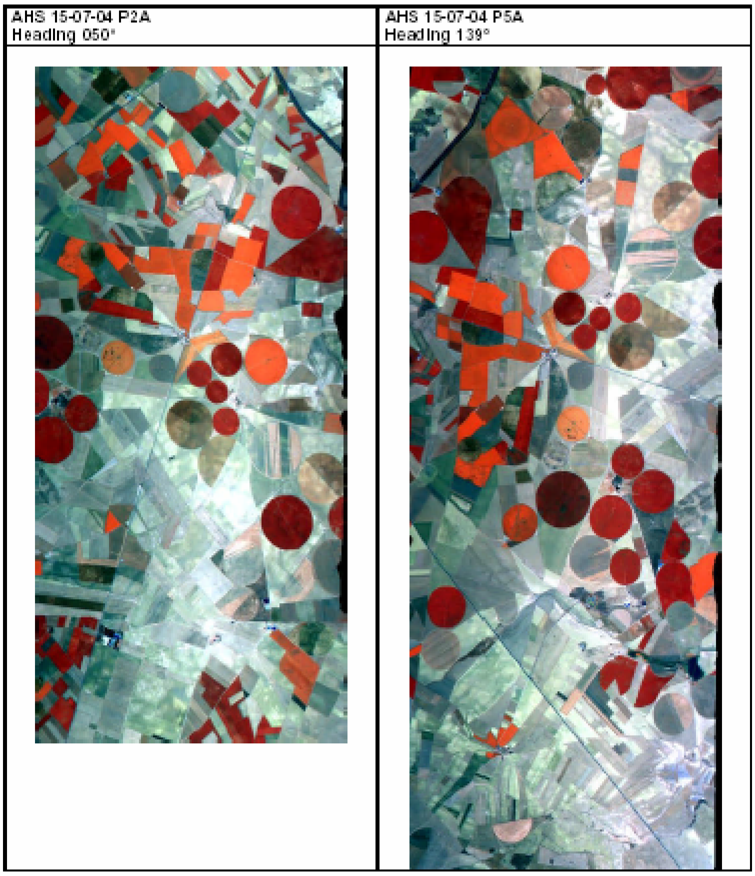

Figure 3.6. Quick looks reported by INTA
of AHS acquired images.15/07/04

4 - ATMOSPHERIC MEASUREMENTS

Aerosols and water vapor vertical profiles have been characterized at Barrax (Albacete) during the SPARC-2004. Knowledge of the atmospheric conditions, mainly the aerosol optical depth, its vertical profile and the water content, is required to perform accurate atmospheric correction of satellite imagery. Three kind of measurements were done simultaneously to the satellite overpass

a) Free atmospheric soundings,
b) Aerosol size distributions at ground level and
c) Lidar aerosol vertical profiles.

Lidar measurements are a tool to determine the diurnal evolution of the aerosols vertical structure. Changes in this structure can have some importance for the detailed atmospheric corrections of hyperspectral/multiangular data. Therefore, an evaluation of its impact on radiative transfer computations of atmospheric transmittance and radiance, as well as the implications for multiangular observations may be interesting.
In the first part of this chapter, we briefly describe each instrument and its measurement protocol. In a second part, we compare lidar profiles with radiosoundings in order to establish the atmosphere stratification and identify the mixing layer height and its aerosol loading. The water content profile was compared with the standard atmosphere models to assess the most suitable atmosphere for the atmospheric correction. A preliminary fit of the aerosol size distribution at ground level, using the four aerosol components of the 6S algorithm was attempted. Finally, we discuss the results obtained and comment about further analysis and processing of the data foreseen.

4.1 INSTRUMENTATION AND MEASUREMENTS PROTOCOLS

4.1.1 Radiosaundings

The Vaisala RS80 radiosondes are small sensors integrated in a light box and released into the atmosphere on meteorological helium filled balloons. Pressure, Temperature and Humidity are measured at regular intervals and transmitted to the surface by radio signals. The equipment was completed with a ground station AIR Inc. TS-2AR Receiver s/n 259 for the signal reception. The position of the sonde can be computed using the hydrostatic equation, which is a function of the pressure. Relative humidity is calculated with the dry and wet bulb temperatures. Wind speed and direction are not directly measured but computed by the ground equipment from the GPS information about the sonde position. Two balloons were released each day, one in the early morning before the mixing layer develops and another at the satellite overpass time, in order to characterize the precise water vapor profile in the lower layers, which change rapidly during the day due to solar heating. The coordinates of the ground station were:

Longitude: 2º 6' 10" W (UTM: 577700) Latitude: 39º 3' 44" N (4323200).

Table 4.1 summarize the exact time and duration of each radiosounding, and the precipitable water values. These were obtained by integrating between 1 and 12 km in order to compare with standard atmosphere values, which start at sea level with values each kilometer up to 100 Km. Atmospheric water vapour can be considered negligible for altitudes above 10 Km, experimentally checked by comparing the integrals up to 12 km and the complete radiosounding (~25 km).

VAISALA RS80 RADIOSONDES

SENSOR	RANGE	RESOLUTION	ACCURACY
Pressure	(3 – 1060) hPa	0.1 hPa	0.5 hPa
Temperature	(- 90 – 60) ºC	0.1 ºC	0.2 ºC
Humidity	(0 – 100) % RH	1 %	< 3%

Experimental Setup:

Figure 4.1. Radiosoundimgs experimental setup.

Table 4.1. SPARC 2004 radiosoundings and precipitable water values.

Date	Starting time (UTC)	Duration	Final altitude (gpm)	*Prec. water (g/cm^2) (1-12 km)*
13/07	16:32	68 m 32 s	25430 m	0.632
14/07	10:53	74 m 20 s	22797 m	1.313
15/07	08:16	78 m 20 s	25145 m	1.488
	10:41	78 m 50 s	25122 m	1.437
16/07	08:07	84 m 54 s	26593 m	1.599
	11:05	35 m 42 s	13731 m	1.789
	12:23	75 m 42 s	24749 m	1.710
17/07	07:49	78 m 44 s	25398 m	2.011
	10:34	74 m 54 s	25149 m	1.846
18/07	07:57	81 m 38 s	25756 m	1.539
	10:13	87 m 54 s	26786 m	1.475

4.1.2 Aerosol monitor

The aerosol distribution at ground level was measured using a laser monitor GRIMM mod. 1108, which provides particles per liter for the size fractions: 0.3, 0.4, 0.5, 0.65, 0.8, 1.0, 1.6, 2.0, 3.0, 4.0, 5.0, 7.5, 10.0, 15.0, & 20.0 µm in diameter. This is a portable system that performs particulate measurement by 90-degree laser light scattering. Air sample passes through a flat laser beam, produced by a laser diode and the scattered signals are detected by a pulse height analyzer for size classification. The measurements interval was set up to 5 minutes, providing the data summarized in the next table:

Table 4.2. SPARC 2004 laser monitor GRIMM acquired data.

Date	Time UTC	Nº files	Interval
14/07	14:04-23:56	119	5 min.
15/07	00:01-23:56	288	5 min.
16/07	00:01-23:57	286	5 min.
17/07	00:02-23:56	288	5 min.
18/07	00:01-11:02	133	5 min.

4.1.3. LIDAR system

The lidar system is a mobile equipment based on a Nd: YAG laser source (Continuum model NY82-20) operating at the 2nd harmonic (532 nm). The laser energy was 20 mJ/pulse, expanded five times and normally operated vertically when unattended (during the night) due to safety reasons.

Table 4.3. Technical characteristics of LIDAR system

Emission line	
Laser system	Nd:YAG
Wavelenght	532 o 355 nm
Energy per pulse	600 o 275 mJ
Frequency	20 Hz
Pulse width	10 ns
Beam divergence	~0.2 mrad
Beam diameter	5 cm
Detection line	
Periscope	
Azimut	0.2 mrad. 0-360º
Zenith	0.2 mrad 0-180º
Telescope	Newtonian
Diameter	300 mm
Focal length	999 mm
Field of view	1.3 mrad (selectable with iris)
PMT	Hamamatsu R928
Quantum eficiency	25 % (λ=300nm), 12% (λ=532nm)
Max. HV anode-cathode	-1250 V
Response time	2.2 ns.
Current gain	1.0 x 10^7
Range	Entre 2 y 6 Km
Spatial resolution (typical)	1.5 m - 30 m

Figure 4.2. CIEMAT Mobile laboratory carrying LIDAR and related devices.

Other instrument characteristics have been described elsewhere (F. Molero, 2000). The detection window, selectable by a pulse generator that switch the detector gain, was chosen with 1 μs delay respect to the laser fire and 20 μs duration, which produced return signals from 250 to 6000 m. These signals were range-corrected and spatially averaged to improve the signal-to-noise ratio (SNR), obtaining a range resolution of 6 m. Each signal corresponds to a temporal average of 1200 laser pulses (1 minute). The measurements protocol consists on a vertical characterization with data acquisition interval of 15-min along the five days. In the 2h-interval around the satellite overpass time, the interval was reduced to 5-min. The following table summarizes the LIDAR measurements:

Table 4.3. SPARC 2004 LIDAR measurements.

Date	Time UTC	Nº profiles	Interval	Res.	Max. range
14/07	10:47-12:07	17	5 min.	6 m	4 Km.
	12:10-21:55	40	15 min.	6 m	4 Km.
	22:10-23:40	7	15 min.	6 m	4 Km.
15/07	00:03-03:03	13	15 min.	6 m	4 Km.
	08:55-10:43	9	15 min	6 m	4 Km.
	10:52-11:56	14	5 min.	6 m	4 Km.
	11:59-23:47	48	15 min.	6 m	4 Km.
16/07	00:02-09:43	40	15 min.	6 m	4 Km.
	09:49-12:01	28	5 min.	6 m	4 Km.
	12:16-17:01	20	15 min.	6 m	4 Km.
	23:20-23:50	3	15 min	6 m	4 Km
17/07	00:05-09:45	40	15 min.	6 m	4 Km.
	09:50-11:00	15	5 min.	6 m	4 Km.
	11:02-16:41	24	15 min	6 m	4 Km.
	19:22-23:52	19	15 min.	6 m	4 Km.
18/07	00:07-10:01	41	15 min.	6 m	4 Km.
	10:04-12:14	27	5 min.	6 m	4 Km.

4.1.4 SOLAR RADIATION GROUP MEASUREMENTS

4.1.4.1 Instruments

Licor 1800 spectroradiometer:

Simple monochromator. Detector silicon photocell.

Measurement range 300-1100 nm with a bandwidth of 6 nm. Precision of 1 nm.

Accessories: Module for direct radiation measurement, FOV = 5º

Cimel CE-318 photometer:

It determines AOT for seven wavelengths and water vapour content along the atmospheric column.

Filter configuration: 340, 380, 440, 500, 670, 870, 940, 1020, 1600nm.

FOV = 1.2º

Sun photometer Microtops II:

It was conFigured to measure total ozone column, total water vapour and aerosol optical thickness at 1020 nm.

Filter configuration: 305.5, 312.5, 320, 940 and 1020 nm.

FOV 2.5º

Figure 4.3. Licor 1800 Spectroradiometer. Direct irradiance measurements

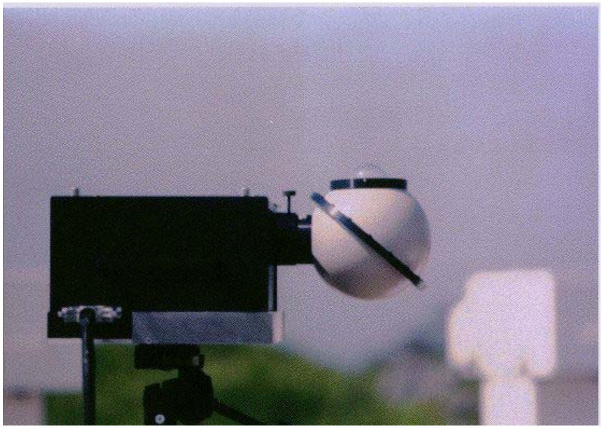

Figure.4.4 Optonic OL-754 with the integrating sphere

Figure 4.5 CIMEL 318 sunphotometer

Figure 4.6 Sunphotometer Microtops II

Table 4.4. Characteristics of the Microtops II channels

Chanel	λ (nm)	FWHM (nm)	Measurement
1	300.0±0.3	2.4±0.4	ozone content
2	305.5±0.3	2.4±0.4	ozone content
3	312.5 ±0.3	2.4±0.4	ozone content
4	940.0±1.5	10.0±1.5	water vapour
5	1020.0±1.5	10.0±1.5	aerosol optical depth

4.1.4.2 Acquired data

Measurements were done within the SPARC acquisition data campaign days (14, 15, 16, 17 and 18 of July 2004). Solar times are detailed at Table 4.5. CIMEL CE 318 instrument was measuring during the whole day from sunrise to the sunset keeping on the same schedule.

a) Available data

- Spectral global irradiance on a horizontal surface.
- Spectral direct irradiance at normal incidence.
- Spectral diffuse irradiance on a horizontal surface.
- Columnar ozone content
- Columnar precipitable water vapour content
- Aerosol optical thickness at the 1020 nm

Table 4.5. Solar time of every measurement made:

Serie	Solar time	Measurements				
		14/07/04	15/07/04	16/07/04	17/07/04	18/07/04
1	7:45	A, B, C				
2	8:00	A, B, C, D	A, B, C, D	A, B, C, D		A, B, C, D, E
3	8:15	A, B, C	A, B, C	A, B, C	A, B, C, E	A, B, C, E
4	8:30	A, B, C	A, B, C	A, B, C	A, B, C, E	A, B, C, E
5	8:45	A, B, C	A, B, C	A, B, C	A, B, C, E	A, B, C, E
6	9:00	A, B, C, D	A, B, C, D	A, B, C, D	A, B, C, D, E	A, B, C, D, E
7	9:15	A, B, C	A, B, C	A, B, C	A, B, C, E	A, B, C, E
8	9:30	A, B, C	A, B, C	A, B, C	A, B, C, E	A, B, C, E
9	9:45	A, B, C	A, B, C	A, B, C, E	A, B, C, E	A, B, C, E
10	10:00	A, B, C, D	A, B, C, D	A, B, C, D, E	A, B, C, D, E	A, B, C, D, E
11	10:15	A, B, C	A, B, C	A, B, C, E	A, B, C, E	A, B, C, E
12	10:30	A, B, C	A, B, C	A, B, C, E	A, B, C, E	A, B, C, E
13	10:45	A, B, C	A, B, C	A, B, C, E	A, B, C,	A, B, C,
14	11:00	A, B, C, D	A, B, C, D	A, B, C, D, E	A, B, C, D, E	A, B, C, D, E
15	11:15	A, B, C	A, B, C	A, B, C, E	A, B, C, E	A, B, C, E
16	11:30	A, B, C	A, B, C	A, B, C, E	A, B, C, E	A, B, C, E
17	11:45	A, B, C	A, B, C	A, B, C, E	A, B, C, E	A, B, C, E
18	12:00	A, B, C, D	A, B, C, D	A, B, C, D, E	A, B, C, D, E	A, B, C, D, E
19	12:15	A, B, C	A, B, C	A, B, C, E	A, B, C, E	
20	12:30	A, B, C	A, B, C	A, B, C, E	A, B, C, E	
21	12:45	A, B, C	A, B, C	A, B, C,	A, B, C, E	
22	13:00	A, B, C, D	A, B, C, D	A, B, C, D, E	A, B, C, D, E	
23	13:15	A, B, C	A, B, C	A, B, C, E	A, B, C, E	
24	13:30	A, B, C	A, B, C	A, B, C, E	A, B, C, E	
25	13:45	A, B, C	A, B, C	A, B, C, E	A, B, C, E	
26	14:00	A, B, C, D	A, B, C, D	A, B, C, D, E	A, B, C, D, E	
27	14:15	A, B, C	A, B, C	A, B, C, E	A, B, C, E	
28	14:30	A, B, C	A, B, C		A, B, C, E	
29	14:45	A, B, C	A, B, C		A, B, C, E	
30	15:00	A, B, C, D	A, B, C, D		A, B, C, D, E	
31	15:15	A, B, C	A, B, C		A, B, C, E	
32	15:30		A, B, C		A, B, C, E	
33	15:45		A, B, C		A, B, C, E	
34	16:00		A, B, C, D		A, B, C, D, E	

A: Licor Li-1800 spectral direct irradiance. Range [300, 1100] nm @ 1 nm

B: Licor Li-1800 spectral global irradiance. Range [300, 1100] nm @ 1 nm

C: Cimel CE-318 direct sun measurements.

D: Cimel CE-318 sky radiance measurements on almucantar plane.

E: Microtops II: 1020 nm aerosol optical depth at 1020nm, columnar ozone content, columnar precipitable water vapour content

The different solar radiation components are shown in Figure 4.7, as an example of some of the acquired measurements. The first one corresponds to 14/07/04 and shows a lowest contribution of the diffuse component (10.8%) than the 18/07/04 (19.1%). This increasing of the diffuse component is mainly related to the aerosols effect.

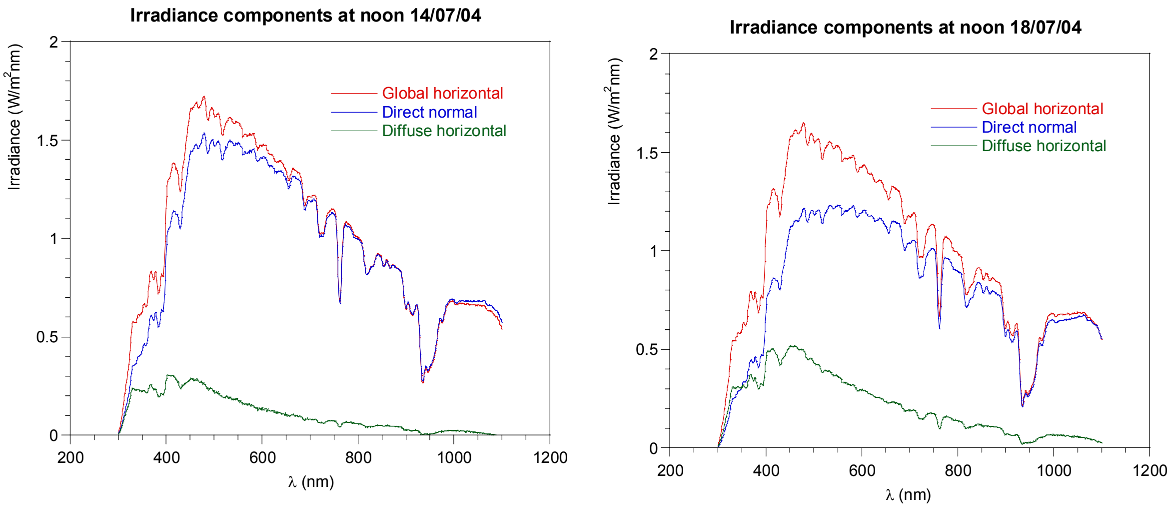

Figure 4.7. Irradiance components at solar noon on 14/07/04 and 18/07/04

The atmospheric components, ozone and water vapour, were characterized by its columnar content and aerosols by its optical thickness at 1020 nm (Figures 4.8-4.10).

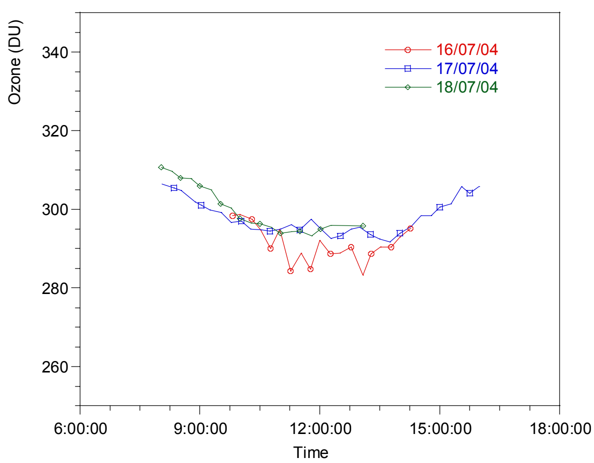

Figure 4.8. Columnar Ozone content along the campaign

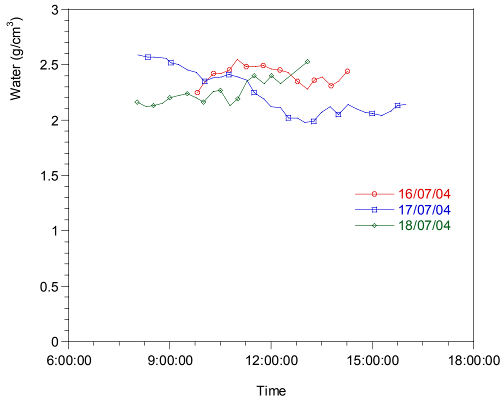

Figure 4.9. Columnar water vapour content along the campaign

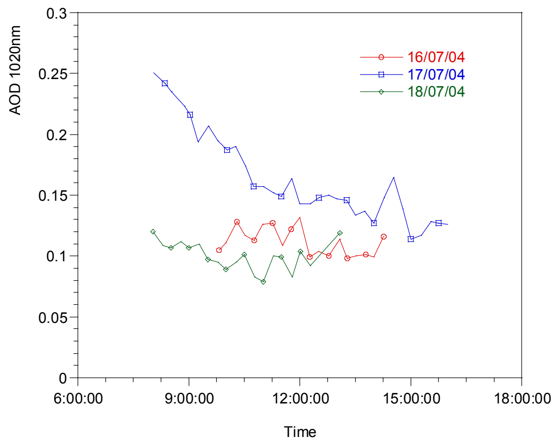

Figure 4.10. AOT at 1020nm along the campaign

4.1.5 CNR IIA LARA & IMAA MEASUREMENTS

Assessments of water vapour columnar content and Aerosol Optical Thickness from FieldSpec Pro FR solar direct irradiance measurements.

The aim of the work carried on by the CNR IIA LARA and IMAA is to estimate the Water Vapour Columnar Content (WVCC) and the Aerosol Optical Thickness (AOT) as function of wavelength (λ) through solar direct irradiance measurements from a ground-based spectrometer. The objective is to provide precise assessments of WVCC and AOT to be both used as input parameters of the radiative transfer code applied for the image atmospheric correction or to validate the WVCC and AOT values obtained from the image itself. Another aspect of their estimation is to validate the results of atmospheric models used for atmospheric corrections.

4.1.5.1 Instruments

FielSpec Pro FR

During Barrax campaign the portable ASD FieldSpec Pro FR was used to acquire the direct component of the solar spectral irradiance in the range of 350 - 2500nm. In order to orient the irradiance collector towards the sun, the irradiance measurements were performed mounting the fore-optics on a motored equatorial tripod (Figure 4.11) to track the sun throughout the day. The foreoptics used were the Remote Cosine Receptor (RCR), on which a direct irradiance probe was mounted for limiting the angular Field-of-View (FOV) of the irradiance receptor. The FOV chosen for the Barrax campaign was 1.0°.

Figure 4.11 FieldSpec spectrometer conFigured for the solar direct irradiance measurements mounted on the equatorial device. The white probe in the Figure shows the sun collimator ending with the FOV of 1.0º.

4.1.5.2 Acquired data

Ground-based atmospheric solar direct irradiance (Figure 4.12) measurement was carried out from the 15th to the 18th of July, 2004. Units of measurements of ASD irradiance are $W/m^2 nm$.

The ASD (Figure 4.11) was positioned at the atmospheric test site where CIMEL, LICOR and MICROTOPS had been already set up. Data were collected during sunrise/sunshine time, about every 15 minutes or more frequently if necessary. Most of the ASD measurements were acquired at the same time of those taken by CIMEL, LICOR and MICROTOPS.

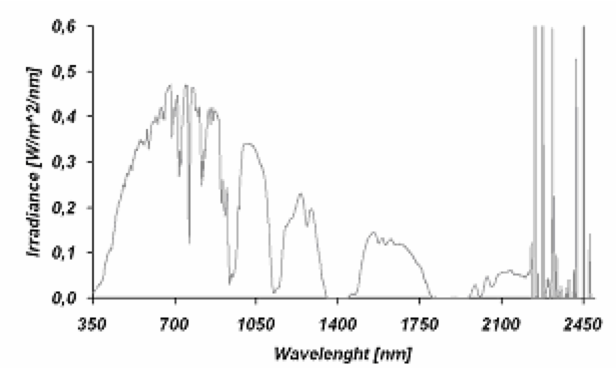

Figure 4.12: Example, ASD solar direct irradiance acquired in Barrax.

Water Vapour Columnar Content

The precipitable water vapour column u_s was assessed from the ASD irradiance measurements by using the Split Window technique applied to the 890, 936nm wavelength. The following formula was applied to spectral irradiance to obtain u_s :

$$1/u_s = a \cdot \left[R_{890nm} / \left(R_{890nm} - R_{936nm}\right)\right] + b \cdot \left[R_{936nm} / \left(R_{890nm} - R_{936nm}\right)\right]$$

Where R_{890nm} is the irradiance in atmospheric window region and R_{936nm} in water vapour absorption band, while a and b are coefficients to be estimated from a multiple regression analysis conducted on the n synthetic R_λ obtained from n MODTRAN simulation.

Both coefficients were then employed to assess the WVCC from each ASD irradiance measurements. A comparison was made between the MICROTOPS WVCC values and the data obtained from the ASD, both simultaneously taken. The WVCC by the ASD Split Window was generally estimated lesser than the one measured with the MICROTOPS. The differences varying till few percent up to 10%.

The difference (Table 4.6) was calculated through the relationship:

$$Percent = 100 * \left(u_{sMIC} - u_{sASD} / \left(u_{sMIC} + u_{sASD} / 2\right)\right)$$

Where u_{sMIC} is the water vapour measured with MICROTOPS and u_{sASD} estimated with Split Window method applied to ASD irradiance.

Table 4.6: Difference between ASD results and MICROTOPS measures

sample [#]	MICROTOPS [cm]	SPLIT WINDOW [cm]	Percent [%]	sample [#]	MICROTOPS [cm]	SPLIT WINDOW [cm]	Percent [%]
1	2.59	2.51	3	24	2.12	2.16	2
2	2.57	2.46	4	25	2.05	2.16	5
3	2.57	2.45	4	26	2.14	2.20	2
4	2.56	2.41	5	27	2.14	2.21	3
5	2.52	2.39	5	28	2.07	2.22	7
6	2.50	2.35	5	29	2.04	2.25	10
7	2.45	2.34	4	30	2.03	2.28	12
8	2.43	2.32	4	31	2.13	2.31	8
9	2.35	2.27	3	32	2.14	2.34	9
10	2.38	2.27	4	33	2.16	2.41	11
11	2.39	2.25	5	34	2.12	2.37	11
12	2.41	2.24	7	35	2.13	2.34	10
13	2.39	2.23	6	36	2.15	2.32	7
14	2.36	2.22	6	37	2.20	2.31	4
15	2.25	2.20	2	38	2.22	2.28	2
16	2.19	2.17	0	39	2.24	2.26	0
17	2.12	2.15	1	40	2.20	2.23	1
18	2.11	2.15	1	41	2.26	2.21	2
19	2.02	2.12	5	42	2.27	2.20	3
20	2.02	2.13	5	43	2.13	2.15	0
21	1.98	2.13	7	44	2.19	2.16	1
22	1.99	2.13	7	45	2.35	2.18	7
23	1.99	2.15	7	46	2.33	2.17	6

Aerosol Optical Thickness

Sun irradiance R_λ received at ground level by a surface normal to the sun's rays at wavelength λ is expressed by:

$$R_\lambda = R_{0\lambda} T_{R\lambda} T_{O\lambda} T_{N\lambda} T_{a\lambda}$$

where $R_{0\lambda}$ is extra-terrestrial irradiance (TOA) obtained from MODTRAN conFigured according to the Barrax day of measurement. The T other factors present in equation correspond to the transmittance values for different extinction processes: Rayleigh scattering (*R*), absorption by ozone (*O*), nitrogen dioxide (*N*) and aerosol (*a*) extinction.
Transmittance terms of equation are controlled by the Bouguer's law:

$$T_{i\lambda} = e^{-m_i \tau_i}$$

where m_i is the refracted path length through the atmosphere (or air mass) at the time of measurement, and τ_i is optical thickness for *ith* constituent of equation (*i* = *R*, *O*, *N*, *a*).
The AOT is retrieved by solving equation for any ASD irradiance R_λ :

$$\tau_{aer\lambda} = \left(1/m_{aer\lambda}\right)\left[\ln\left(R_\lambda / R_{0\lambda}\right) - m_{NO_2\lambda}\tau_{NO_2\lambda} - m_{O_3\lambda}\tau_{O_3\lambda}\right]$$

Figure 4.13 shows time series of $\tau_{aer\lambda}$ retrieved from ASD irradiance, for July 18, calculated on the CIMEL wavelengths.

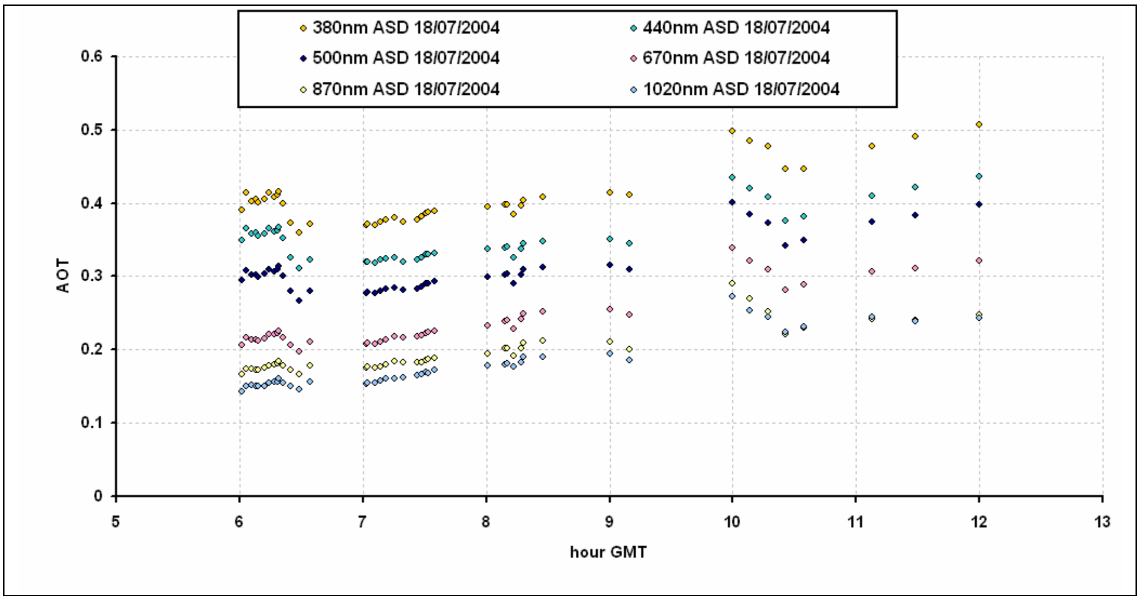

Figure 4.13. Time series (July 18, 2004) of spectral AOT derived from irradiance acquired with the ASD spectrometers. The plot shows the AOT(λ) variations with time.

4.2 EXPERIMENTAL RESULTS

The meteorological analysis of the period between 14th and 18th of July 2004, based on the INM synoptic charts, shows a synoptic situation governed by a thermal low system located over the Iberian Peninsula. During these thermal low episodes, winds are normally weak, mainly ageostrophic and driven by orography. This situation favours an inward flow from the coast toward the interior of the Peninsula, which permits the incoming of Saharan air masses, as it has been previously described (Millan, 1991). The situation changed on the 16th, with rain showers in the evening and different visibility conditions in the following days. This is shown in Figure 4.14, a color-coded plot of the range-corrected signal profiles obtained by interpolating all the measurements. The horizontal axis represents time and the vertical axis is height above ground level. The color represents the intensity of the range-corrected lidar signals in arbitrary units. The red spots on the 16th evening and 17th morning are clouds. The change in the visibility conditions could be explained by larger scattering signals caused by water uptake from present aerosols or arrival of dust-rich air mass from the Sahara. Those arrivals are normally preceded by dust-rich layers placed above the mixing layer, easily identified in the lidar profiles but that has not been observed. Further analysis of the whole set of atmospheric data, supported by backtrajectories, meteorological models (SKIRON) and satellite images (SeaWifs, TOMS) seems necessary. No clouds were detected during the satellite overpasses for days 14th, 15th & 18th, but convective clouds were detected on the 17th morning.

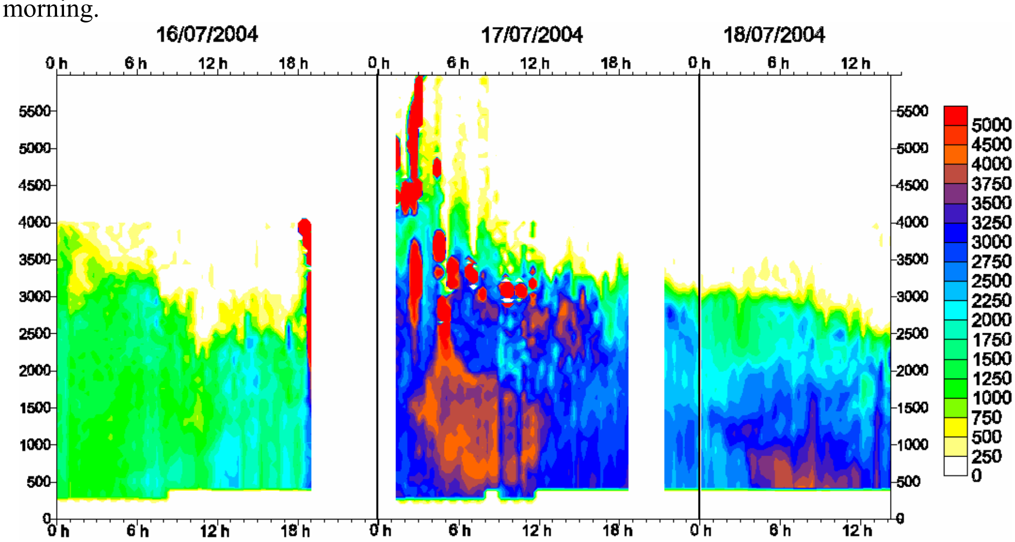

Figure 4.14.Temporal variation of the atmospheric aerosols structure provided by the CIEMAT lidar during the last three days of the SPARC-2004 campaign.

Figure 4.14 shows a comparison of the temperature and aerosol profiles. The virtual potential temperature (θ) was calculated from the dry and wet bulb temperatures at each height in order to identify the mixing layer, where it remains constant. In the Figure, it reaches up to 1300 m, with wind speeds over 5 ms^{-1} and south-east component. Then, θ increase from 304 to 308 ºK, remaining there up to 3000 m, with weaker winds from the west, indicating the residual layer from the previous day. The lidar profile shows the aerosol loading in both layers, with a slight increase in the mixing layer and decrease in the residual layer. This situation occurred the three first days of the campaign, but the last two days, the aerosol load reached up to 4000 m in a fairly constant profile. The aerosol loading of the residual layer must be considered on atmospheric correction algorithm

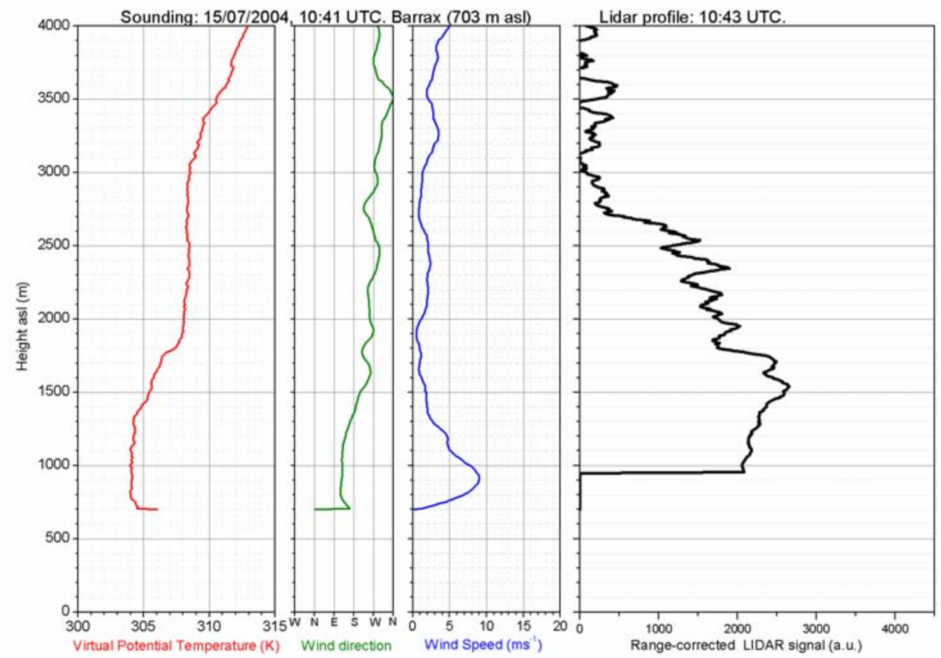

Figure 4.15. Comparison of the radiosounding data (virtual potential temperature (in red) and wind direction (in green) and speed (in blue)) with the aerosol vertical profile (in black) provided by the lidar system

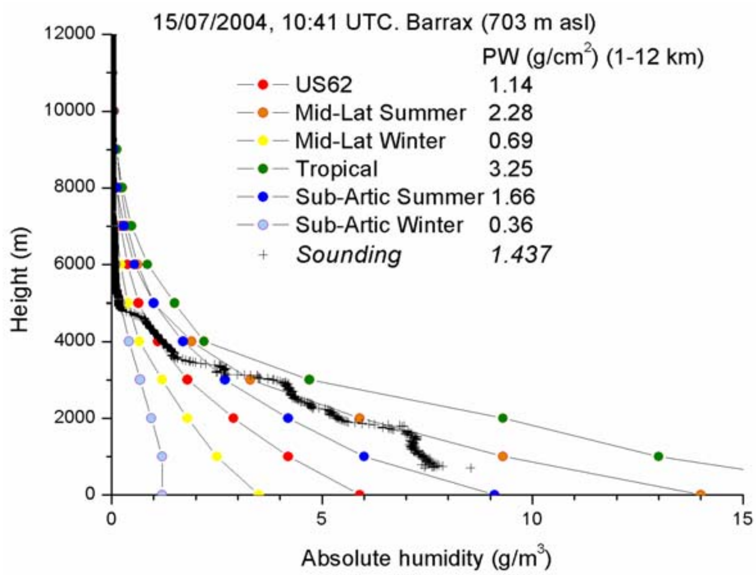

Figure 4.16. Comparison of the measured water content profile with the standard atmospheres. Precipitable water values are integrated between 1 and 12 km.

Figure 4.16 shows the vertical profile of the water content measured on day 15th at the satellite overpass time and the standard atmospheres profiles taken from McClatchey (1982). The measured profile nearly follows the Mid-Latitude Summer atmosphere, as one would expect, up to 4 km, dropping to negligible values from there. Due to this, the integral of this profile produce values comparable to the Sub-Artic Summer atmosphere. Values for other days were tabulated on the last column of table I and may be compared with those of the standard atmosphere indicated in the Figure

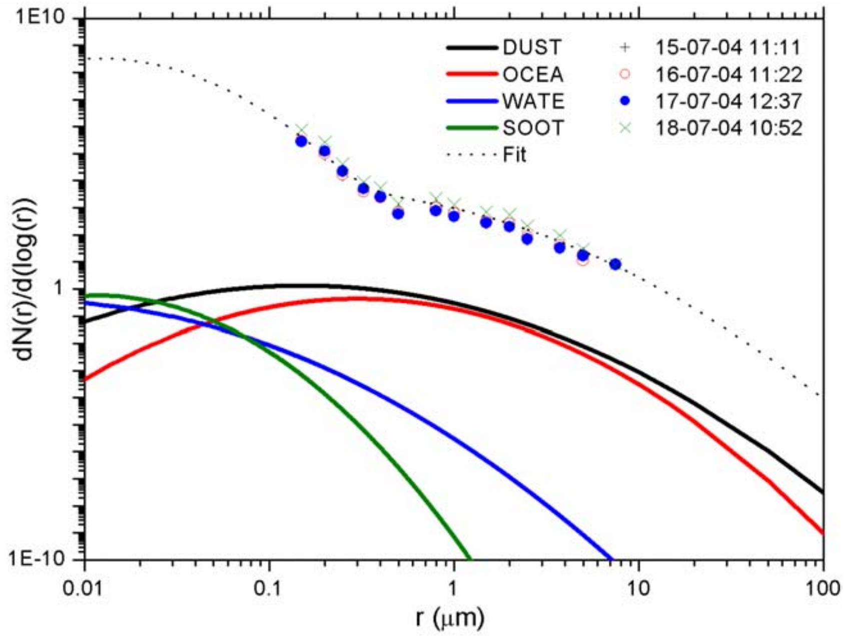

Figure 4.17. Fit of the 6S aerosol components to the experimental size distribution measured at the satellite time overpass for days 15th to 18th of July 2004. Volume percentage for each component are: Dust-like: 90.39%, Water-soluble: 0.38%, Oceanic: 0.06%, Soot: 9.17%

Finally, Figure 4.17 shows aerosol size distributions measured during the campaign at four different times, near the satellite overpass time for the last four days. The aerosol components employed by the 6S algorithm (World Meteorological Organization (CAS)/Radiation Commission of IAMAP, 1983) were fitted to these values. Further effort is required in this attempt, either as a validation of the values provided by the correction algorithm or as a source of initial data for the process.

Conclusions

The meteorological conditions over Barrax during the campaign were dominated by relative low pressures systems, produced by the intense solar heating of the central plateau of the Iberian Peninsula. During day 16th, a change in the synoptic situation occurred, producing rain showers in the evening and different visibility conditions in the following days. This change is not completely understood and further analysis of the whole set of atmospheric data seems necessary. No clouds were detected during the satellite overpasses for days 14th, 15th & 18th, but convective clouds were detected on the 17th morning. Aerosols were systematically found in the residual layer, so this loading must be considered on atmospheric correction algorithm. The precipitable water data show that the Sub-Artic Summer standard atmosphere model was the most convenient to depict the atmospheric conditions over Barrax during the campaign, although during the five days there was a different water profile evolution for each day. Preliminary fit of the 6S aerosol components to experimental ground-level aerosol size distributions between 0.3 and 20 μm opens a new validation approach. No significant changes were observed on the ground-level size distribution during the campaign.

Future work

An analysis of the origin of air masses through a study of backtrajectories, models and satellite images will be accomplished in order to establish the more probable origin of the aerosols detected during the last two days of campaign. A re-processing of the lidar profiles, once the AOD measurement are available, will provide the aerosol extinction coefficient vertical profile a (z) (km-1). This parameter may be integrated in the different layers in order to assess the contribution to the aerosol optical depth of each of the layers. Finally, a comparison of the measured aerosol size distributions with those estimated by the atmospheric correction algorithm seems an interesting study to be carried out.

5 - GROUND RADIOMETRIC MEASUREMENTS

5.1 SURFACE RADIOMETRIC CHARACTERIZATION DURING SPARC

Main tasks

Optical radiometric measurements were performed with three objectives in mind:

- Characterization of different surface types for calibration and validation of Remote Sensing Images.
- Radiometric characterization of main crops in test area.
- Reflectance and Transmittance at leaf level from selected crops.

5.1.1 Surface characterization

The main purpose of these measurements is to obtain sufficient representative spectra from different surface types of the test area. These spectra are to be used for calibration and validation of the atmospheric correction of airborne and spaceborne hyperspectral images.
A sampling strategy had to be designed in order to have a correspondence between the field measurements and the images that allows proper comparison and validation.

There were a number of requirements to be satisfied:

- Field measurements should be simultaneous to image acquisition. Image acquisition takes a very short time to perform: few minutes for spaceborne images, and tens of minutes in the airborne case. Ground measurements cannot be performed in such a short time, least if a large enough number of samples are planned. Therefore a time window of ±1h from flight time was used to perform field radiometric measurements, assuming that illumination and surface conditions remained stable during this period.
- For calibration purposes large homogeneous and stable surfaces are desirable; unfortunately such type of fields is not usually available, and Barrax test site is no exception. In principle bare soils are stable in time and structure, but they present a high variability, therefore it is necessary to take measurements in many points within a single field and record accurate GPS coordinates. Dense vegetation canopies have low angular effects (except at hot spot) but they are not as homogeneous as it is usually thought due to natural variability, also to move in those fields is difficult and slow.
- A large number of fields had to be measured in order to cover the largest portion of the study area.
  - Bare soils: with different brightness, colour and textures.
  - Vegetation: homogeneus (alfalfa), tall (corn, vineyard), short (sunflower, grass), sparse (garlic).
  - Stubble

  The complete list of surfaces is collected and located in the map below.

  It is interesting to note that it was very helpful for the selection of the fields and measurement planning, the readily availability of the CHRIS/PROBA quicklooks the very morning after the first acquisition, providing the teams with the "real time" situation of the fields, to complement the land-use maps prepared before the campaign.

To satisfy these requirements we counted with three spectrorradiometers with full range capability 350-2500nm: two ASD FieldSpec (one belongs to Centro de Estudios y Experimentacion de Obras Publicas CEDEX and the other to LEO/GPDS groups of University of Valencia), and one GER3700 from IDR of University of Castilla-La Mancha in Albacete(Figures 5.1 and 5.2).
The GER3700 was mounted on a crane in order to take measurements over a vineyard field where Energy Balance measurements were taking place. This crop has a strong vertical structure with large gaps between rows.
The other two radiometers were dedicated to sample the rest of surfaces.

Figure 5.1. ASD FieldSpect Pro-FR Spectroradiometer

Figure 5.2 GER 3700 Spectroradiometer

Samplig strategy

The sampling strategy was to cover the fields in transects with continuous measurements (Figure 5.3), making several stops at random to take white reference radiance and a larger number of samples of the same spot for greater accuracy.
The continuous measurements taken between spots, making use of user defined integration time, allows to obtain spectra corresponding to an area of several meters of length, which can be better compared to that of remote sensors.

- Spot measurements
  - 3 still measurements of the same sample, reducing error bars
  - White reference at start and end to estimate illumination stability
  - Samples located by GPS to allow match with images.

- Continuous measurements
  - Taken while walking between spots
  - Integration time allows to cover several meters
  - Distance between spots is large, allowing to catch field variability
  - No white reference could be taken while walking, what introduced the need of interpolation with a reduced accuracy in these reflectances.

In this campaign more than 2000 radiance spectra were collected. They were processed by the GPDS team to check for bad data, calculate reflectances from the radiometric measurements, and calculate error bars for each one (Figure 5.4).

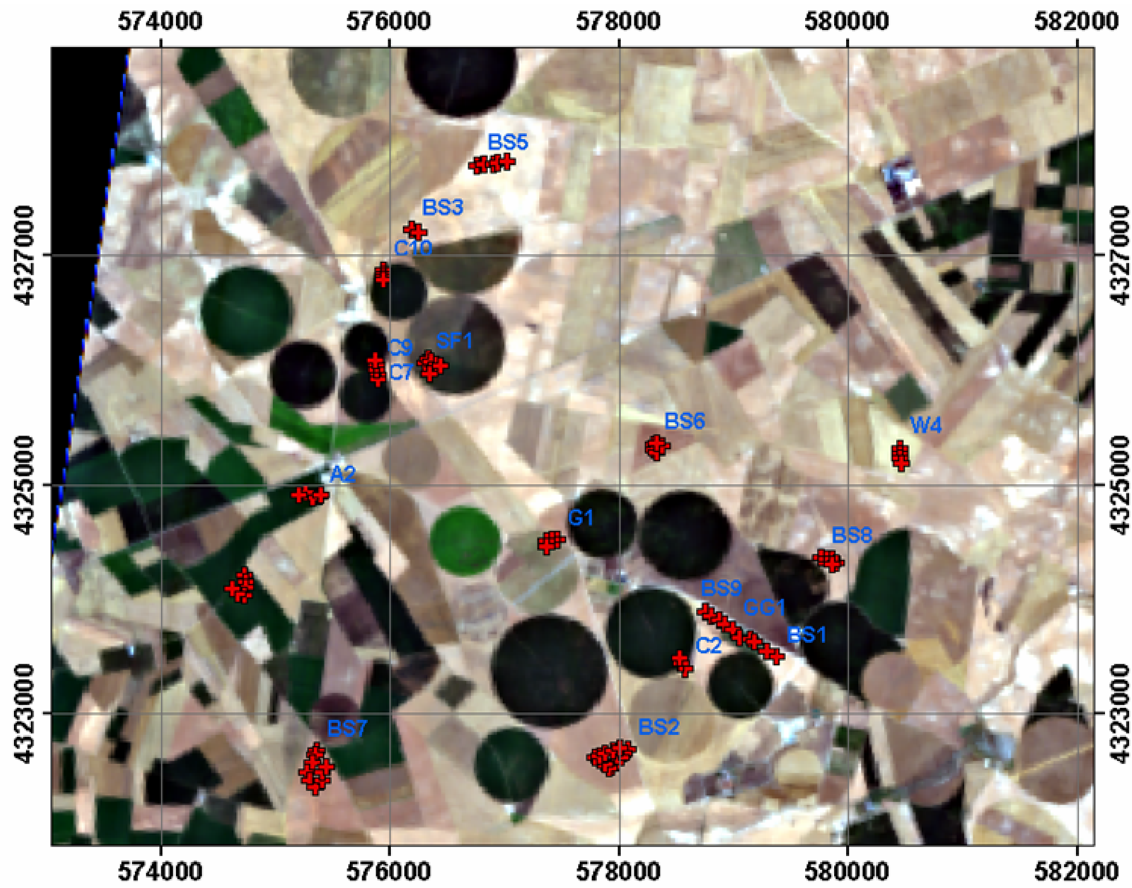

Figure 5.3. Sampling strategy was to cover the fields in transects with continuous measurements

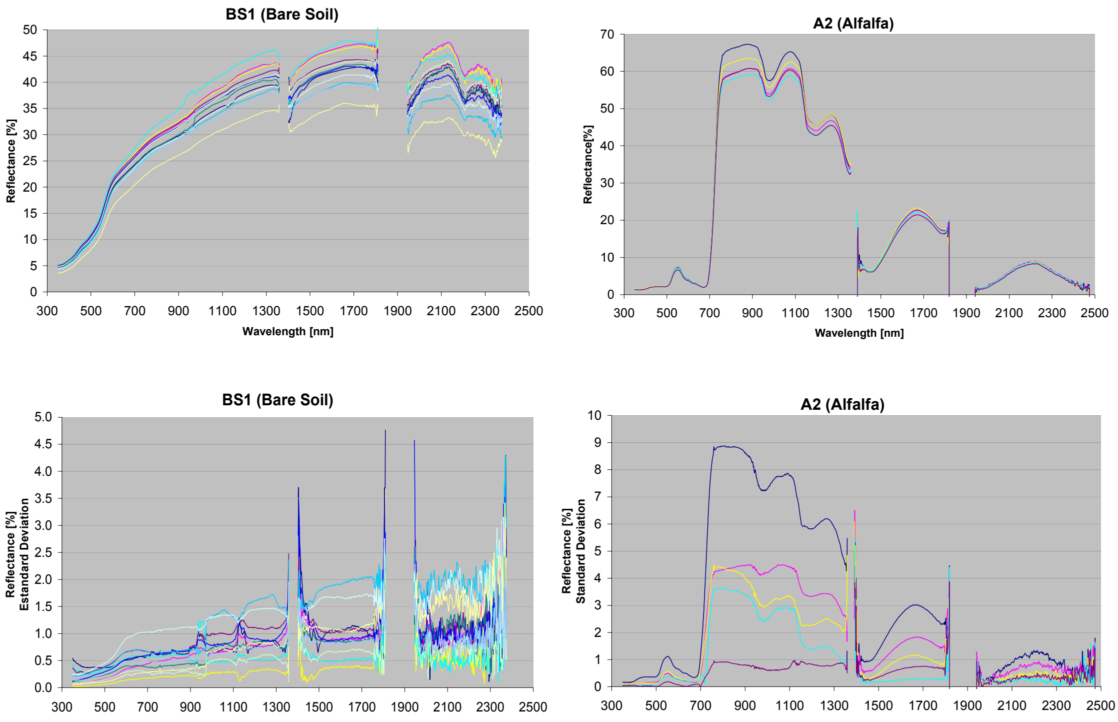

Figure 5.4.Soil and vegetation reflectances taken at several spots within a field. Below the corresponding standard deviations.

5.1.2. Leaf Reflectance and transmittance

Several leaf samples were collected and preserved for transmittance and reflectance measurements in the laboratory, from those crop fields where biophysical measurements were taking place.
These measurements took place in a dark room specially set for the purpose in a building of the ITAP at the test area. An ASD-FSFR was used for this purpose together with two experimental imaging radiometer systems based on optical tuneable filters (AOTF). Unfortunately the setup based on AOTF imaging spectrometer did not work due to technical problems.

Figure 5.5. Brimrose AOTF Video adapter with a B/W Firewire camera.

Figure 5.6.Monochrome video camera.

The setup for these measurements consisted in:

- Diffuse light source
- White reference (Spectralon)
- Black cavity; used as background in reflectance measurements to avoid light coming from behind the leaf mixing with the reflected light.
- Black shade; to block light from outside the leaf in transmittance measurements.

Special care was taken to assure that all the black elements in the setup were actually black at all wavelengths, and not just in the visible (unfortunately it is a common assumption to think that black objects to the eye are also black in the IR regions which are invisible). We used "jet black" spray paint for cars which has a around 1% reflectance in all wavelengths, and from most view angles (except in the especular case that was avoided).

The samples measured were:

Corn from field C10: middle and upper part of the same leaf.
Vineyard from field V: large and small leaves from vase cultivated plants.
Sugarbeet from field SB1: Tip and side from a large leaf.
Potato from field P2: Two large leaves.

5.1.2.1 Leaf Reflectance

To measure leaf reflectance the setup was designed to place the elements (light source, sensor, sample, white reference, and black background) in such a way that the illumination would be as close to perpendicular to the sample as possible, without casting shadows from the sensor. The tip of the fibre optics was placed at a distance from the sample that would cover a large area of the leaf without interfering with the illumination; this distance will be maintained in the transmission measurements to be consistent. As a black background a cavity painted black was used, the radiance coming from this cavity with the illumination turned on was as low as the instrument's noise level, what assures that the signal measured from the leaf had no contribution from the background.

Absolute black background equivalent to intrument noise levels

Closest to perpendicular illumination without interference of elements

Avoid wrinkles and shadows

5.1.2.2 Leaf Transmittance

To measure leaf transmittance a black shade was place in front of the light source reducing the lighted area to a size smaller than the leaf, avoiding light going directly to the sensor.
The distance from the tip of the fibre optics to the sample was the same that in the reflectance measurements, and the sampling spot was approximately the same.

Dificulties Encountered

The diffuse light source was directly connected to the power line, without the use of a power stabilizer. This introduced low frequency variations in light intensity that affected the measurements. The spectrorradiometer's integration time was increased in order to reduce this effect by averaging the variations; but at the same time we had a time constrain during transmittance measurements, as the heat degraded the leaf tissues for long exposure times. A compromise had to be found to cope with both effects.

We faced another problem with non-flat leaf samples. We did not have a proper holder that would maintain the samples still and without wrinkles. This could introduce shadow effects, especially in reflectance measurements.

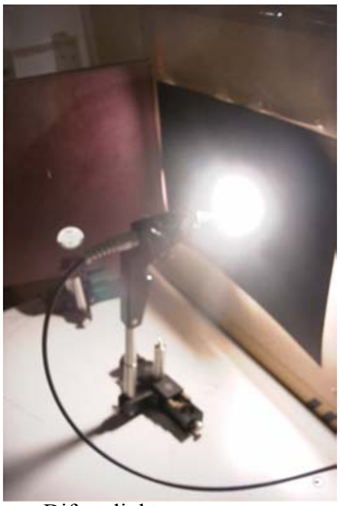

Difuse light source
Reduced aperture

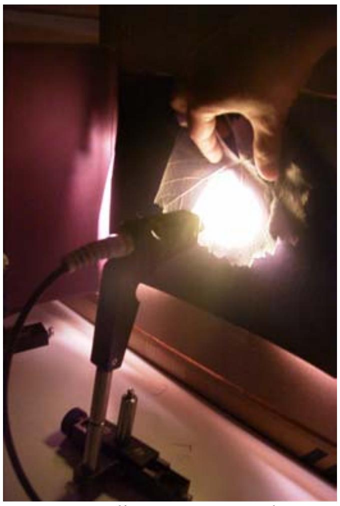

Same distance to sample
than for reflectance

The order for these measurements consisted in first measuring reflectance of both sides of the leaf, and then transmittance, also from both sides. This order was chosen to avoid the impact of tissue degradation (due to high temperature during transmittance measurements) in reflectance measurements. In order to be able to estimate a confidence value of the resulting spectra, each measurement was repeated three times, and the white reference was taken before and after sample measurements (also three times). In this way we could assess the stability of the illumination during the process, and obtain the standard deviation of the measurements, which in this case gives an estimate of the errors committed. It is interesting to note that the shorter and larger wavelengths suffer a higher dispersion in the measurements due to the low levels of radiance from the halogen light source in these regions. In some small leaves the central nerve was within the sampling area, which has different optical properties than the green part of the leaf. In these measurements it is impossible to determine its contribution to the reflectance; that is why it is very interesting to use an imaging spectrometer for leaf reflectance/transmittance measurements.

Corn C10 - Sample 1: Middle part of the leaf

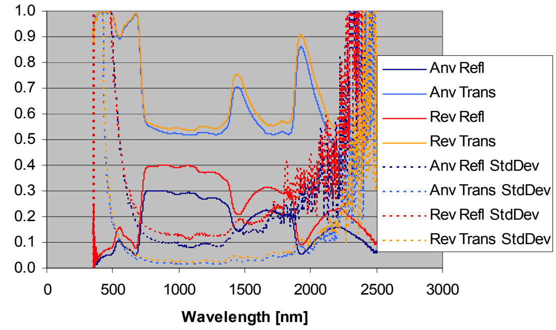

Corn C10 - Sample 2: Upper part of the leaf

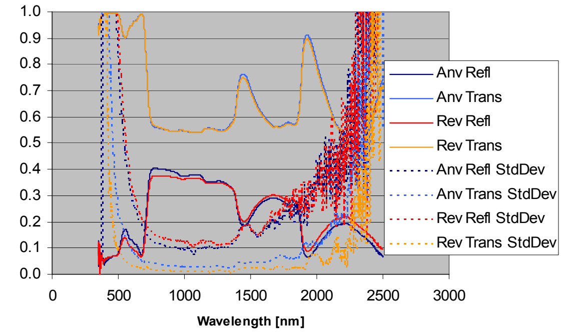

Vineyard VV - Sample 1: Small leaf

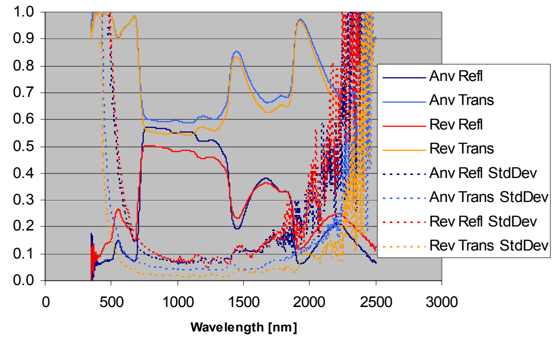

Vineyard VE - Sample 1: Medium leaf

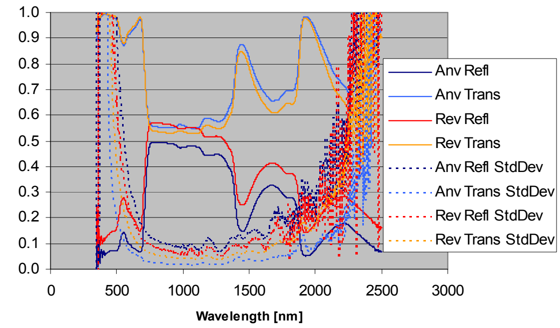

5.2 THERMAL INFRARED GROUND RADIOMETRIC MEASUREMENTS

5.2.1 Instrumentation

Radiometric measurements were carried out in the thermal infrared region with various instruments that include fixed FOV and single band or multi bands radiometers. In addiction, a thermal camera, termocouples and a black body (calibration source) for calibration purposes were used.

· CIMEL 312-1 radiometer

The CIMEL CE-312-1 is a radiance-based thermal-infrared radiometer composed of two major components: an optical head containing the detector and optics, and the electronic unit which performs the data storage. The detector includes one broad-band filter, 8-13 µm, and three narrower filters, 8.2 – 9.2 µm, 10.5 – 11.5 µm and 11.5 – 12.5 µm (Table 1). An external temperature probe can be added by the user into the control unit. It allows collecting the temperature of an external blackbody especially for the estimation of absolute emissivity. A set of different scenarios is available to collect data depending on the user desires.

· CIMEL 312-2 ASTER radiometer

The CIMEL CE-312-2 ASTER is a radiance-based thermal-infrared radiometer composed of two major components: an optical head containing the detector and optics, and the electronic unit which performs the data storage. The detector includes 6 bands, a wide one, 8-13 µm, and five narrower filters, 8.1 – 8.5 µm, 8.5 – 8.9 µm, 8.9 – 9.3 µm, 10.3 – 11 µm and 11 – 11.7 µm (Table 2). An external temperature probe can be added by the user into the control unit. It allows collecting the temperature of an external blackbody especially for the estimation of absolute emissivity. A set of different scenarios is available to collect data depending on the user desires.

· EVEREST 3000.4ZLC Infrared temperature transducer

The Everest thermometer, model 3000.4ZLC single band 8 – 14 µm collects the infrared radiation from the sample converting it into electrical signal. With the suitable calibration process, the electrical signal is converted to a signal in terms of temperature. It is scaled from – 40ºC to 100ºC with a resolution of 0.1 K, an accuracy of ±0.5 K and a repeatibility of ±0.1K. The Field of View -FOV- is 4º. It has an adjustable emissivity equal to unity. The output signal is in mV (10 mV/º), and the power requirements is 5V to 26V DC. Power supply was provided by an auxiliary Einhell power station

· RAYTEK ST6 Infrared radiometer

A portable RAYTEK, model ST6 single band 8–14 µm, with a FOV of 8 degrees, and with adjustable emissivity operation mode was used. It ranges up to 100ºC with a sensitivity of 0.1 K and an accuracy of 0.5K. It has a laser beam that helps to locate the target for the measurement.

· RAYTEK Thermalert MID radiometers

The Raytek Thermalert MID radiometer is an infrared sensor with a single band 8–14 µm, with a FOV of 20 degrees, and with adjustable emissivity operation mode. It ranges up to 600ºC with a sensitivity of 0.1 K and an accuracy of 0.5K.
Two instruments, Raytek MID-1 and Raytek MID-2, were used during the field campaign with the same characteristics

Thermocouple Type K.

The water and surface temperature was measured with different thermocouples with error lower than 0.1 ºC.

Thermal camera Irisys-Iri1001

The thermal camera was used in the angular measurements jointly the CIMEL instruments

· EVEREST 1000 calibration source

A calibration source EVEREST model 1000 was used to calibrate the radiometers. Its operating range is from 0ºC to 60ºC, with a resolution of 0.1K, with an absolute accuracy of 0.3 K over entire range.

GALAI 204-P calibration source (from the ULP)

A calibration source GALAI model 204-P was used to calibrate the radiometers

LICOR LI-1000 Dataloggers

Four different Licor LI-1000 dataloggerss were used to storage data from both radiometers and thermocouples

CAMPBELL CR21 Micrologger (from the ULP)

The Campbell micrologger is a compact, self-contained datalogger with Programming capabilities dependent on internal software PROM. It was used to storage the radiometers data.

Goniometer motorized system

A Goniometer with a rotating arm installed to change the observation angle in the zenith direction, a 1m high elevator to adjust the measuring level and a half circle roadway to change the observation angle in the azimuth direction will be used to measure directional brightness temperature**.**

Details of the instruments are given in Table 5.2.

Table 5.2. Thermal Infrared instrument settings.

MODEL	SPECTRAL BANDS	RANGE OF TEMPERATURE	ACCURACY	FOV
Cimel CE 312-1	8 – 13 µm 8.2 – 9.2 µm 10.3 – 11.3 µm 11.5 – 12.5 µm	– 80 to 60º C	0.1º C	10º
Cimel CE 312-2 ASTER	8 – 13 µm 11 – 11.7 µm 10.3 – 11 µm 8.9 – 9.3 µm 8.5 – 8.9 µm 8.1 – 8.5 µm	– 80 to 60º C	0.1º C	10º
Everest 3000.4ZLC	8 – 14 µm	– 40 to 100º C	0.5º C	4º
Raytek ST8	8 – 14 µm	– 30 to 100º C	0.5º C	8º
RAYTEK THERMALERT MID	8 – 14 µm	– 40 to 600º C	0.5º C	20º

EVEREST 3000.4ZLC
Infrared temperature transducer

Goniometer motorized system

CIMEL 312-1 radiometer

RAYTEK ST6 Infrared radiometer

EVEREST 1000 calibration source

RAYTEK Thermalert MID radiometers

Thermal camera Irisys-Iri1001

Thermocouple Type K

GALAI 204-P calibration source (from the ULP)

5.2.2 Aqcquired data

A set of thermal radiometric measurements was carried out in the framework of the SPARC-2004 experimental field campaign. The retrieval of bio-geophysical parameters such as land surface emissivity and temperature was the main aim of these measurements. To this end, radiometric measurements were carried out in the thermal infrared region with various instruments that included fixed FOV and single band or multi bands radiometers. In addition, a thermocouple for thermometric temperatures measurements and black bodies (calibration sources) for calibration purposes were used.

Table 5.3. Work Plan carried out by GCU in the framework of SPARC '04

DATE	CIMEL CE 312-1	CIMEL CE 312-2 ASTER	THERMAL CAMERA	RAYTEK MID-1	RAYTEK MID-2	EVEREST	RAYTEK ST-6	OMEGA	THERMISTORS	OVERPASS			
										Plane	AATSR	ASTER	CHRIS/PROBA
15-July	Fixed in a mast on GG1	Fixed in a mast on BS1		Fixed in a mast on GG1	Fixed in a mast on BS1 Fixed in a mast on V	Fixed in a mast on WB Fixed in a mast on V	Transect on GG1 and BS1		Thermal Variation on WB	10:43			11:11
16-July	Direccional emissivity measurements on baresoil in V				Fixed in a mast on BS1 Fixed in a mast on V	Fixed in a mast on WB Fixed in a mast on V							11:22
17-July	Transect on A4	Transect on W1		Fixed in a mast on BS1	Fixed in a mast on GG1	Fixed in a mast on BS1					10:37		
18-July	Transect on A3	Transect on BS2. TES method measurements on BS2 and C2		Fixed in a mast on BS1	Fixed in a mast on GG1	Fixed in a mast on BS1	Transect on CW1	Fixed on C1 and C2	Thermal Variation on WB	10:30		11:00	
19-July	Night directional emissivity measurements on GG2, V and baresoil in V.			Fixed in a mast on BS1	Fixed in a mast on GG1	Fixed in a mast on BS1							
20-July				Fixed in a mast on BS1.	Fixed in a mast on GG1						10:11		
21-July	Directional emissivity measurements on GG2 and baresoil in V. TES method measurements on WB, GG1, BS1, CW2, G1, P1 and A4.		Directional emissivity measurements on GG2 and baresoil in V.								10:42		

Therefore, the experimental work of the Global Change Unit of the University of Valencia were the measurement of thermal radiometric temperatures, emissivities, atmospheric radiances, air temperature, temperature transects and angular measurements within the BARRAX area (see Table 5.5). Transects were performed concurrently to the flight/satellite overpasses (HyMap, Rosis, Chris/Proba, AATSR, Landsat, Aster, MSG (daily). Transects were carried out taking temperature measurements with different field radiometers (CIMEL, RAYTEK and EVEREST), at regular steps (3 meters) or fixed in characteristic areas

A) TRANSECTS

Transects were taken over several samples surfaces. The transects were performed concurrently to the satellites flights over the studied samples. They were carried out taking temperature measurements with field radiometers, at regular steps (3 meters) along a walk performed within a well defined area.

The transects were made half an hour before the scheduled plane/satellite overpass and ended half an hour later, and we made sure that the sky was clear during taking measurements.

B) MASTS

Thermal measurements were continuously recorded with radiometers located on fixed masts over determined areas and periods of time, in coincidence with the plane/satellite overpasses. As an example, we show an overview of the data in two cases: bare soil and green grass.

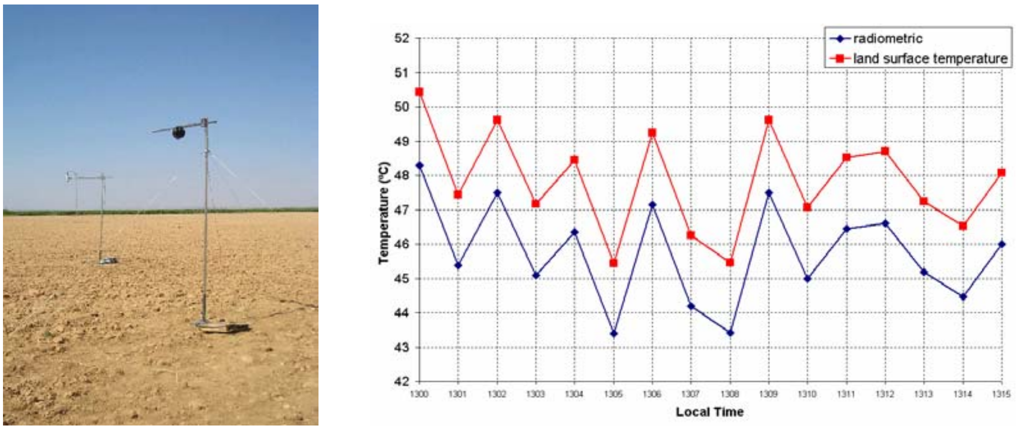

Figure 5.7. Radiometric and land surface temperature values measured with the RAYTEK MID (8-14 um) over bare soil.

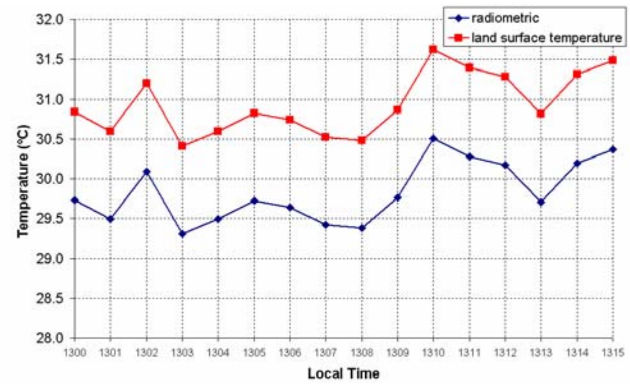

Figure 5.8. Radiometric and land surface temperature values measured with the RAYTEK MID (8-14 um) over green grass.

3) ANGULAR EMISSIVITY MEASUREMENTS

An experimental investigation of the angular variation of the infrared emissivity of some representative samples at angles of 0º-60º (at 10º increments) to the surface normal was ccarried out. We took several series of measurements for each sample, so that we could obtain the mean values shown by the graphics. Before and after each series, we measured the sky temperature pointing to the zenith. The two CIMEL radiometers were mounted together and were used simultaneously with the thermal camera to measure radiometric temperature.

The main difficulties for this kind of measurement were:

1) Necessity of clear sky (clouds modify hemispherical downwelling radiance).

2) Problem to determinate surface temperature in a “big” ground area (mixture of soil, leafs, sun and shadows).

As a result, (1) We have measured only in absence of clouds, (2) doesn’t allow to study absolute angular emissivity variation in heterogeneous samples.

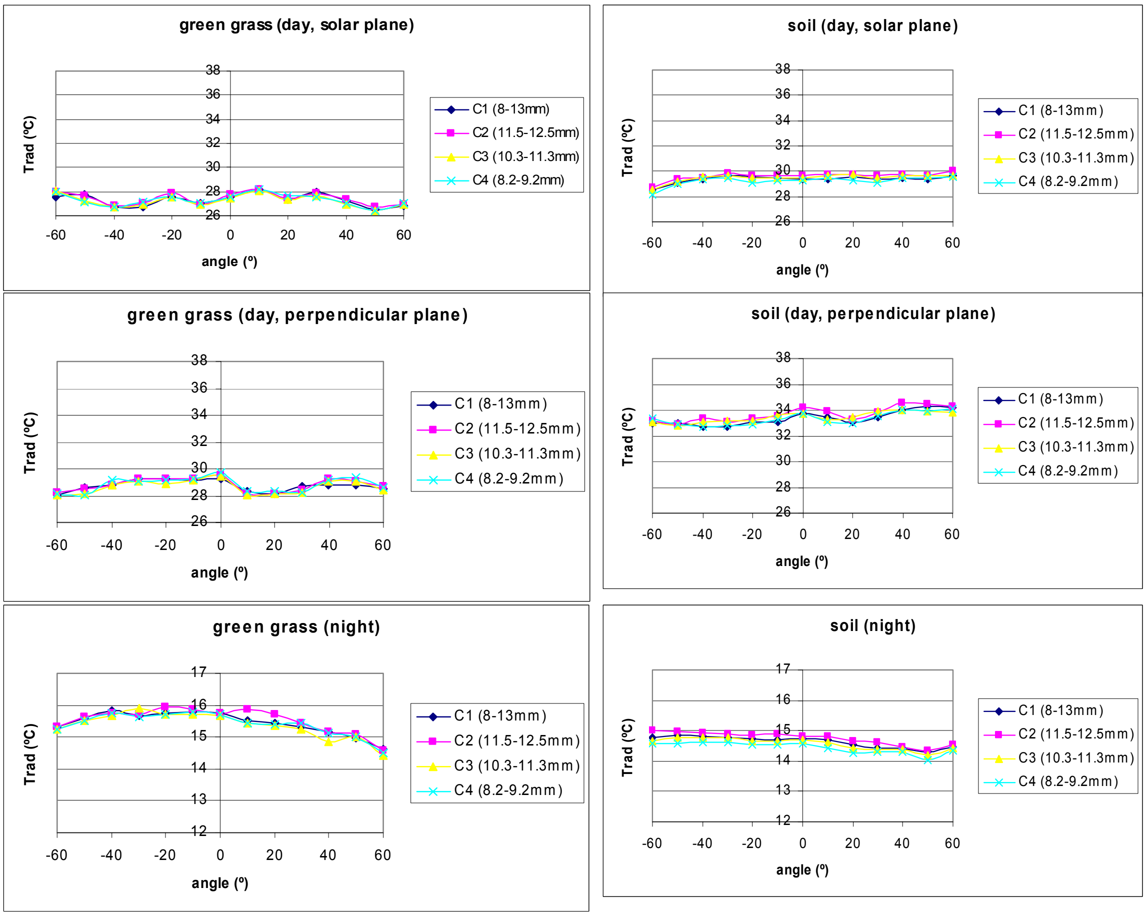

Figure 5.9. Angular measurements of radiometric temperature using the goniometric device.

6 - VEGETATION MEASUREMENTS

6.1. Vegetation properties and sampling strategy scheme

A large amount of ground measurements were collected in the Barrax study area during the SPARC campaign, covering LAI, fCover, Leaf Chlorophyll a+b, Leaf water content and leaf biomass, together with other complementary data. All the available ground measurements were cross-checked with GPS measurements.

The sampling strategy to be followed in choosing measurement points was designed according to statistical criteria. Nevertheless, most times experimental constraints become critical, and finding a balance between what is mathematically optimal and what is experimentally possible requires some compromise.

According to statistical requirements, till 4 to 15 areas have been sampled to fully characterize a crop (its size and heterogeneity). These areas were chosen randomly, but it was not operationally very often (high plant densities, very wet soils or tall plants may cause moving across the cross be very hard). So, the aim was to perform random sampling in crops where it was possible, but restrict sampling to crop geometrical constraints when it was not. For example, taking samples in 1.80 meters high corn crops following the circular track made by irrigation pivot wheel could be a good idea.

Once sampling areas were chosen, a strategy to take samples inside each area was again needed. The above considerations on the choice of areas were again useful in point sampling within the sampling area: random criterion was mathematically supported, so it was the one to be followed when field crop configuration allowed it; however, it was sometimes difficult to move around one measurement point to take samples randomly, so mobility requirements might be taken into account in such cases, and a sampling strategy that made sampling easier might be followed.

Table 6.1 shows the number of fields measured for each crop during SPARC-2004 campaigns compared to SPARC-2003 number of samplig areas.

Table 6.1. SPARC-2004 vs. SPARC-2003 sampled areas

CROP	SPARC 2003 Number of sampled areas	SPARC 2004 Number of sampled areas
GARLIC	1	2
ALFALFA	5	6
ONION	2	3
SUNFLOWER	none	3
CORN	6	6
POTATO	1	3
SUGAR BEET	3	2
VINEYARD	none	2
WHEAT	1	none
PAPAVER	1	none

Biophysical parameters used in the characterization of the different crops:

a. Dry Matter content (DM)
b. Water Content (WC)
c. Leaf Area Index (LAI) from LAI-Licor
d. Fractional Vegetation Cover (FVC) from hemispherical photographs
e. Chlorophyll Content (CC)

The number of Elementary Sampling Units (ESUs) measured during SPARC-2004 for the biophysical parameters characterization of the different crops is showed at table 6.2. Number of measurements per ESU was different depending on the biophysical parameter measured and the strategy scheme designed for each case. Each strategy will be described with detail at the same time that parameter acquistion data.

Table 6.2. Number of ESUs .SPARC-2004

CROP	NUMBER OF ESU'S			
	LAI		Chlorophyll	Biomass
	LAI-LICOR (5x8 per ESU)	HP (12/ESU)	CCM-200 (50 per ESU)	3 per ESU
Alfalfa	22	2	2	3
Corn	19	5	3	3
Garlic	17	4	4	1
Onion	12	3	1	3
Potato	16	4	2	2
Sugarbeet	20	2	1	2
Sunflower	27	4	4	3
Vineyard	4	1	1	2
TOTAL	140	26	18	19

6.2. Data acquisition and measurement protocols

6.2.1. Wet and dry biomass

This is the mass of plant material within a defined area divided by the area size ($kg \cdot m^{-2}$). For taking the dry and fresh matter content measurements, cut a number of leaves (3 per ESU) from a pre-defined samplig area (normaly the field area) and place into separate containers (plastic, bags, etc.). Weigh each component within a few hours (preliminary test can be used to determine permissible elapsed time) simultaneously to digital photograps acquisition of the leaves over squared paper for posterior determination of the area (fig. 6.1). Dry the plants at 70ºC until constant weight is reached and weigh again. From the two masses and the known sampled area, wet and dry biomass can be calculated. Water content is calculated as the percentage of wet (or dry) mass, or per unit area (volume) when biomass (biomass and height) are known. This parameter is the mass of water in a plant sample divided by the mass of the entire plant sample before drying (i.e. on a wet biomass basis). Units are percent or dimensionless, although when plant height and/or biomass are known, water content can also be expressed in kg/m^3 or kg/m^2, respectively). It is given from the biomass evaluation procedure directly, for each one of plant components.
Eight different crops were characterised till 16th untill 18th of July and the number of measured fields was a maximun of three. This number was limited and determined by the land use at Barrax test site during SPARC-2004 campaign.

Table 6.3. Sampling strategy per crops .SPARC-2004

CROP	16/07/2004	17/07/2004	18/07/2004
GARLIC	G-1	-	-
ALFALFA	A-2	A-3	A-1
ONION	ON-1	ON-2	ON-3
SUNFLOWER	SF-1	SF-2	SF-3
CORN	C-2	C-10	C-6
POTATO	P-1	P-2	-
SUGAR BEET	SB-2	SB-1	-
VINEYARD		VV, VE	

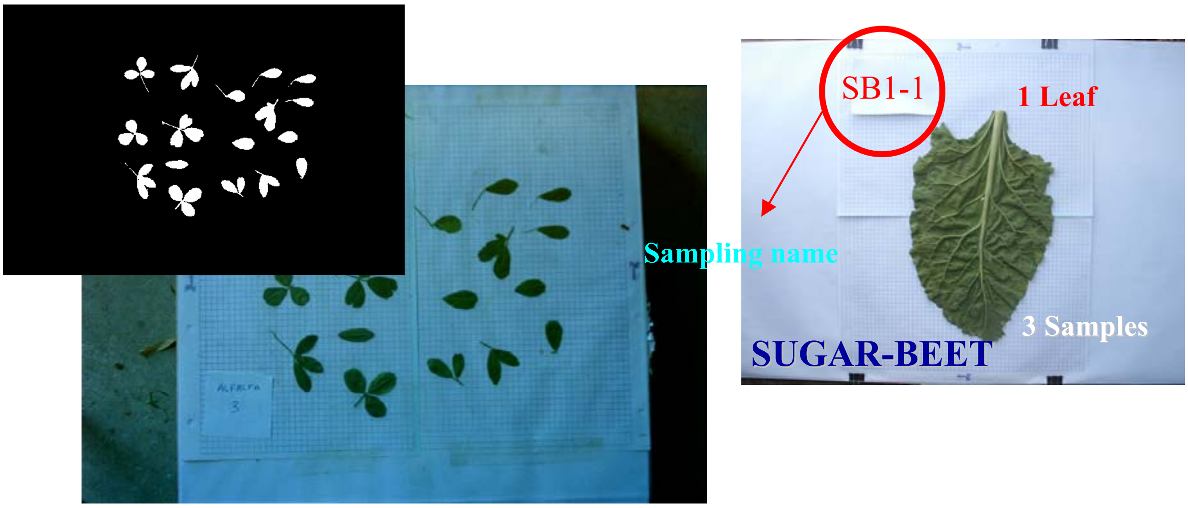

Figure 6.1. Area estimation by means of digital photos and squared mm paper.

Once the dry matter and water content were determined from each sample, results were checked per ESUs, as a first step, and per crops as a second step, and compared to SPARC-2003 data for their posterior statistical and spatial variability analysis that will be described at PART-II of this report.
This methology was applied to each biophysical parameter under study and results obtained for dry matter and water content are showed at tables 6.4 and 6.5 and Figures 6.2, 6.3.

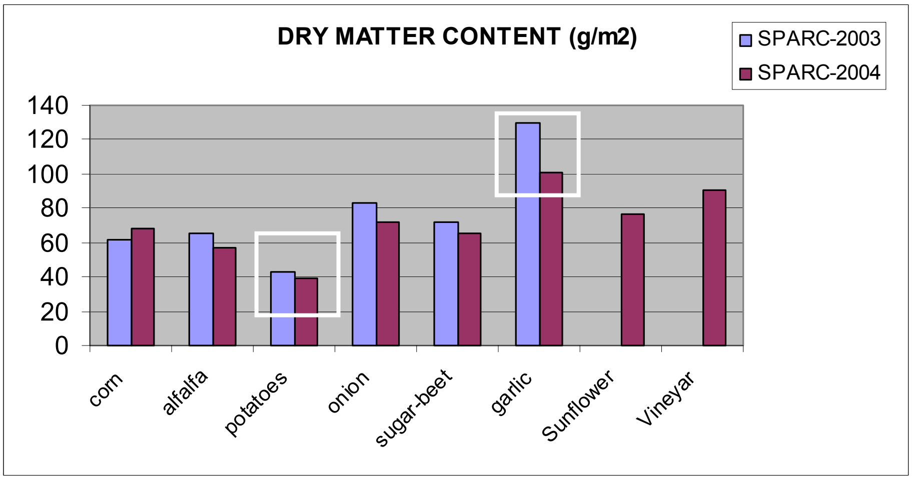

Figure 6.2. Dry matter content mean values per crops. SPARC-2004 data in red compared to SPARC -2003 data in blue. Lowest values were got from potato fields measurements and highest results from garlic.

Comparisson between SPARC-2003 and SPARC-2004 dry matter content mean values obtained per crops gave us a similar behaviour when we characterised the vegetation under study (Figure 6.2). Lowest values were got from potato fields' meassuerments and highest results corresponded to garlic crops. When water content values were checked we found the low range of values for alfalfa crop (Figure 6.3) and the 2003 highest values differed to 2004 results (respectively got maximum values for onion and garlic).The different phenologycal state of those crops during the two SPARC campaigns determined differences found for water content values because we were measuring a parameter which characterice dinamic properties of the plant.

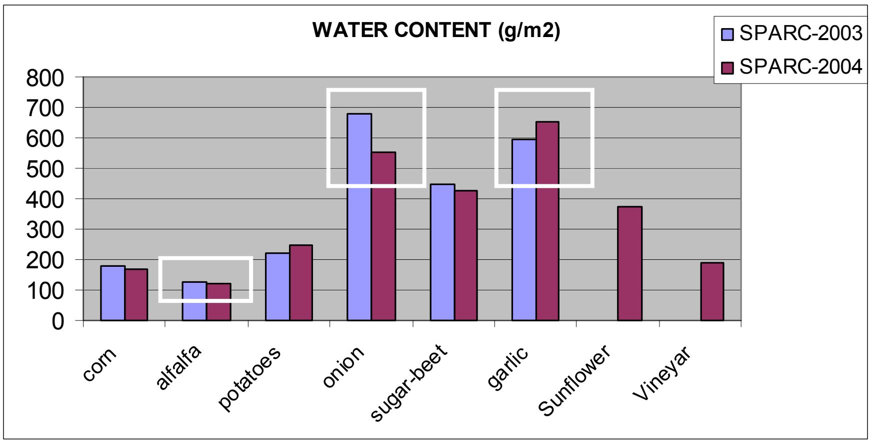

Figure 6.3. Water content mean values per crops. SPARC-2004 data in red compared to SPARC-2003 data in blue. Lowest values were got from alfalfa fields measurements and highest results from garlic and onion respectivly for 2004 and 2003 campaigns.

Tables 6.4 and 6.5 shows dry matter and water content ranges of values messured during SPARC 2003 and SPARC-2004 campaigns for the different crops and their mean and standard error associated values.

Table 6.4.SPARC-2004 DMC and WC range of values

Crop	DM Range of values	DM $\mu \pm \sigma$	WC Range of values	WC $\mu \pm \sigma$
Corn C1	53.9 – 69.9	61 ± 6	165.9– 189.5	180 ± 8
Alfalfa A1	55.4 –106.1	90 ± 20	110.9 –160.3	140 ± 30
Alfalfa A9	47.1 – 90.4	65 ± 19	105.9 – 142.8	126 ± 16
Potato P1	39.7– 46.1	43 ± 3	213.8 – 240.4	223 ± 15
Onion On1	71.4 – 81.4	83 ± 7	602.9 – 810.1	680 ± 70
Sugarbeet B1	50.5 – 81.8	72 ± 11	315.1 – 635.6	400 ± 100
Garlic G1	99.8 – 189.5	130 ± 30	482.1 – 712.1	600 ± 90

Standard error associated to 2004 measurements was, in general, lower than to 2003 data and results got for those ESUs meassured at different fields for the same crop are very similar. This fact gave us confidence in the SPARC-2004 results and their robustness.

Table 6.5.SPARC-2003 DMC and WC range of values

Crop	DM Range of values	DM µ±σ	WC Range of values	WC µ±σ
Corn C2	62 – 67	65 ± 3	176– 185	181 ± 7
Corn C10	74 – 78	76 ± 3	144 – 153	148 ± 6
Corn C6	61 – 64	63 ± 2	156 – 179	168 ± 15
Alfalfa A2	37 – 49	42 ± 6	118– 120	119 ± 1
Alfalfa A3	67 – 82	76 ± 8	121 – 132	126 ± 6
Alfalfa A1	50 – 56	53 ± 4	115 – 135	125 ± 14
Onion On1	50 – 59	55 ± 4	508 – 589	550 ± 39
Onion On2	85 – 93	90 ± 3	532 – 683	607 ± 76
Onion On3	69 – 74	274 ± 14	453 – 524	499 ± 40
Garlic G1	90 – 106	100 ± 9	621 – 701	655 ± 41
Potato P1	37 – 39	38 ± 0.5	218 – 232	226 ± 7
Potato P2	39 – 43	41 ± 2	264 – 277	271 ± 6
Sugarbeet B2	58 – 71	66 ± 7	360– 479	425 ± 60
Sugarbeet B1	62 – 72	64 ± 7	357– 463	424 ± 59
Sunflower SF-1	84 – 92	87 ± 4	341– 399	369 ± 29
Sunflower SF-2	69 – 78	73 ± 5	305– 387	345 ± 41
Sunflower SF-3	67 – 72	70 ± 2	361– 586	460 ± 115
Vine VE	87 – 96	91 ± 5	197– 211	202 ± 8
Vine VV	81 – 101	90 ± 9	166– 189	176 ± 11

6.2.2 Leaf Area Index

Leaf Area Index (LAI) and leaf mean tilt angle (MTA) were made with a LI-COR LAI 2000 instrument, which works by comparing the intensity of (diffuse) incident illumination measured at the bottom of the canopy with that arriving at the top (LI-COR technical report; Welles and Norman, 1990). The LAI 2000 is a portable instrument that does not require additional data acquisition and processing. Incident light is recorded over five concentric angular rings, each of approximately 15° in width (giving a nearly hemispherical field of view) (7°, 23°, 38°, 53° and 67°). LAI is estimated by calculating the probability of a photon penetrating to a depth z in the canopy (under various assumptions regarding the arrangement and radiometric properties of scattering elements in the canopy), and comparing this with the measured radiance at the bottom of the canopy. The angular integral of this property (over all zenith angles) is approximated as a weighted summation over the five concentric angular rings of the instrument.

Figure 6.4 LAI2000 Plant Canopy Analyser

The manufacturer's recommendations were followed in deciding a measurement plan. For reducing the effect of multiple scattering on LAI-2000 measurements, the instrument was only operated near dusk and dawn (6:30-9:30am; 6:30-8:30pm) under diffuse radiation condition using one sensor for both above and below stand measurements. In order to prevent interference caused by the operator's presence and the illumination condition, the sensor field of view was limited with a 180° view-cap. Both measurements were azimuthally oriented opposite to the sun azimuth angle.

LAI measurements were taken with the instrument held a few centimeters above the soil in eight different crops (Alfalfa, Corn, Garlic, Onion, Sugarbeet, Sunflower, Potato and Vigna) within 3 days of image data acquisition.
One measurement of ambient light was made with the sensor extended upward and over the top of the canopy at arm's length. Eight below-canopy readings were then made as show in Figure. This pattern was repeated three times per spot, and the resulting twenty-four samples comprise one full set of measurements. Finally, each centre of the LAI-2000 transects were geolocated by using GPS measurements. This protocol yield a low Standard Error of measurement to assure 90% to 95% confidence interval.

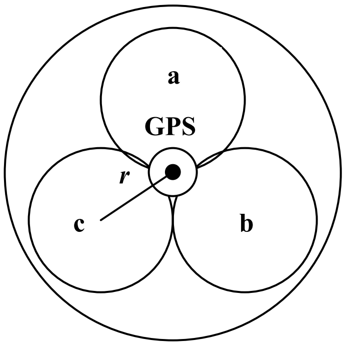

1 LAI DATA for each ESU (Elementary Sampling Unit) is given by: 3 repetitions of 8 measurements
Semi-radius r ≅ 10 m.

For each repetition, 1 above canopy measurement in the center of sector is taken.

Duration of each measure approximately 10-15'.

Figure 6.5 LAI2000 Plant Canopy Analyser

The data for both sensors was recorded with a time stamp on attached data loggers and then dumped to a computer through an integral RS-232 port for analysis. In total 140 LAI measurements were performed using four LAI-2000 instruments and, in order to compare them, sixteen inter-comparison measurements were also performed in four different types of crops (Sugarbeet, Potato, Corn and Garlic) in the same spot at the same time (see Figure 6.8). A good agreement was found except for a Sugarbeet spot in which the LAI value was underestimate for one instrument.

The numbers of LAI measurements for each crop and the value are plotted in Figures 6.6 and 6.7:

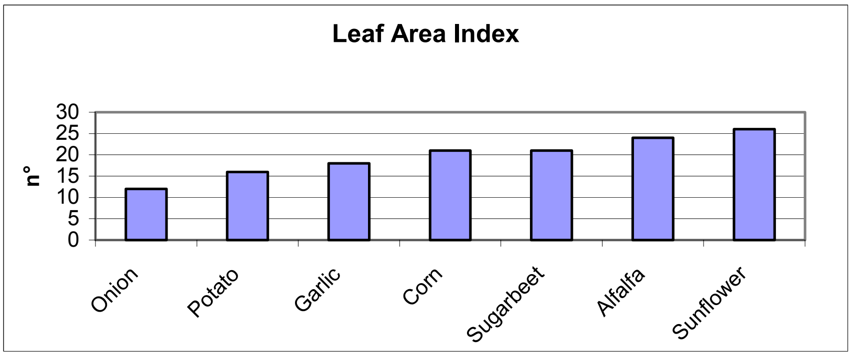

Figure 6.6. LAI measurements for each crop.

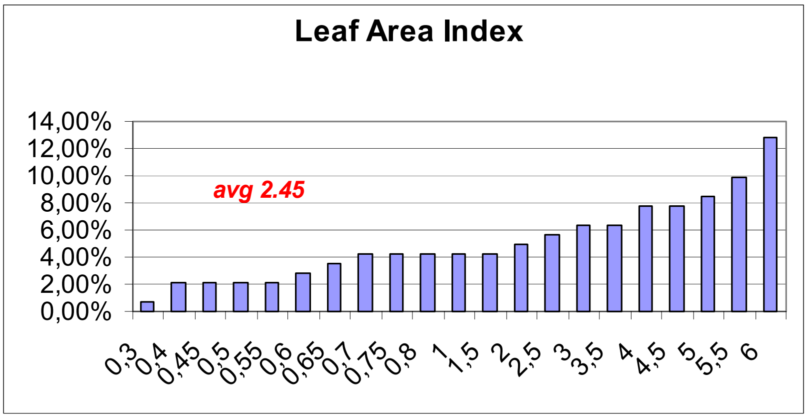

Figure 6.7. LAI values and percentage of measuremets associated to each value

Alfalfa crop. Field A-1.15th of july.SPARC-2004.

Alfalfa crop. Field A-1.15th of july.SPARC-2004.

Corn crop. Field C-1.15th of july.SPARC-2004.

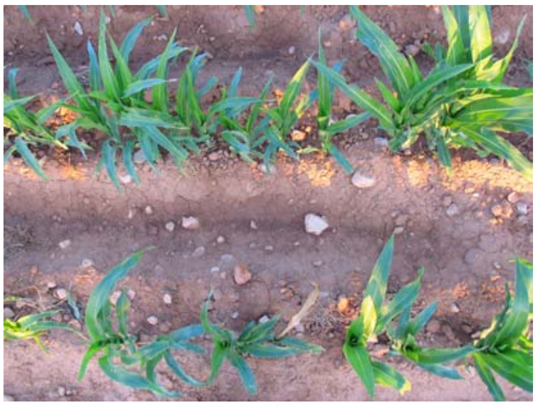

Corn crop. Field C-1.15th of july.SPARC-2004.


Garlic crop. Field G-1.


Garlic crop. Field G-1.16th of july.SPARC-2004.


Onion crop. Field On-3.16th of july. SPARC-2004.


Potato crop. Field P-2.16th of july.SPARC-2004


Potato crop. Field P-2.16th of july.

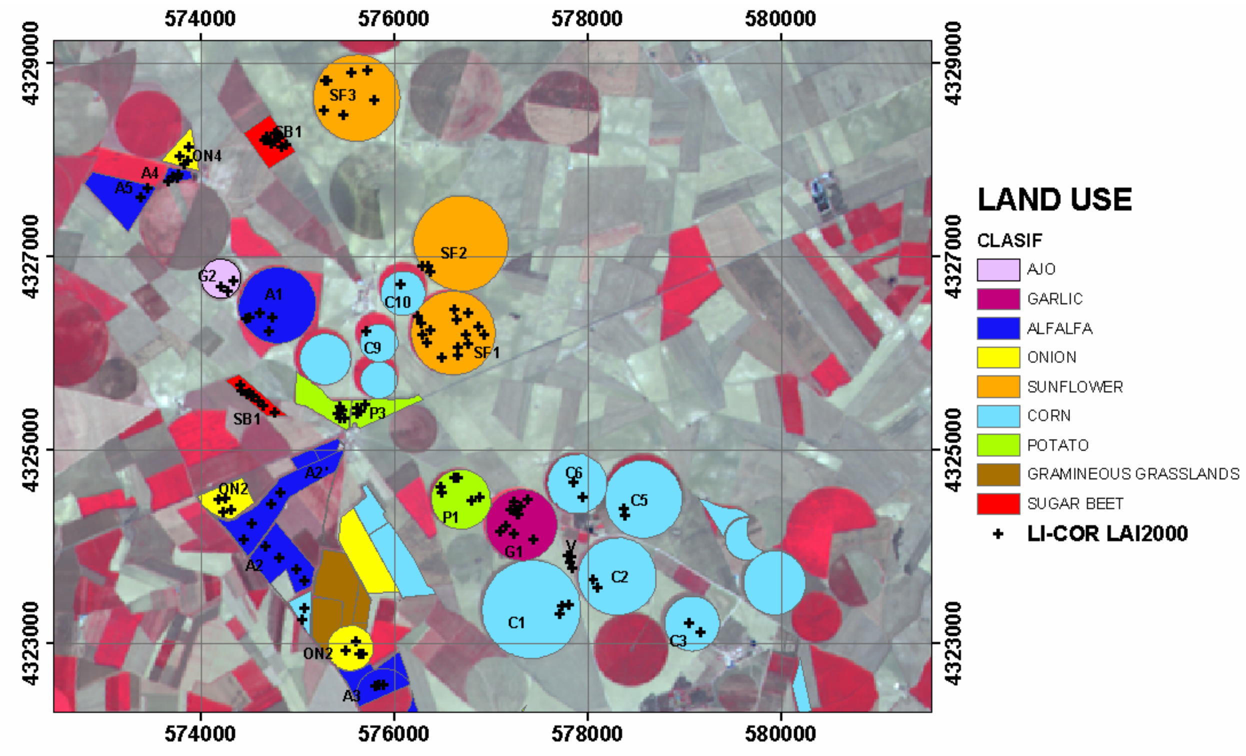

Figure 6.8. Map of LAI-LICOR sampling scheme.

LAI-LICOR measurements and their SEL associated by the instrument were checked and compared per crops. Results can be seen at Figure 6.9 where each point corresponds to each ESU described before. Once they were checked, comparison to SPARC-2003 acquired data and their behaviour versus the rest of biophysical parameters under analysis were made and obtained results are described at PART-II of this report.

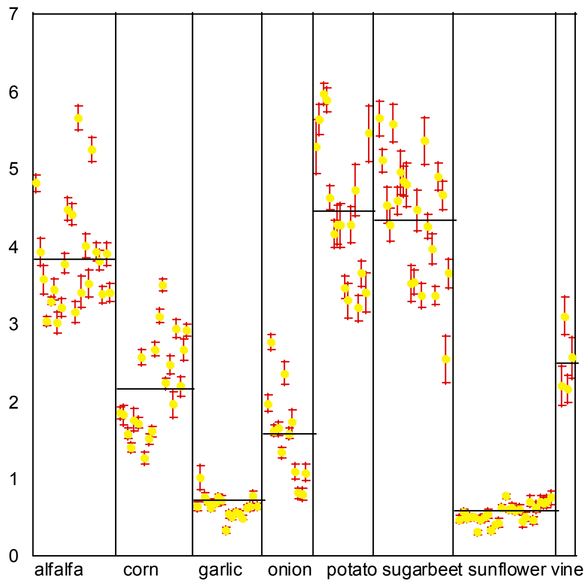

Figure 6.9. LAI-LICOR measurements (in yellow) and SEL (in red) got for each ESU let to characterise each crop. SPARC-2004 data campaign.

6.2.3 Fractional Vegetation Cover (FVC) from hemispherical photographs

Hemispherical canopy photography is a technique for studying plant canopies via photographs acquired through a hemispherical (fisheye) lens from beneath the canopy (oriented towards zenith) or placed above the canopy for downwards looking. Therefore, it can be used for any canopy type.

A hemispherical photograph allows you to derive, among others, vegetation structural characteristics such as, gap fraction, leaf area index (LAI) and average leaf inclination angle (ALA). It provides a permanent record and is therefore a valuable information source for position, size, density, and distribution of canopy gaps. The view angle is equal to 183º and allows the gap fraction to be evaluated in all viewing directions, which increases the accuracy of the derived biophysical variables (LAI, ALA).

Figure 6.10. NIKON Coolpix5000 with the NIKON FC-E8 fisheye converter.

Sampling design with the hemispherical camera

The main objective of the sampling was to estimate a high-resolution biophysical map by means of a transfer function which accounts for the mean and variability presented in the area. The transfer function is used to establish a relationship between the biophysical variable of interest measured over the ESUs and the corresponding high spatial resolution radiometric response (Martínez et al., 2004b).

The sampling design performed with the hemispherical camera was extended over a larger area around the Barrax test site in order to (i) characterize the main crops and other cover types that were not found in the Barrax test site (e.g. Forest and Shublands), (ii) have enough measurements in order to use some of them as validation points and (iii) analyze other sampling strategy. The sampling strategy adopted with the camera was different from the Li-COR LAI2000 since only one digital camera was available during the campaign as opposed to four LI-COR LAI2000 instruments. In this case, the strategy was mainly based on the characterization of each crop with at least 6 ESUs and one ESU per field. For those crops with minor presence in the area (e.g. Garlic and Sugar Beet), all the measurements were distributed inside one field. As a result, only a minimum of 6 ESUs were collected for those crops with major presence in the area, such as Alfalfa, Corn and Onion.

The ESUs have similar dimensions to the high-resolution radiometric data used to derive the high-resolution biophysical map, in our case 20×20 m2 of the SPOT image and the sampling design inside an ESU was adopted from the VALERI methodology (Baret et al., 2004). The biophysical estimate for each ESU was the average of twelve measurements acquired according to two different schemes. For homogeneous canopies (e.g. Sugar Beet, Potato, Corn, Onion), the scheme a shows in Figure 6.11 was used for the Potato, sugar Beet, Corn, Alfalfa and Onion crops. On the other hand, the scheme b was used for canopies distributed in rows such as SunFlower and Vineyard crops. In these cases, the measurements were acquired along a direction that was not parallel to the rows in order to sample the row effect and the variability within the ESU.

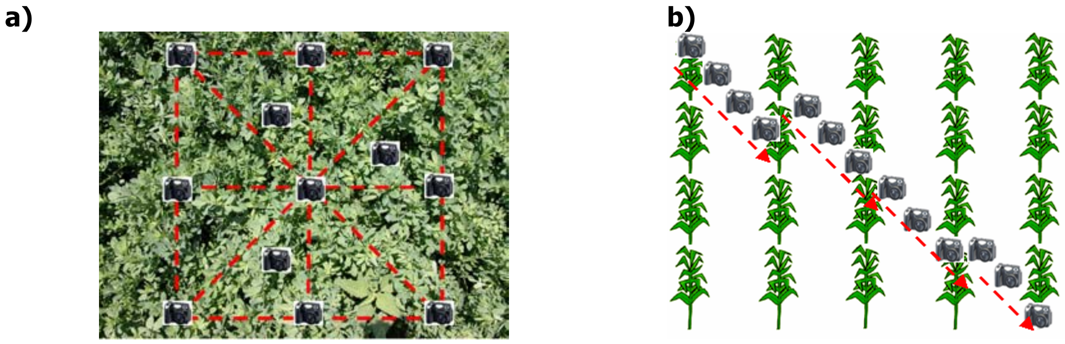

Figure 6.11. Two different sampling strategies for (a) homogeneous and (b) row crops ESU (20×20 m^2). The center of the ESU was geolocated using a non differential GPS.

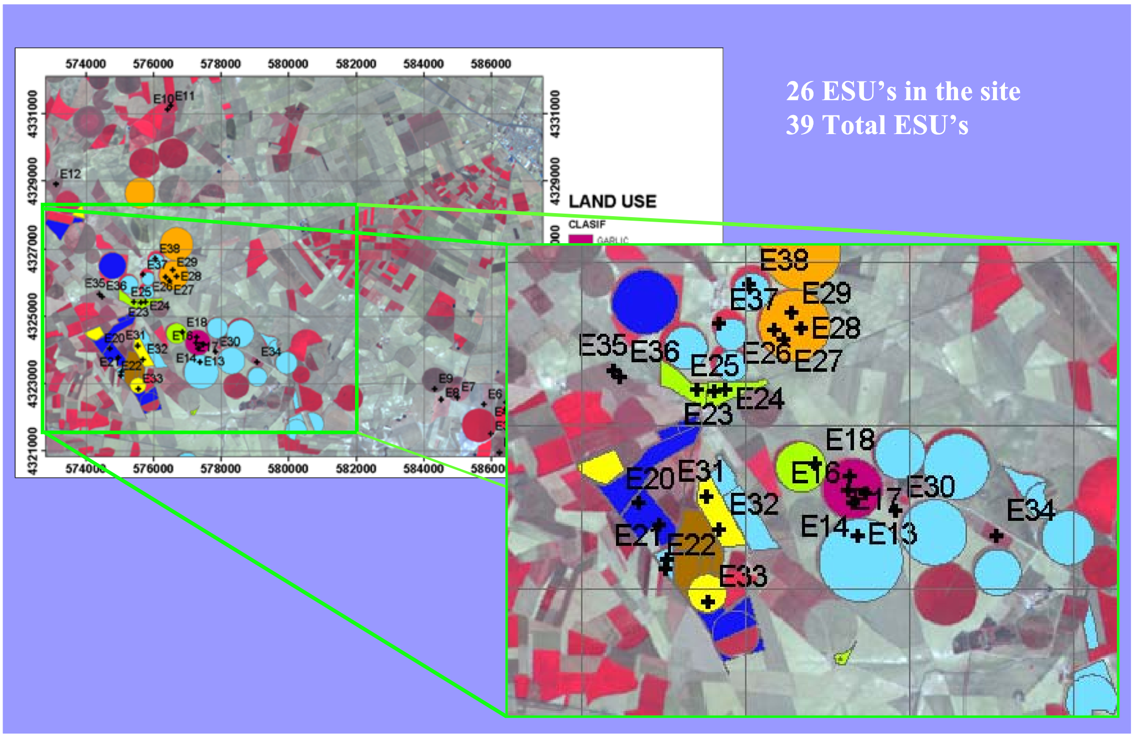

Figure 6.12. Map of hemispherical camera sampling scheme.

A total number of 39 ESUs were measured with the hemispherical camera, 26 of them inside the test site, along the five central days of SPARC-2004 campaign. Ten different crops were characterised by this method, all of them showed at next Figure.

The hemispherical photographs were processed using a specialized software package (CAN-EYE) developed at INRA-CSE Avignon. The CAN-EYE software allows obtaining structural parameters of the canopy such as LAI, FCV and ALA[1] by estimating the gap fraction over all the hemispherical photographs taken within an ESU. The gap fraction is estimated by classification techniques whereas LAI and ALA are derived from an inversion Poisson model, which relies upon look up table techniques using the zenith ranges of (0º-10º) and (10º-80º) for the LAI and ALA, respectively (Figure 6.14). The software provided, among others, the monodirectional average gap fraction of the 12 photographs of the ESU over a given view zenith range, in our case (0º-60º) (Figure 6.15). From this result, different structural parameters were derived, such as the true and effective LAI average for this zenith range, the clumping factor as a function of the view zenith angle, the LAI at 57.5º view angle, the ALA, the FVC for the view zenith range of (0º-10º) and the standard deviation of the LAI estimated at the angle 57.5º (Martinez, et al., 2004).

[1] Average Leaf Inclination Angle

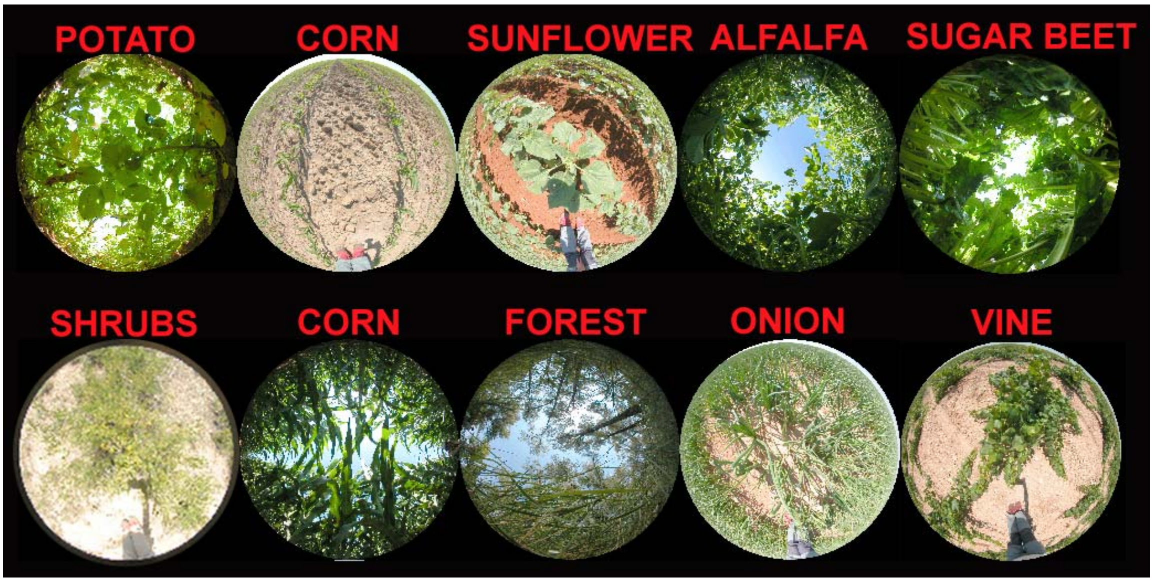

Figure 6.13. Vegetation characterised with the hemispherical. SPARC-2004 data campaing.

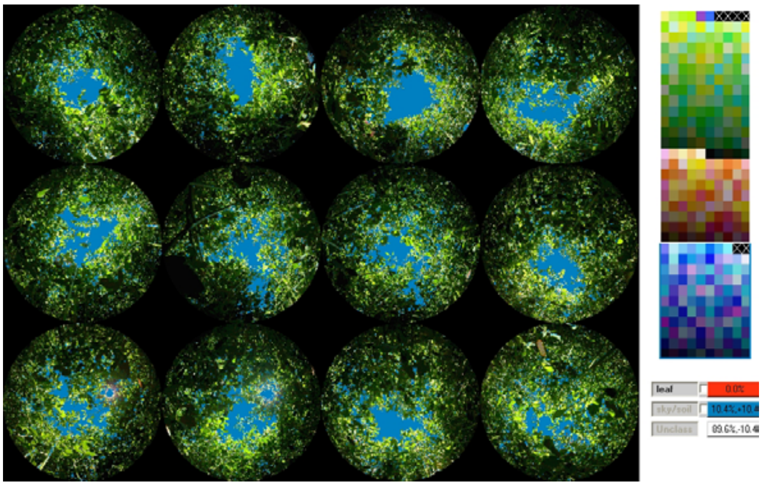

Figure 6.14. An example of the preliminary processing analysis. This Figure shows the classification process performed over the 12 photographs acquired inside an Alfalfa ESU. In this case, a 10% of the image is classified as sky.

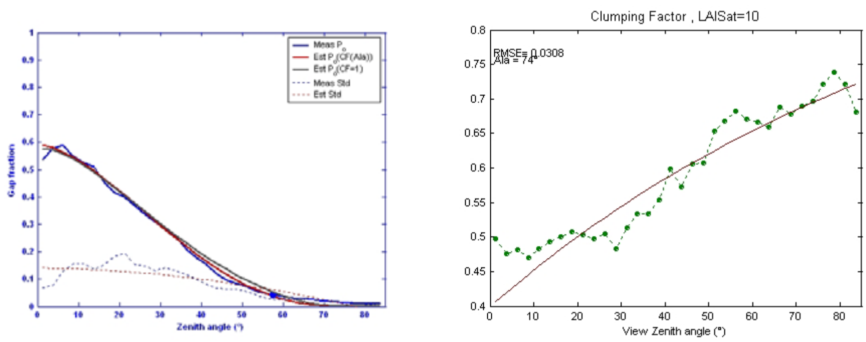

Figure 6.15. Some of the outputs derived from CAN-EYE processing. Figure on the left shows the monodirectional gap fraction measured and estimated. Figure on the right shows the clumping factor as a function of the view zenith angle.

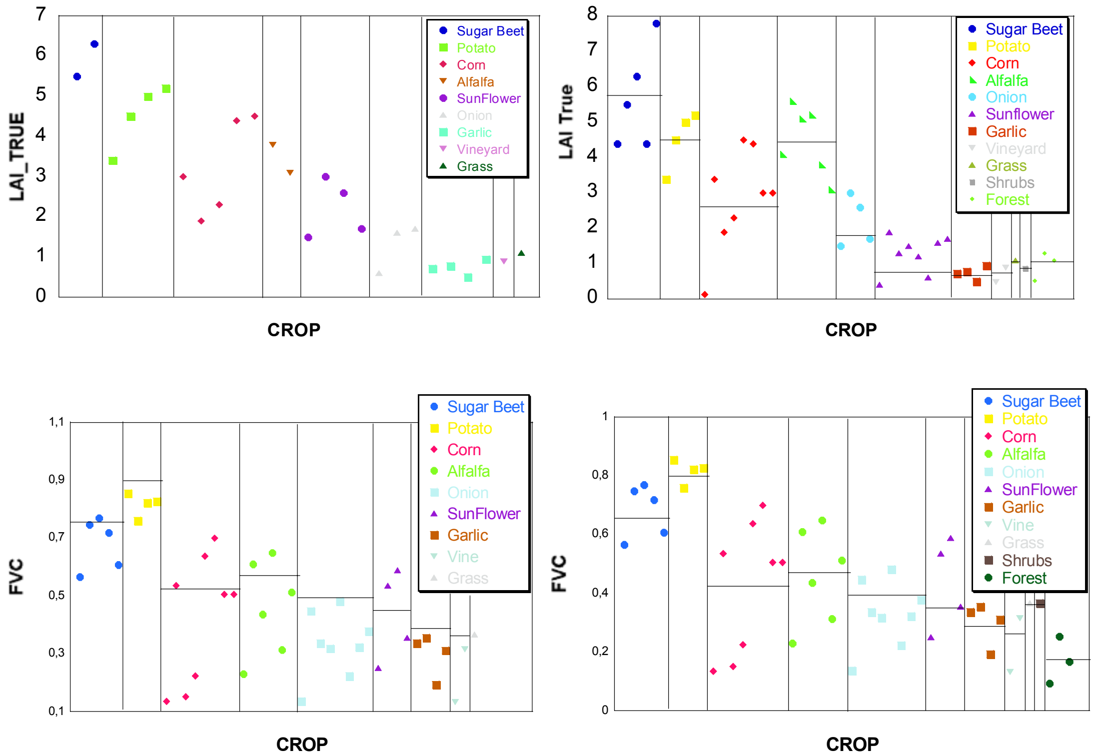

Figure 6.16. FVC and LAI-true the outputs derived from CAN-EYE processing. Figures on the left shows results from the Barrax test site measurements and Figures on the right shows the derived values corresponding to the large sampling area.

LAI-true and FVC derived from CAN-EYE processing were checked and compared per crops. Results from the Barrax test site and the derived values corresponding to the large sampling area can be seen at Figure 6.16 where each point corresponds to each ESU described before. Once they were checked, both of the methods were compared, relative errors calculated and their behaviour versus the rest of biophysical parameters under analysis were compared and obtained results are described at PART-II of this report.

6.2.4 Leaf chlorophyll content.

The leaf chlorophyll content was measured with the CCM-200 Chlorophyll Content Meter (Figure 6.17). Observation of changes in chlorophyll content has applications in basic photosynthesis research. The CCM-200 illustrates changes in chlorophyll content which can be correlated to plant health and condition. This data can even be used to compliment chlorophyll fluorescence and gas analysis measurements.

However, it performed relative measurements, so calibration measurements might be made before using laboratory analysis methods. Leaf disks were cut with a calibrated cork borer, wrapped in aluminum foil, frozen in liquid-nitrogen, and stored (still wrapped in foil) at -20 °C. Leaf pigments were later extracted with acetone in the presence of Na ascorbate and stored as described previously (Abadía and Abadía 1993). Pigment extracts were thawed on ice, filtered through a 0.45 µm filter and analyzed by an isocratic HPLC method based on that developed by De las Rivas et al. (1989). Two steps (instead of three) were used: mobile phase A (acetonitrile: methanol, 7:1, v:v) was pumped for 3.5 min, and then mobile phase B (acetonitrile :methanol: water: ethyl acetate, 7:0.96:0.04:8 by volume) was pumped for 4.5 min. To both solvents 0.7% (v:v) of the modifier triethylamine (TEA) were added (Hill and Kind 1993) to improve pigment stability during separation. All chemicals used were HPLC quality. The column was equilibrated before injecting each sample by flushing with mobile phase A for 5 min. The analysis time for each sample was 13 min, including equilibration time.

Chlorophyll has several distinct optical absorbance characteristics that the CCM-200 exploits to measure relative chlorophyll concentration without destructive sampling. Strong absorbance bands are present in the blue and red but not in the green or infrared bands, hence the green appearance of a leaf. By measuring the amount of energy absorbed in the red band an estimate of the amount of chlorophyll present in the tissue is possible. Measurements in the infrared band show absorbances due to cellular structure materials. By using this infrared band to quantify bulk leaf absorbance, factors such as leaf thickness can be taken into account in the CCI (Chlorophyll Content Index) value.

Figure 6.17 Chlorophyll Content Meter CCM-200

Acquired data

Data acquisition took place on 15, 16, 17 and 18th July, between 11 a.m. and 15 p.m (local time). Chlorophyll samples were measured independently on the rest of biophysical parameters due to the measurements protocol followed. Moreover, a new set of sampling points was defined using the GPS device, due to the search of ESUs geolocated for the rest of the vegetation measurements slowed down the process considerably.
Eighteen ESUs were sampled in thirteen different fields, characterising a total number of eight different crops (Figure 6.18). Around 50 CCM-200 measurements were taken per ESU, while all of the species were well represented in order to perform a proper analysis of the measurements.

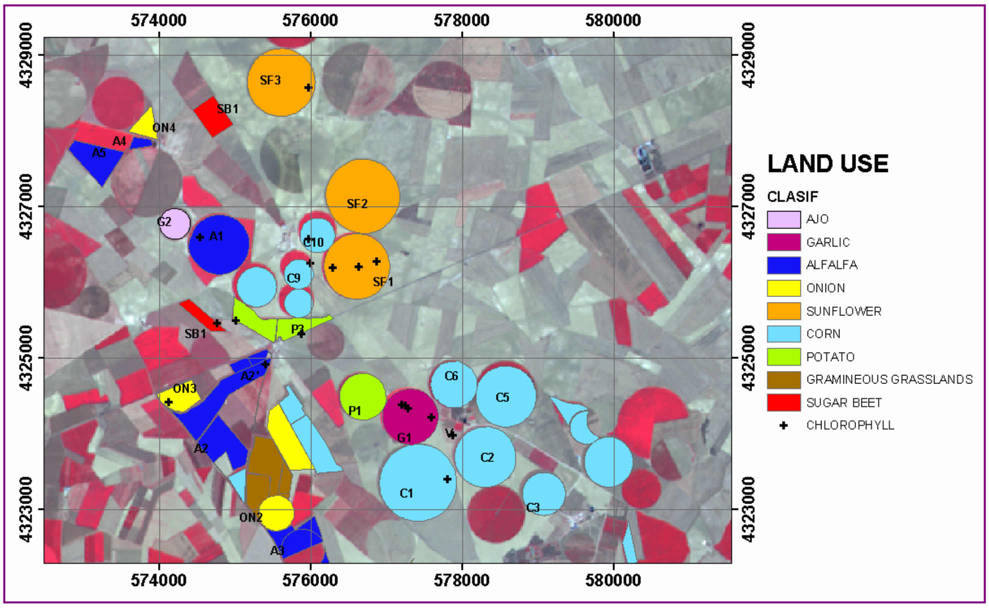

Figure 6.18. Map of CCM-200 sampling scheme.

Data acquisition was made according to two guidelines. On one hand, measurements were sampled from different points to characterize the chlorophyll content for the different species. On the other hand, leaves samples from each of the ESUs were collected and measured by means of the chlorophyllometer, in order to perform a second calibration of the device, different to the one made in 2003. Although this second objective made the process slower, a considerable improvement in the derived chlorophyll values is expected.

GPS coordinates and the acquisition starting time were annotated for all the ESUs. Sampling points were located inside the fields, in points were boundary effects were not noticeable. Since the CCM-200 instrument is designed to work with leaves larger than 1 cm of diameter, big leaves were chosen in advance. As far as possible, leaves veins were avoided due to they might perturb the measurement (Figure 6.19). The chlorophyllometer is not able to measure the thickest leaves, as the radiation emitted can not cross them. Onion and garlic leaves were cilindrical shaped and leaves scissors were used to split different layers for plants with such thick.

Figure 6.19. CCM-200 sampling for corn leaves

Figure 6.20. CCM-200 measurement protocol

Once the leaf was inside the CCM-200 window (Figure 6.20), three straight measurements were made in the same part of the leaf. When measurement dispersion observed for an ESU was large, measurements continued until dispersion decreased sufficiently.

From the leaf fraction measured with the chlorophyllometer two samples were extracted for the posterior instrument calibration in the laboratory. They were cut by means of a copper cylinder with a sharp edge (as shows Figure 6.21), leading to a sample with an area of (0.785 ± 0.016) cm^2. These samples were located inside a previously numerated aluminium foil to keep them (Figure 6.22), and were preserved in liquid Nitrogen. Ten leaf samples were collected and 50 chlorophyllometer were measurements from each ESU.

Figure 6.21. Leaves were cut by means of a copper cylinder with a sharp edge.

Figure 6.22. Samples were located inside a previously numerated aluminium foil and preserved in liquid Nitrogen

Results obtained for chlorophyll from the CCM-200 sampling are showed in table 6.6: crops characterized, ESUs sampled inside each crop, number of measurements per ESU, mean chlorophyll content value corresponding to these measurements and mean values for each crop with the standard error associated.

Comparisson between SPARC-2003 and SPARC-2004 chlorophyll content mean values obtained per crops gave us a similar values excep for garlic an onion (Figure 6.23). Their leaves were cilindrical shaped and difficulted chlorophyllometer measurements and the different phenologycal state of those crops during the two SPARC campaigns justified differences found from comparisson.

Table 6.6. Chlorophyll content sampling results

CROP	ESU	Number of measurements	Chlorophyll (µg cm-2)	Mean value per crop
	C1-D1	53	49.3 ± 0.4	
	C9-D1	56	52.58 ± 0.6	
Corn	C10-D1	87	53.06 ± 0.7	**51.6 ± 0.8**
Sugar beet	B1-D1	56	48.9 ± 0.62	**48.86 ± 0.62**
Onion	On3-D1	58	33 ± 2	**33 ± 2**
	G1-D1	22	53 ± 2	
	G1-D2	43	51 ± 2	
	G1-D3	46	47 ± 2	
Garlic	G1-D1	77	44 ± 2	**49.2 ± 2**
	P2-D1	60	37.2 ± 0.7	
Potato	Px-D1	68	35.7 ± 0.6	**36.5 ± 0.7**
	A1-D1	95	50 ± 0.4	
Alfalfa	A2-D1	45	48.5 ± 0.7	**49.3 ± 0.7**
Vine	V1-D1	135	36.1 ± 0.7	**36.1 ± 0.7**
	SF1-D1	52	43.4 ± 0.3	
	SF1-D3	58	43.7±0.3	
	SF1- D1	62	39.6 ± 0.4	
Sunflower	SF3-D1	103	44.2 ± 0.5	**42.7 ± 0.5**

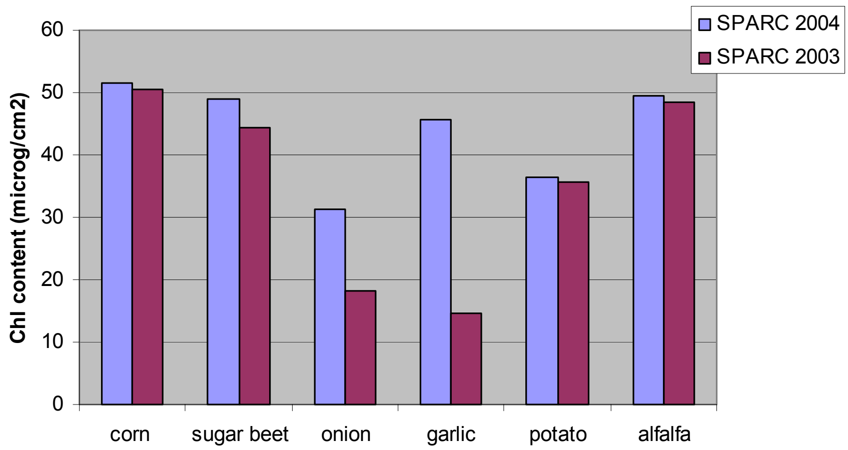

Figure 6.23. Chlorophyll content mean values per crops.
SPARC-2004 data in red compared to SPARC -2003 data in blue.

Mean chlorophyll content values corresponding to SPARC-2004 and SPARC-2003 measurements, mean values for each crop and the standard error associated can be seen at Figure 6.24 where each point corresponds to each ESU described before. Their behaviour versus the rest of biophysical parameters under analysis is described at PART-II of this report.

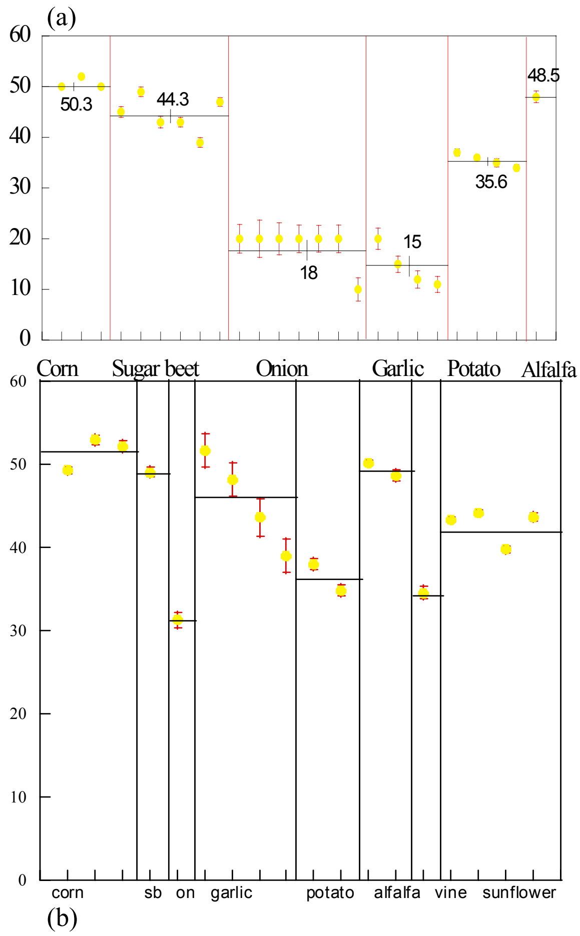

Figure 6.24. Chlorophyll content mean values per ESU with standard error bars and mean value for each crop: (a) SPARC -2003,(b) SPARC-2004.

6.2.5 Volumetric soil water content

The Time Domain Reflectometry belongs to the category of "capacitance methods" (Kutílek and Nielsen, 1994), which are based on in-situ measurement of soil dielectric behaviour.
This method has been introduced by Topp in early '80 but it has proved his reliability in many field and laboratory applications; it is based on the measurement of propagation velocity of a pulse along a transmission line embedded in the soil, which is related to an "apparent" permittivity and thus to the actual soil water content. The measurement is performed by installing two conductors of known length in the soil and sending a steep pulse along this line by means of a special cable tester. The signal travel along this transmission line with a velocity that depends on the medium dielectric behaviour; at the end of the line the signal is reflected back to the tester, which can register the transit time, thus the propagation velocity is calculated. This technique has a low sensitivity to probe geometrical characteristics and to soil type and it has been possible to define a unique calibration relationship which holds for most practical applications, as shown later.

Relationship between the dielectric constant and the soil water content

Several approaches have been tried out to relate the volumetric soil water content θ to the dielectric constant εa determined by means of TDR. In many cases, empirical relationships have been defined by simply interpolating observed data without paying too much attention to their physical interpretation. A commonly used "universal calibration formula", in the form of a third degree polynomial function, has been proposed by Topp et al. (1980):

$$\theta = -5.3\cdot 10^{-2} + 2.9\cdot 10^{-2}\,\varepsilon_a - 5.5\cdot 10^{-4}\,\varepsilon_a^2 + 4.3\cdot 10^{-6}\,\varepsilon_a^3$$

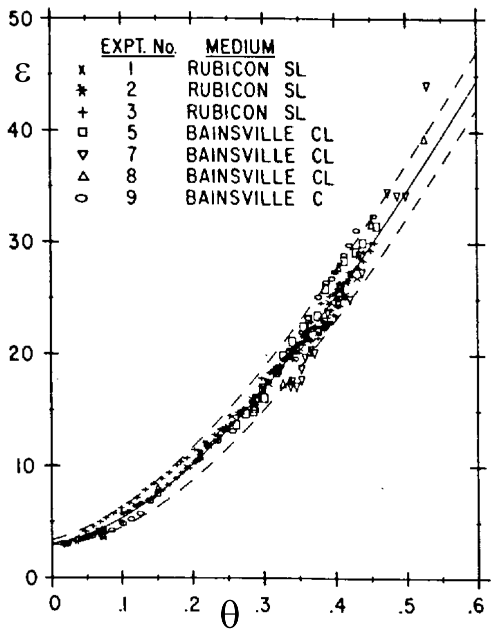

Figure 6.25: Empirical calibration formula (Topp et al., 1980)

This expression has been derived from a large laboratory data set considering different types of soils and for frequencies not higher than 1 GHz. The function in equation gives reliable results in the range 0.05<θ<0.60 if applied to mineral soils without high clay fractions and organic matter, but it does not match exactly the actual relationship between θ and ε_a when this latter approaches the extreme values of 1 or that of free water (εa≈80) or in soils with elevated organic matter contents.

Recently, a physically based approach has been tried out by relating the apparent dielectric permittivity of a multiple-phases mixture to the ε_a values for each component and to their corresponding volumetric fraction. This approach leads to an alternative formula as follows:

$$\theta = a\sqrt{\varepsilon_a} + b \quad .$$

The square root of the dielectric constant is commonly indicated as the "*refraction index*", n. The a and b parameters should be considered as purely empirical variables.
The data set used for defining the Topp's formula in Equation was re-analysed by Heimovaara (1993), which suggested the following relationship between θ and n to be applied for $1{,}5<n<7{,}5$ with high correlation:

$$\theta = 0{,}103 \cdot n - 0{,}135$$

Since the beginning, the large interest in TDR technique was given by the reliability of "universal" calibration formulae which validity has been proven in most practical applications. For precision measurements, the use of these general relationships is suitable only when no absolute determination of θ is required, i.e. when monitoring the temporal variation of soil moisture in a fixed location (Zegelin et al., 1992). Indeed, in most cases the maximum absolute error of estimate is 0.05 (Jacobsen et al., 1995); if a better accuracy is needed, a soil-specific validation and calibration should be performed (Figure 6.26). In most critical situations, other influencing factors should also be considered, i.e. the effect of large temperature variation on the value of water permittivity ε_w [2] when the measurements are taken near the soil surface, as shown by Roth et al. (1990).

Description of TDR instrumentation

The main components of a typical TDR instrumentation are schematically drawn in Figure 6.26. The electronic apparatus includes a control unit, needed for the synchronisation of the pulse generator and the receiver, and the output device (generally a LCD monitor) and related peripherals (communication port and/or dot matrix printer). The apparatus is connected with a coaxial cable to the transmission line (TDR probe), which may have different shapes and configurations.

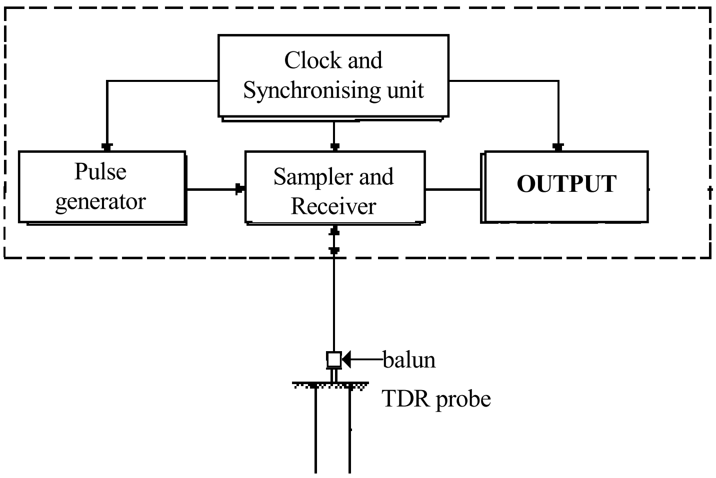

Figure 6.26. Schematic view of TDR apparatus (adapted from Topp and Davis, 1985)

[2] The dependence of water dielectric permittivity ε_w on the temperature (T°C) may be expressed by the following relationship (Hasted, 1973):
$\varepsilon_w = 87{,}74 - 0{,}4001T + 9{,}398 \cdot 10^{-4} T^2 - 1{,}410 \cdot 10^{-6} T^3$

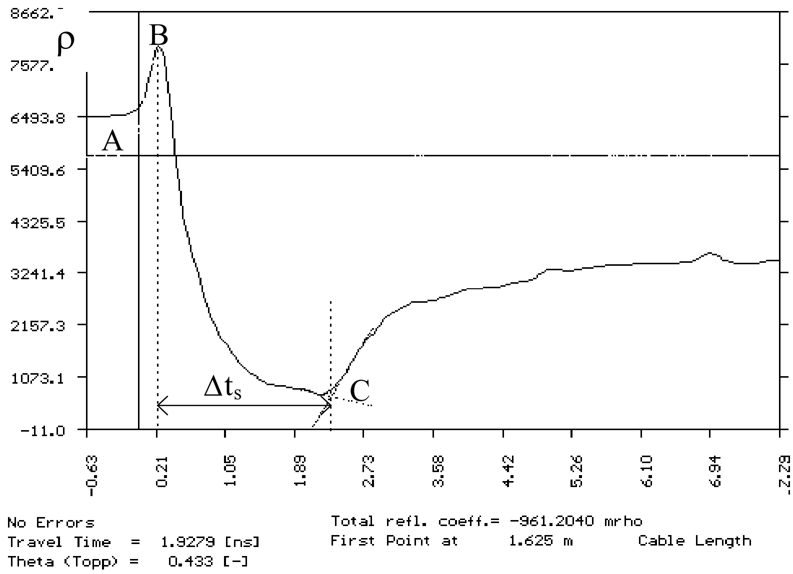

Figure 6.27. Example of TDR output with a balanced parallel line in a wetted soil**.**

The returning signals are superimposed to the emitted ones and they are detected by the receiving unit, with a voltage decrease or increase depending on the phase of the reflection. By means of its built-in hardware and firmware, the receiving unit samples and records the returning signal at very small time steps; in the same time, the output device provides a graph of the reflected voltage versus time.

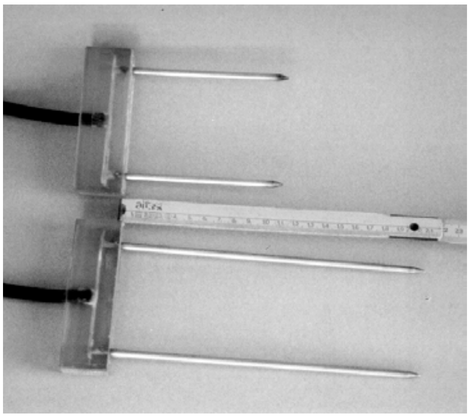

Figure 6.28. Balanced probes of different length.

Widely used TDR equipment is the Tektronix cable tester Mod.1502 C, which has been conceived as a portable measuring device and it can be easily connected to a personal computer through its communication port. In this case, the step-pulse is characterised by amplitude of 300 mV, a rise time of 0.2 ns and duration of 25 μs corresponding to a theoretical frequency range from 20 kHz and 1.75 GHz. The effective frequency bandwidth is certainly restricted by attenuation effects induced by cable connections; the extent of this attenuation, which mainly affects the higher frequencies range, largely depends on the quality and on the length of cables. From the analysis of several estimates of soil dielectric permittivity on different types of soils by means of TDR, Heimovaara et al. (1994) estimated a frequency range between 200 MHz and 1 GHz, thus confirming the assumptions reported in previous section.

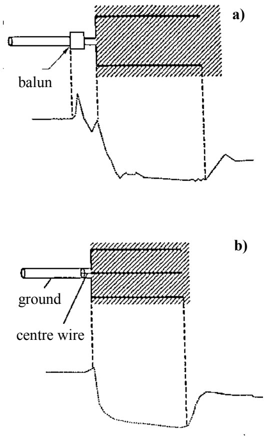

Figure 6.29. Parallel balanced (a) and unbalanced (b) TDR probes (from Whalley, 1993)

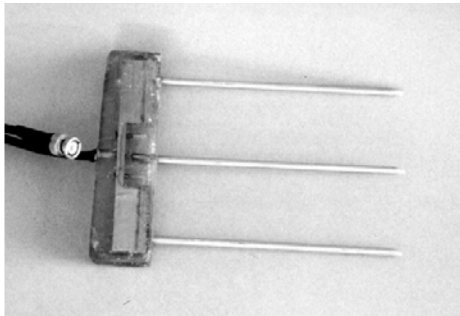

Figure 6.30. Unbalanced three-wire probe (L=14 cm) with coaxial cable and connector.

The probe inserted into the soil constitutes the pulse transmission line which can be electrically balanced or unbalanced. The balanced lines (Figure 6.28) are more widely used and they are made of parallel and cylindrical metallic conductors; the soil between them is the dielectric medium (Figure 6.29-a). The probe is connected to the TDR unit by means of a coaxial cable or a parallel shielded cable; every connection represents impedance mismatching which causes a partial reflection of energy.

Data acquisition

TDR measurements were taken with the instrument in six different fields: Bare soil, corn (C1), sunflower (SF1), potato, onion (On-3) and onion (On-5). A total number of 31 samples were measured and GPS geolocated along the 15th and 16th of july, within the SPARC-2004 airborne data acquisition.
Results are showed in tables 6.7 and 6.8. An exahustive analysis will be presented at the Final Report document.

Table 6.7. TDR measurements.15th of july. SPARC-2004 campaign.

(15/07/2004)

Est-30N	Nord-30N	Probe	mΔ	Ω	
					Bare Soil
577907	4323214	329	0,4	136	
577920	4323203	329	0,32	278	
577928	4323196	329	0,248	545	
577940	4323196	329	0,252		
577958	4323175	329	0,376	143	
					Corn (C1)
577861	4323261	328	0,316	75	
577861	4323261	329	0,592	50	
577867	4323277	328	0,252	121	
577867	4323277	329	0,532	66	
577841	4323272	328	0,26	123	
577851	4323260	328	0,274	112	

Table 6.8. TDR measurements.16th of july. SPARC-2004 campaign.

(16/07/2004)

Est-30N	Nord-30N	Probe	mΔ	Ω	
					Sunflower (SF1)
576329	4326005	330	0,244	130	
576351	4326015	328	0,27	94	
576339	4325995	330	0,272	78	
576353	4326003	328	0,268	80	
576338	4325995	330	0,284	84	
576345	4326005	328	0,252	104	
					Sunflower (SF1)
576484	4326083	328	0,25	120	
576480	4326088	330	0,294	72	
576466	4326065	328	0,268	92	
576475	4326073	330	0,274	104	
576462	4326076	328	0,276	89	
576468	4326088	330	0,32	57	
					Potato
575396	4325383	328	0,25	208	
575403	4325382	328	0,244	190	
575399	4325383	328	0,264	170	
575385	4325384	330	0,26	216	
575391	4325403	328	0,244	218	
					Potato
575471	4325346	330	0,174	455	
575473	4325347	328	0,186	330	
575498	4325356	330	0,18	350	
575496	4325338	328	0,174	405	
					Onion (ON3)
574188	4324464	328	0,27	133	
574181	4324464	330	0,258	165	
574206	4324485	328	0,246	148	
574206	4324485	330	0,272	116	
574212	4324468	330	0,211	208	
574212	4324468	328	0,204	186	
					Onion (ON5)
574335	4327364	328	0,174	400	
574940	4327373	330	0,172	485	
574932	4327388	328	0,098	780	
574315	4327367	330	0,11	920	

6.2.6 Canopy geometrical structure characterization.

This section describes the measurements that were done during the SPARC 2004 campaign for a detailed reconstruction of plants and fields geometrical structure.

Different canopy parameters and field geometrical properties were measured inside the main crops of the study area: 6 corn plots, garlic, alfalfa, onion, potatoes, sugar beet, vineyard and sunflower.

Measurements protocol

The center and the diameter of the plot were the first field geometrical properties that were measured for all the plots by using a Landsat georeferenced image. Inside the field, the plants were distributed in rows. Orientation of the rows was measured with respect to the north and it was considered a constant for all the fields. If we do a zoom inside the field:

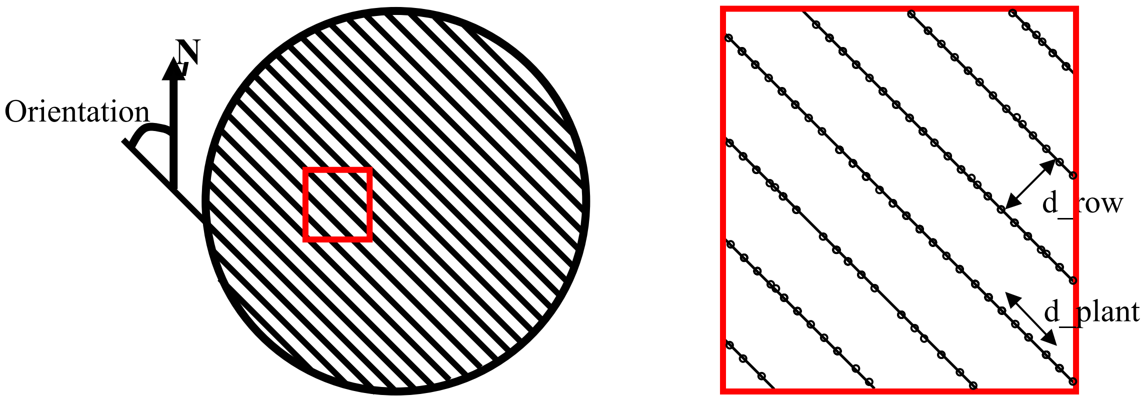

Field geometrical properties

The idea is to be able to reconstruct the position of each individual plant inside the field. To do that, we measured the row distance (that is considered as a constant), and we also did some measurements to obtain the mean value and the standard deviation of the plant distance for each crop. Finally we asign a position for each individual plant using a constant value for the center of the plot, the diameter, the orientation and the row distance, and a random value for the plant distance, with a normal distribution, accepting only the values that were between the maximum and minimum plant distance measured in the field.

Once we have defined the individual position of each plant inside the field, the next stage is to do a detailed 3D reconstruction of each individual plant. The idea is to reconstruct the different crops with the same model. For example, from the corn plant that we can see in Figure 6.31, we can obtain this 3D model.
On one hand, we measured the main stm, defined by the height, the thickness and the angle with the vertical. On the other hand we measured for each secondary stem or leaf the height where the leaf starts, the distance from the main stem to the beggining of the leaf, the angle with the vertical and the orientation with respect to the north. Each leafwas defined as a triangle, with a base and height. Measurement of this properties let to modelice the sun flower, alfalfa, garlic, onions, corn and sugar beet canpy structure.

Finally, we have obtained some statistical measurements of the plant properties, and for each one we have a mean value, and a standard deviation. To be realistic, we only accept the values that are between the maximum and minimum value measured in the field.

The final result is a text file where for each individual plant inside the plot, we have all the properties described before, as we can see below:

Crop, x, y, stem h, stem ang., stem thickness, nº of leaves
leaf 1, h, d0, orientation, ang., base, length
leaf 2, h, d0, orientation, ang., base, length
...
leaf n, h, d0, orientation, ang., base, length

First line describes the properties of the main stem: crop, x and y possition in UTM coordinates, height of the stem, angle of the stem with the vertical, thickness of the stem and number of leafs. We also have one line for each leaf of the plant with these properties: number of the leaf, height where the leaf starts, the distance from the main stem to the beggining of the leaf, orientation with respect to the north, the angle with the vertical, the base and lenght of the triangle.
With these measurements we will be able to do a detailed 3D reconstruction of the plants in Barrax during the SPARC 2004 campaign. These models can be used to measure different canopy geometrical properties as LAI, GAP, Fcover, Clumping, etc, and for advanced 3D reflectance modelling models.

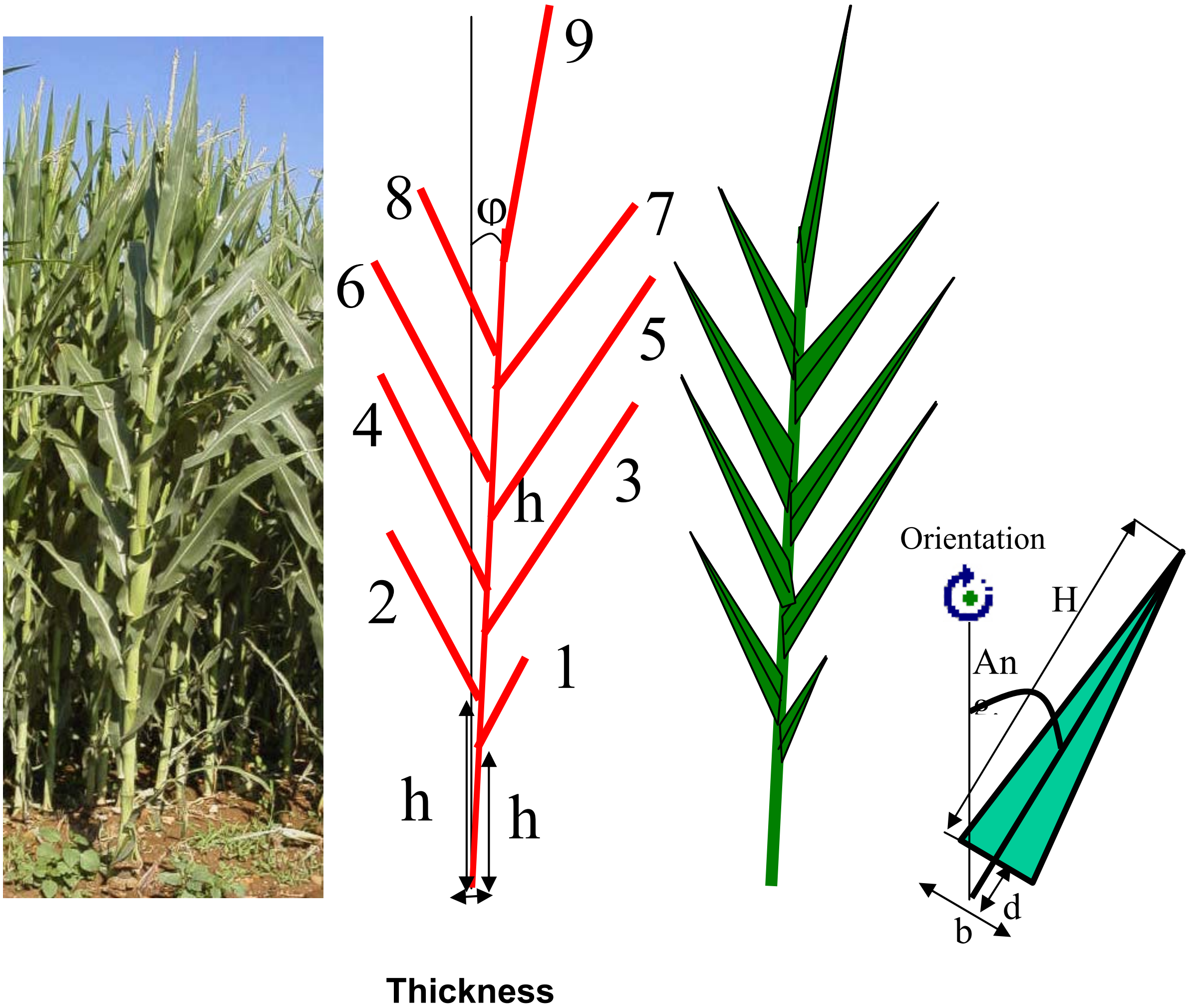

Figure 6.31.This model is defined with some geometrical properties of the plants that can be easilly measured in the field.

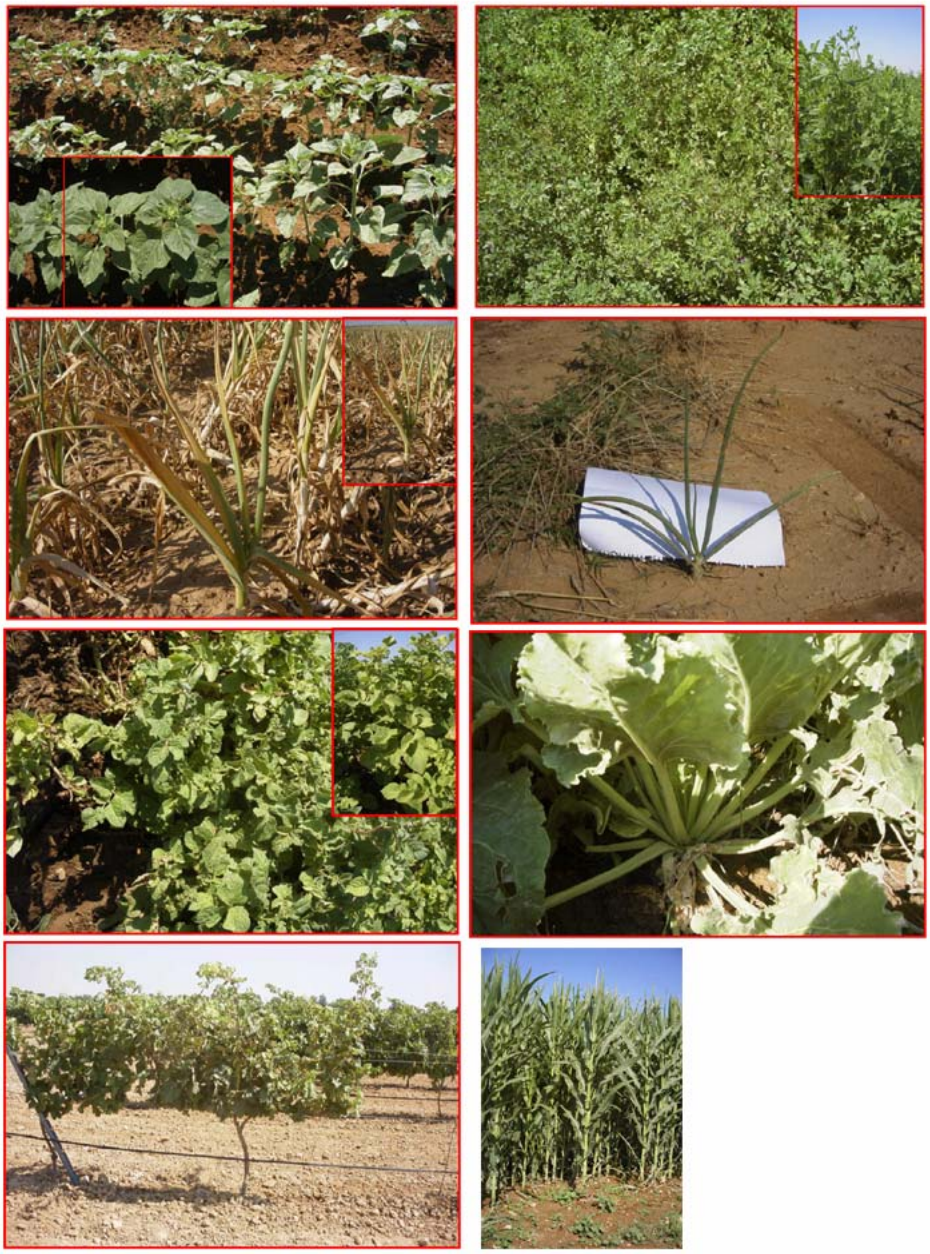

Figure 6.32 Different crops measured in Barrax to characterice their structure.

7 - REFERENCE METEOROLOGICAL DATA

The University of Castilla-La Mancha, through the "Escuela Técnica Superior de Ingenieros Agrónomos", operates three agro-meteorological stations in the study area of Barrax (fig. 7.1):

a) Tiesas-Anchor Station (39º 02’ 31” N; 2º 04’ 55” W)
b) Tiesas-Lysimeter Station (39º 03’ 30” N; 2º 05’ 24” W)
c) Blancares Station (39º 06’ 45” N; 2º 06’ 40” W)

These stations belong to the Permanent Station Network of the University of Castilla-La Mancha and are connected by modem with the central computer at the Institute for Regional Development in Albacete. The data are compiled and stored automatically for later treatment, as well as being accessible in real time. Measurements are done by all sensors every 30 seconds and are stored every 10 minutes.

Figure. 7.1. Las Tiesas-Anchor and Lysimeter permanent meteorological stations at Barrax.

The following measurements are available from each station:

- Tiesas-Anchor Station

Anemometer (10m)	Soil moisture (0,90m)
Wind direction (10m)	Atmospheric pressure
Temperature and relative humidity (10m)	Evaporation
Anemometer (2m)	Precipitation

Temperature and relative humidity (2m)	Reflected short radiation
Temperature (0,5m)	Shortwavelength net radiation
Shortwavelength incident radiation	Diffuse radiation
Soil temperature (0,50m)	Long wavelength incident radiation
Soil thermal flux (0,05m)	Long wavelength reflected radiation
Soil thermal flux (0,10m)	Long wavelength net radiation
Soil thermal flux (0,20m)	Soil temperature (0,10m)
Soil thermal flux (0,30m)	Soil temperature (0,25m)
Soil moisture (0,30m)	Soil temperature (0,35m)
Soil moisture (0,60m)	

- Tiesas-lysimeter Station

Pluviometer
Temperature and Relative humidity (2m)
Temperature Sensor
Relative humidity Sensor
Piranometer (2m)
Radiometer neto (2m)
Anemometer (2m)
Reflectometer for hydric soil content
Evaporimetric bucket
CR10 Datalogger
Reference Lisimeter
Herbal Crop Lisimeter
Ligneous Crop Lisimeter

- Blancares-Station

Pluviometer	Moisture Sensor
Temperature and Relative Moisture (2m)	CR500 Datalogger
Temperature Sensor	

Available data acquired within SPARC-2004 campaign.

Measurements of meteorological parameters were done for Festuca, Vineyard and Barley crops. Soil temperature was registred each 15 minutes and lysimetric parameters were measured for each hour and day. All these data are available in the data base that will be described with detail at Part-III of the report.

8 - SURFACE ENERGY BUDGET MEASUREMENTS

Measurements of canopy fluxes and relevant variables in Barrax during 12-21 July 2004

Data used for modeling heat, water and CO_2 transfer inside and above canopy were collected by the Alterra Team (one of the EAGLE partners) over vineyard, bare soil, reforestation, sunflower, corn in Barrax during 12-21 July 2004. The team is a joint team by participants from Alterra, ITC and Utrecht University. The participants were Z. (Bob) Su (Alterra), Li Jia (Alterra), Jan Elbers (Alterra), Xiaomei Jin (Wageningen University), Ambro Gieske (ITC), Wim Timmermans (ITC), Hans van der Kwast (Utrecht University).

The measurements are grouped into the following categories in terms of their functions in radiative, heat, water and CO_2 fluxes modeling inside and above the canopy:

-Measurements of sensible, latent, and CO_2 fluxes together with radiation and soil fluxes will be useful to understand the characteristics of turbulent fluxes of different canopies, especially the sparse canopy, e.g. vineyard. Such data are also necessary for model validation.
-Measurements of gradients of air temperature and wind speed.
-Measurements of sunlit/shaded leaf/soil component temperatures are critical for understanding anisotropy of the thermodynamically heterogeneous canopy and will be used for validation of a radiative transfer model and a convective transfer model of a 3D-canopy.
-Measurements of photosynthesis, leaf conductance and transpiration are helpful for the validation of a complete model.
-Roughness length is a dynamic parameter determining the height of momentum transfer as well as the source height of heat transfer through the relation with roughness length for heat transfer.
-Leaf Area Index is a canopy structure parameter needed to model radiative transfer and heat transfer.

The summary of the measurements done by Alterra team is given in Table 8.1.

Table 8.1 Summary of measurements and instrumentation used by the Alterra Team from 12 to 21 July 2004 during the SPARC-2004/EAGLE campaign in Barrax, Spain.

Measurements	**Instrumentation**	**Observer**
Turbulence, H2O, CO2 fluxes and CO2 concentrations	Eddy correlation system: - Gill 3D sonic - closed path Licor gasanalyser: CO2 and H2O/nitrogen reference gas - pneumatic mast - dataloggers	Alterra
Gradient of air temperature and humidity	Thermocouple	Alterra
Sunlit/shaded leaf/soil temperatures	Thermocouple	Alterra
Soil heat flux		Alterra / ITC
Soil temperatures	Thermocouple wires	Alterra
Radiation balance components: Short-wave and long-wave incoming and outgoing radiation, wind, air temperature, and sensible heat flux	Scintillometer system	ITC
Radiometric surface temperature	Radiometer	ITC
Photosynthesis, conductance and transpiration	CIRAS	Alterra
Radiometric surface temperature measurements using a hand-held radiometer	Reytek hand-held radiometer	Alterra
Roughness length	stereo photogrammetry with the NEar Sensing CAmera Field Equipment (NESCAFE)	UU
Emissivity	'two-lid' box	UU
LAI	hemispherical photographs	UU

Description of measurements

8.1 Turbulent heat fluxes and radiation fluxes

The surface flux data set is comprised of data obtained by the eddy correlation system and the scintillation technique.

8.1.1 Sensible, latent and CO2 fluxes measurements using eddy correlation system

A three-dimensional eddy correlation system was set up in the vineyard field to observe the turbulent exchange of sensible, latent heat and CO2 fluxes above the canopy by measuring the co-variance of the vertical wind velocity with respectively the air temperature, the water vapor density and CO2 density. The system consists of a 3D sonic anemometer, a closed path Licor gas-analyser, a nitrogen reference gas supply, a pneumatic mast and dataloggers.

The flux observations are 10 minutes and 60 minutes averages. The height of measurements is 2.4m above the ground corresponding to eddy fluxes to an upwind surface "footprint" which is spread over a range between 10 to over 100 times the height of the sensors. Such setup ensures only fluxes from vineyard canopy were observed by the eddy correlation system. Figure 8.1 gives an example of 60 minutes averages of sensible and latent heat fluxes measured by the eddy correlation system over vineyard canopy.

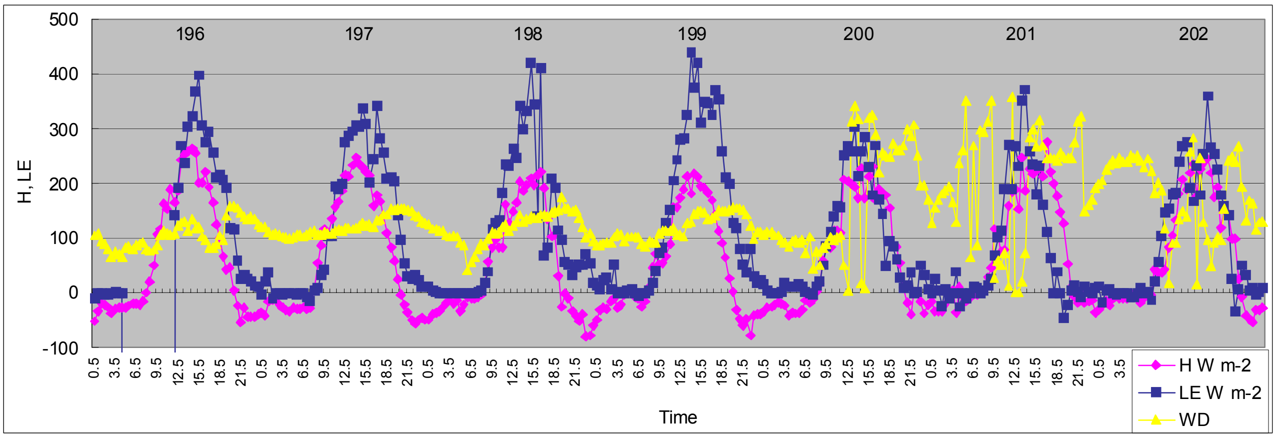

Figure 8.1 Sensible and latent heat fluxes measured by eddy correlation system over vineyard canopy during DOY 196 to DOY 202 2004 in Barrax (H: sensible heat flux, LE: latent heat flux, WD: wind direction).

8.1.2 Sensible heat flux measurements using Scintillation method

Many studies have demonstrated that the scintillation technique is a reliable and suitable method. When electromagnetic (EM) radiation propagates through the atmosphere it is distorted by a number of processes that can influence its characteristics, e.g. its intensity or amplitude (by far the most important), polarization and phase. The most serious mechanism that influences the propagation of EM radiation is small fluctuations in the refractive index of air (n). These turbulent refractive index fluctuations in the atmosphere lead to intensity fluctuations and are known as scintillations. Some examples that clearly show the distortion of wave propagation by the turbulent atmosphere that can be seen regularly by the human eye are the twinkling of stars, image dancing and image blurring above a hot surface. In most cases the atmosphere is turbulent. Turbulence is described as three-dimensional air motions (known as eddies), which have sizes ranging between millimetres to tens of metres. Turbulence in the atmosphere is the most effective transport mechanism for many scalar quantities, such as sensible heat (H) and water vapour (LE). As these eddies transport both heat and water vapour their refractive indices are different from their surroundings, resulting in refractive index fluctuations and thus scintillations, which are measurable (De Bruin et al., 1995).

Measurement principle

A scintillometer is an instrument, consisting of a transmitter and a receiver, which can measure the "amount" of scintillations by emitting a beam of light over a horizontal path. The scintillations "seen" by a scintillometer can be expressed as the structure parameter of the refractive index of air. The structure parameter correlates with the "turbulent strength" of the atmosphere, which describes the ability of the atmosphere of transporting e.g. sensible heat and water vapor.
Because the scintillometer integrates over its optical path the structure parameter is actually a path-averaged value. Path-averaging is the most important advantage of the scintillation method compared to traditional (point) measurement techniques, and a such has a direct link with area averaged turbulent flux estimates from satellite or airborne remote sensing measurements. A mobile scintillometer was used to make measurements over corn on DOY 198, reforestation on DOY 199, sunflower on DOY 200, and bare soil on DOY 201 respectively. Figure 8.2 gives the example of sensible heat flux measurements by scintillometer over vineyard canopy.

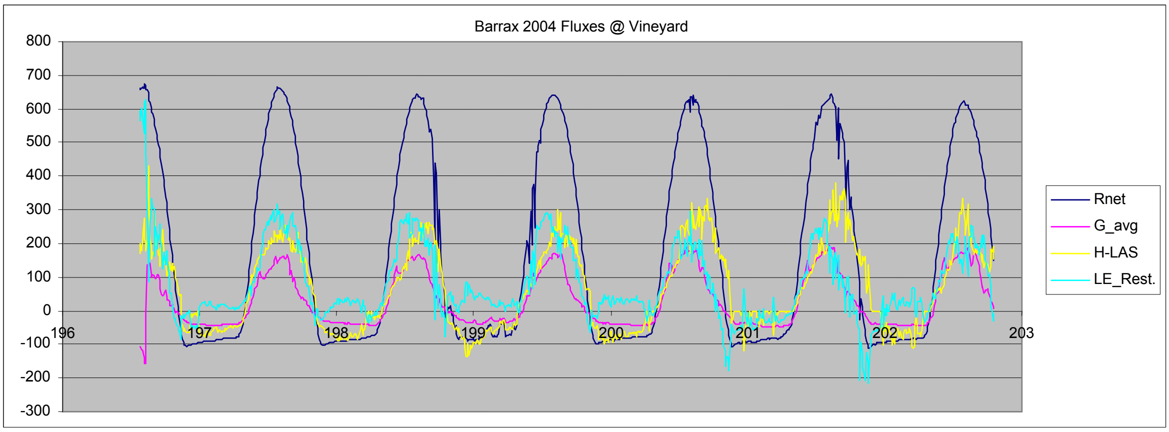

Figure 8.2 Sensible heat flux measured by eddy correlation system over vineyard canopy during DOY 197 to DOY 203 2004 in Barrax (Rnet: net radiation flux, G_avg: soil heat flux, H-LAS: sensible heat flex, LE_rest: latent heat flux as the residual of energy balance equation).

8.2 Measurements of sunlit/shaded leaf/soil component temperatures

Measurements of sunlit/shaded leaf/soil component temperatures are critical for understanding anisotropy of the thermodynamically heterogeneous canopy and will be used for validation of radiative transfer model and convective transfer model of a 3D-canopy. Measurements were made using thermocouples sticking to the leaf surface or buried just underneath the soil surface (ca. 1cm the soil). A Reytek hand-held thermal infrared radiometer was also used to measure the four component temperatures by randomly sampling in the vineyard. Figure 8.3 shows the measurements of component temperatures made by the Reytek hand-held thermal infrared radiometer on three different days.

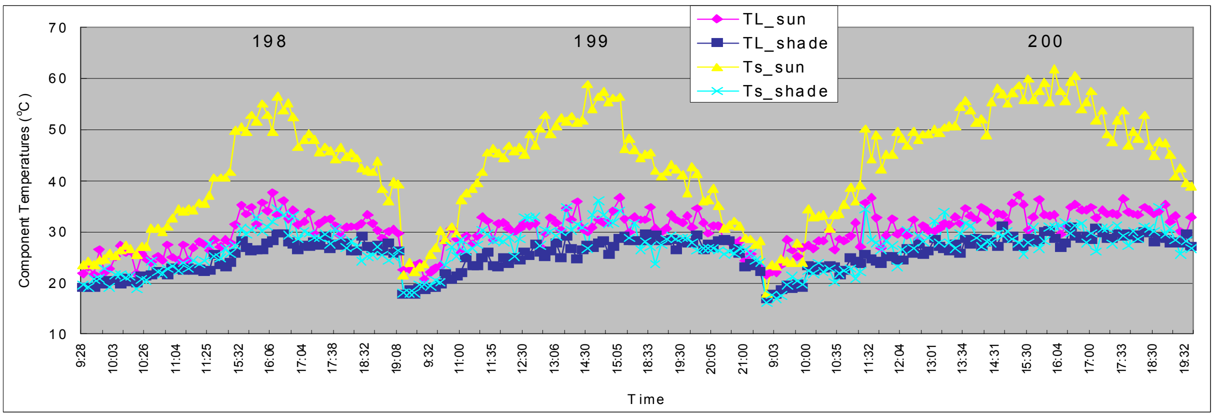

Figure 8.3 Sunlit/shaded soil/foliage component temperatures measured by Reytek hand-held radiometer during DOY 198, 199 and 200 in 2004 in vineyard site of Barrax. (TL_sun: sunlit leaf, TL_shade: shaded leaf, Ts_sun: sunlit soil, Ts_shade: shaded soil).

8.3 Gradient of air temperature and humidity

Measurements of air temperature and humidity gradient (Figure 8.4) were made in the vineyard field and will be used for evaluating the multi-source model and algorithm of roughness length for heat transfer.

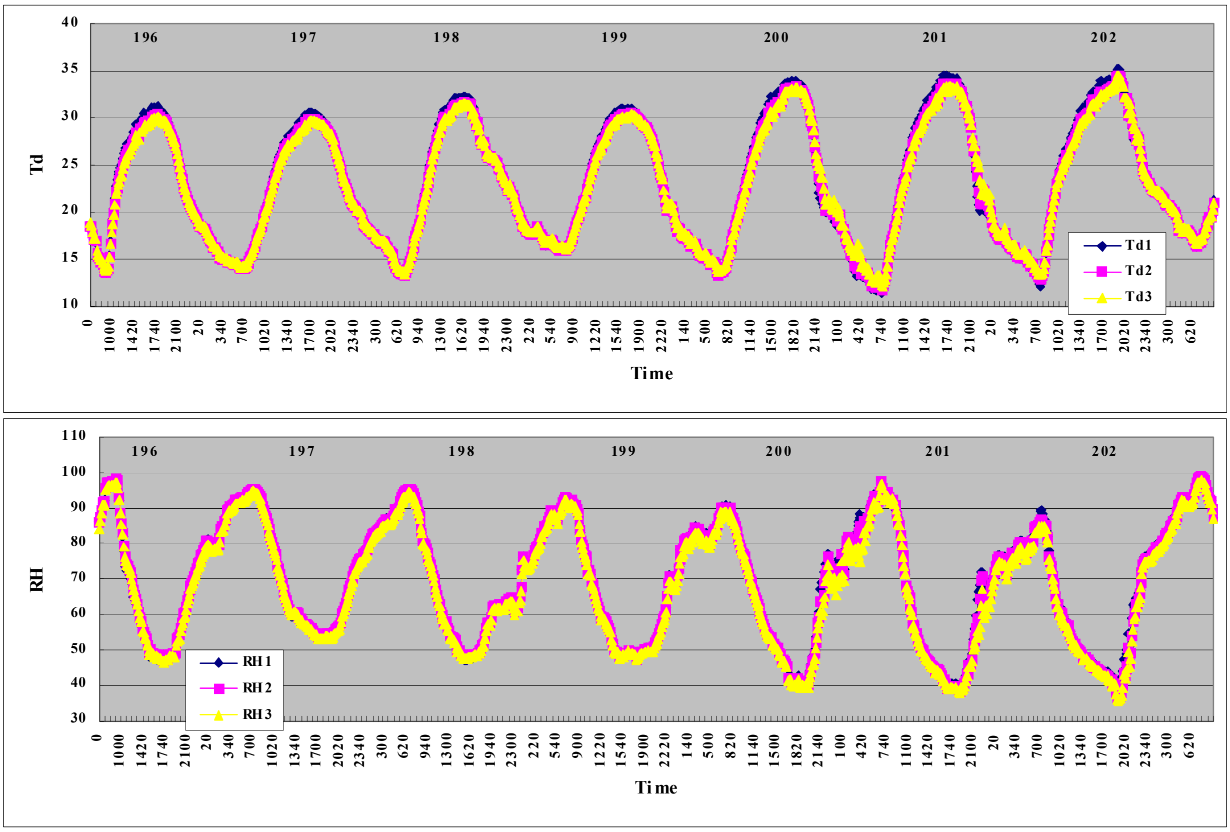

Figure 8.4 Gradients of air temperature and humidity

8.4 Measurements of photosynthesis, conductance and transpiration

A CIRAS (Differential CO2/H2O Infrared Gas Analyzer) was used to measure photosynthesis, conductance and transpiration at single leaf level of grape plants during 17, 18 and 19 July 2004 in the vineyard site. Each cycle of measurement took roughly 20 minutes with five 'old' and five 'young' leaves measured. The leaves were selected randomly near the position where a Lysimeter system was located. The plant leaf is clamped into the leaf cuvette and the CO2 gas and water vapor are measured before entering the cuvette and on exit providing measurements of leaf temperature, PAR (Photosynthetically Active Radiation), leaf stomatal conductance, leaf photosynthesis rate, respiration rate and leaf transpiration.

8.5 Roughness

Roughness length was measured by means of Near Sensing Camera Field Equipment (NESCAFE). NESCAFE has a close range remote sensing technique for measurement of surface geometric roughness, i.e. the DEMs of a area ca. 10 x 10 m, with pixels of ca. 2 cm using a DGPS. Roughness measurements were made over vineyard and bare soil.

8.6 Emissivity

An aluminum box with a dimension of 30cm (wide) x 30cm (length) x 80cm (height) was used to make measurements of emissivity by means of a two-lid method over several different canopies, i.e. bare soil, alfalfa, sunflowers and stubble. A Raytek ST60 infrared thermometer was used to measure temperatures when cold-lid and hot-lid were covered respectively (Rubio et al., 2003).

Summary

Some of the data, e.g. heat fluxes, gradient of air temperature and humidity and component temperatures, have been processed to the ESA-CDB format and will be uploaded to the website soon. Other data are still in processing from raw format to the CDB format.

Besides the data collected in the field, satellite data have also been colleted by ITC, these data are:

- ASTER images

- A full set of MSG-1 global images for 2 weeks covering the SPARC 2004 campaign period.

PART II- Data Processing

9- PRE-PROCESSING OF CHRIS/PROBA DATA ACQUIRED DURING SPARC 2003 AND 2004 CAMPAIGNS

A considerable effort has been made at the Laboratory for Earth Observation in the pre-processing of the CHRIS/PROBA data acquired in the SPARC 2003 and 2004 campaigns. Geometric correction, noise removal and atmospheric correction has been performed on the acquired images to make them available for the later exploitation of the data. Geometric correction and noise removal will be described in a future report, while some first results of the atmospheric correction will be shown briefly here.

The main effort has been put on the implementation of an operative atmospheric correction algorithm over land which estimates the aerosol and water vapour contents as a prior step to the derivation of the surface reflectance. The fundamental basis lies on the retrieval of the aerosol optical thickness (AOT) and the water vapour column content from the image itself, by means of the inversion of the Top-Of-Atmosphere (TOA) radiances from 5 pixels with a large spectral contrast, in order to decouple the atmosphere and the surface contributions in the measured signal. Due to the reported mis-calibration of the instrument in the near-infrared bands, a final step devoted to the recalibration of the calculated reflectances is performed, being the corresponding updated calibration curve obtained as a by-product of the atmospheric correction procedure.

Four CHRIS/PROBA data sets over the Barrax area are available (acquired in mode-1, 62 bands and 34 m spatial resolution), two for each year. For the SPARC 2003 campaign, acquisitions were made on 12th and 14th July. The situation over Barrax on those days was particularly favourable, because PROBA almost passed over (-4º across-track zenith angle) on 13th July, and then on 12th July (+20º across-track zenith angle) and on 14th July (-27º across-track zenith angle). Unfortunately, the image from 13th July was not correctly taken because of satellite pointing problems, so we have had only two images from the campaign. Concerning SPARC 2004, two data sets were also acquired, on 15th and 16th July. Nevertheless, the system failed on the first date, and only 3 of the 5 images for 15th July were recorded, one of them only partially. The observation angles for each of the two days and the two years are plotted in Figure 9.1.

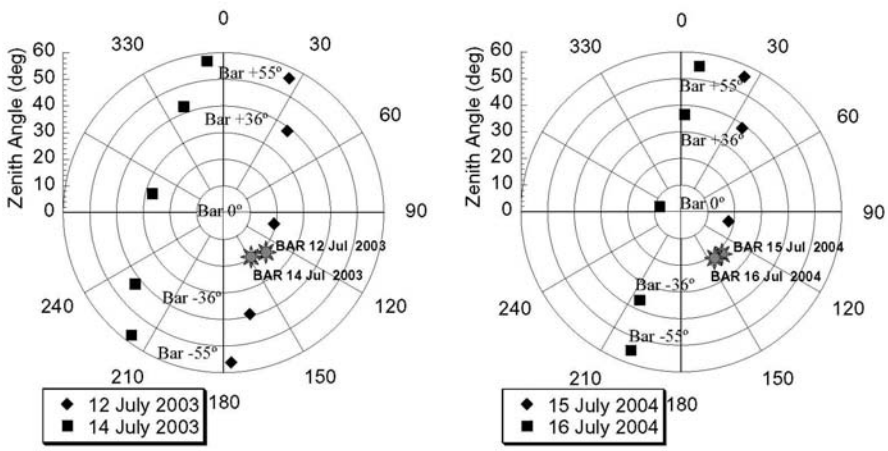

Figure 9.1. Acquisition geometries and illumination angles for the images of SPARC 2003 and 2004.

Despite the failures in some of the acquisitions, the resulting data base, with 4 different dates, turned out to be enough for the validation exercise, as well as to show the capabilities of the CHRIS/PROBA data to represent the particular spectral and angular features of different targets. The results obtained from the application of the algorithm to those images and the validation with in-situ measurements will be discussed next.

A sample of surface reflectance spectra from the Barrax site is displayed in Figure 9.2. They have been manually extracted from the same targets in the 5-angle images. In-situ measurements taken with an Analytical Spectral Devices (ASD) FieldSpect Pro FR Spectroradiometer are also plotted for the alfalfa and bare soil surfaces. The agreement between the ASD spectroradiometer and the CHRIS data is quite high, both in the shape and in the reflectance levels, what validates the techniques used in the pre-processing of the data. It must be taken into account that the field spectra were acquired from a nadir view, not coincident with any of the CHRIS/PROBA view angles, so small deviations due to angular differences are expected a priori. This is confirmed by the fact that the maximum agreement with the in-situ measurements is found for the “0” Fly-by Zenith Angle (FZA), which is the closest one to the vertical view used in the field measurement.

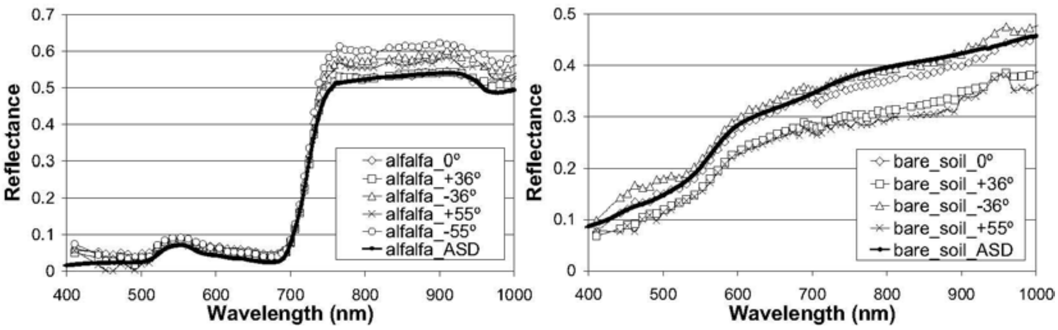

Figure 9.2. Sample surface reflectance spectra extracted from the 5 observation angles of Barrax 16 July 2004 images. Angles in the legends correspond to the view zenith and azimuth angles plotted in Figure 9.1. Ground-truth from in-situ measurements is also plotted for alfalfa and bare soil targets (black thick line).

Apart from this qualitative comparison of the directional effects in the surface reflectance for different targets, further validation of the angular trends showed by the alfalfa crop has been achieved using a newer coupled version of the SAIL and PROSPECT models. We have only selected the alfalfa crop for its 2D uniformity, which makes it the prototype of crop to be modelled with the SAIL/PROSPECT model. Besides, all the inputs needed (chlorophyll content, LAI, water content and dry matter content) were explicitly measured during the SPARC 2004 campaign. Results for the 5 angles in Fig.1 are plotted in Fig.3. It can be stated that both the spectral shape (Figure 9.3-a) and the angular dependencies (Figure 9.3-b) are highly coincident with those showed for the alfalfa crop in Figure 9.2, what confirms the validity of the procedure applied in the pre-processing of the CHRIS/PROBA data.

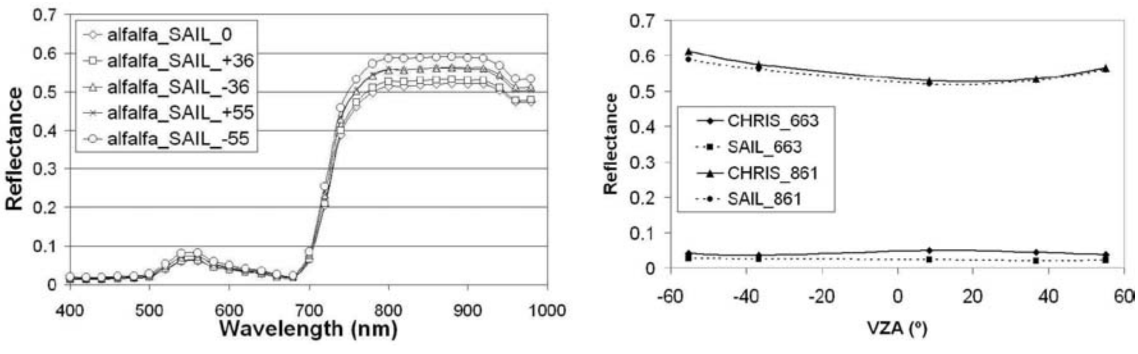

Figure 9.3. Left (a), results of SAIL/PROSPECT simulations using in-situ measurements of the biological parameters for the alfalfa crop and the geometrical configuration plotted in Figure 9.1. Right (b), projection of the alfalfa simulations in Figure 9.3-a on the view zenith angle, for 2 wavelengths in the red (663 nm) and in the NIR (861 nm) regions.

As a summary of the pre-processing, the images acquired from the FZA=0º in the two dates of the 2004 campaign are displayed in Figure 9.4, after the geometric correction, the noise removal and the atmospheric correction. The failure in the acquisition of around a third of the 15th July image can be noted, although most of the crops located in the measurements area are visible fortunately.

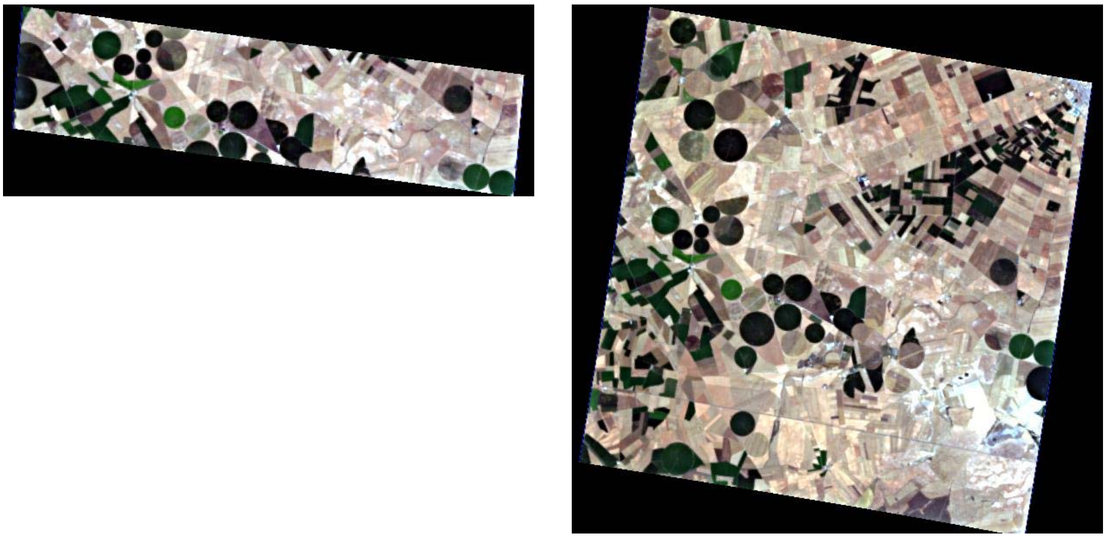

Figure 9.4. Left (a), 15th July 2004 Barrax image acquired from the FZA=0º, after all the pre-processing steps. Right (b), same for 16th July.

10- GROUND DATA PROCESSING&PRODUCTION OF THE LEVEL 1 HIGH RESOLUTION MAPS

This chapter describes the production of the high resolution, level 1, biophysical variable maps for the Barrax site in 2003 (see campaign report for more details about the site and the ground measurement campaign). Level 1 map corresponds to the map derived from the determination of a transfer function between reflectance values of the SPOT image acquired during (or around) the ground campaign, and biophysical variable measurements (Hemispherical Images). For each Elementary Sampling Unit (ESU), the hemispherical images were processed using the CAN-EYE software (Version 1.3) developed at INRA-CSE.

The derived biophysical variable maps are:

- Leaf Area Index: two LAI are considered, the first one corresponds to effective LAI derived from the description of the gap fraction as a function of the view zenith angle, the second one (LAI57) is derived from the gap fraction at 57.5°, which is independent on the leaf inclination and is also an effective LAI (does not take into account clumping effect).
- cover fraction (fCover) : it is the percentage of soil covered by vegetation between o° et 10° view zenith angle
- fAPAR: it is the fraction of Absorbed Photosynthetically Active Radiation (PAR=400-700nm). The fAPAR can be defined as instantaneous (for a given solar position) or integrated all over the day. Following a study based on radiative transfer model simulations, it has been shown that the root mean square error between instantaneous fAPAR computed every 30 mns and the daily fAPAR is the lowest for instantaneous fAPAR at 10h00 AM (local time, RMSE= 0.021). Therefore, the derivation of fAPAR from CAN-EYE corresponds to the instantaneous black sky fAPAR at 10h00 AM.

10.1 Available data

10.1.1. Sampling strategy

Figure 10.1 shows that the ESUs locations are well spatially distributed over the 5km x 3km site. The site has been extended to a 5kmx5km area in order to add bare soil points (Beatriz Martinez, personal communication) which are at the top and bottom limits of the image (ESUs 56,57,58).
The processing of the ground data has shown that:

- ESUs E32, E40, E26 (in black on Figure 10.1) were located on field borders. Those three ESUs were eliminated
- Considering that SPOT geo-location and GPS measurements are associated to errors, we found that processed LAI for ESUs E8, E11, E17, E34 and E38 did not correspond to the SPOT pixel in terms of reflectance: they have been shifted of 1 pixel, according to D. Béal and F. Baret who participated to the measurements.

Finally 48 ESUs have been kept for the computation of the transfer function.

The sampling strategy is evaluated using the SPOT image by comparing the NDVI distribution over the site with the NDVI distribution over the ESUs (Figure 10.2). As the number of pixels is drastically different for the ESU and whole site (WS=22500 in case of a 3x3km SPOT image), it is not statistically consistent to directly compare the two NDVI histograms. Therefore, the proposed technique consists in comparing the NDVI cumulative frequency of the two distributions by a Monte-Carlo procedure which aims at comparing the actual frequency to randomly shifted sampling patterns. It consists in,

1. Computing the cumulative frequency of the N pixel NDVI that correspond to the exact ESU locations.
2. Then, applying a unique random translation to the sampling design (modulo the size of the image).
3. Computing the cumulative frequency of NDVI on the randomly shifted sampling design
4. Repeating steps 2 and 3, 199 times with 199 different random translation vectors.

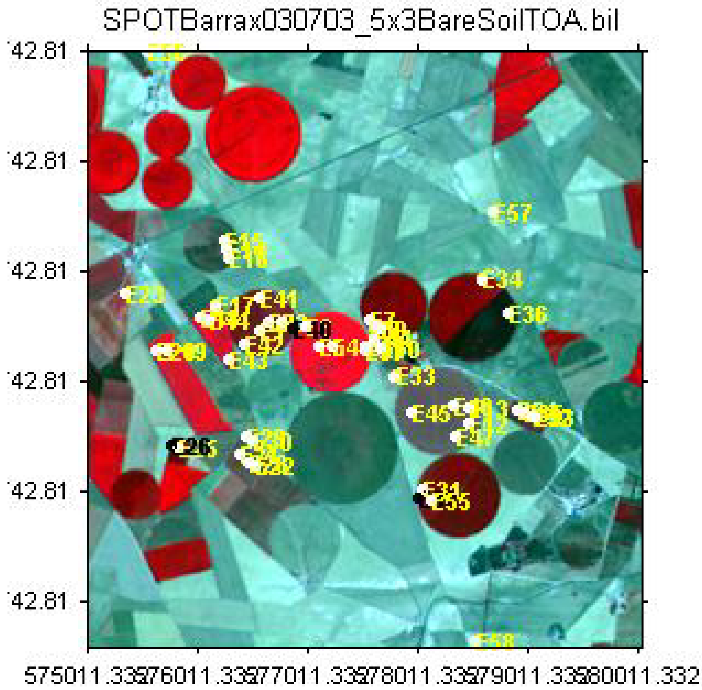

Figure 10.1. Distribution of the ESUs around the Barrax site. ESUs in black were eliminated for the computation of the transfer function

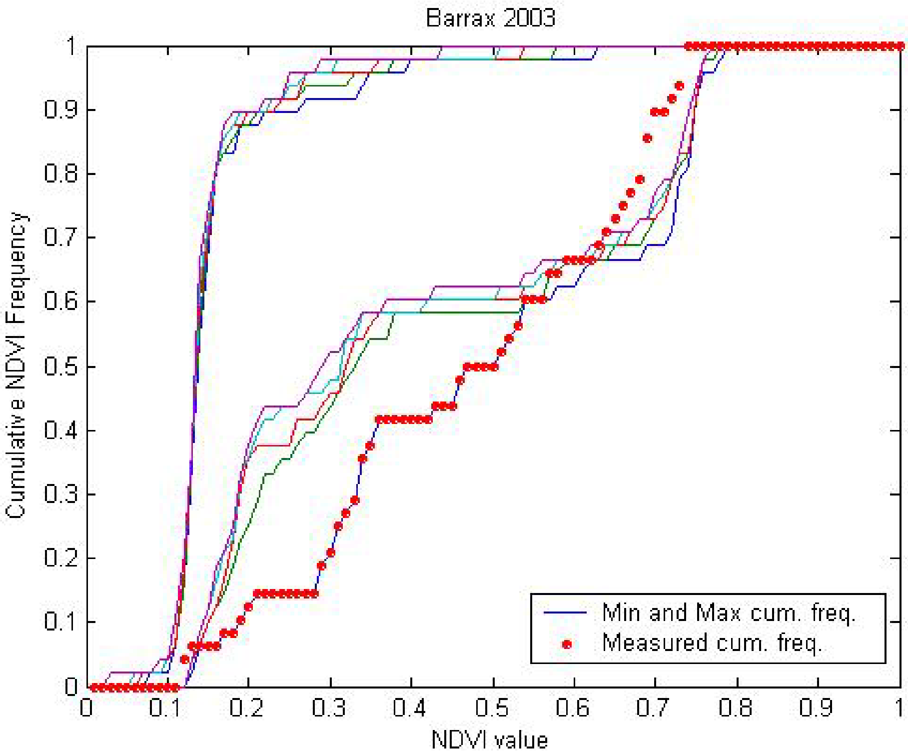

Figure 10.2. Comparison of the ESU NDVI distribution and the NDVI distribution over the whole image.

This provides a total population of N=199+1(actual) cumulative frequency on which a statistical test at acceptance probability $1-\alpha=95\%$ is applied: for a given NDVI level, if the actual ESU density function is between two limits defined by the $N\alpha/2=5$ highest and lowest values of the 200 cumulative frequencies, the hypothesis assuming that WS and ESU NDVI distributions are equivalent is accepted, otherwise it is rejected.

Figure 10.2 shows that the NDVI distribution of the 48 ESUs is not well representing the NDVI distribution on the 5kmx5km image. As a lot of bare soils area are observed on this site, and only 3 bare soil points are considered, low NDVI values are not well sampled. Therefore, as we consider cumulative frequency, the 'ESU' curve is outside the 'boundary curves', mainly because of the mis-representation of bare soils. However, the effect of the ESU NDVI distribution should be slight since bare soil points are taken into account in the regression. This can be checked by looking at the LAI map which should show very low LAI values for bare soil areas observed on the SPOT image.

10.1.2 SPOT image

The SPOT image was acquired the 3rd july 2003 by HRVIR2 on SPOT4. It was geo-located by SPOTimage (SPOTView basic). The projection is UTM 30N, WGS84, no atmospheric correction was applied to the image since no atmospheric data were available. However, as the SPOT image is used to compute empirical relationships between reflectance and biophysical variable, we can assume that the effect of the atmosphere is the same over the whole 5kmx3km site. Therefore, it will be taken into account everywhere in the same way. **Figure 10.3** shows the relationship between RED and near infrared (NIR) SPOT channels: the soil line is well marked, and no saturated points are observed.

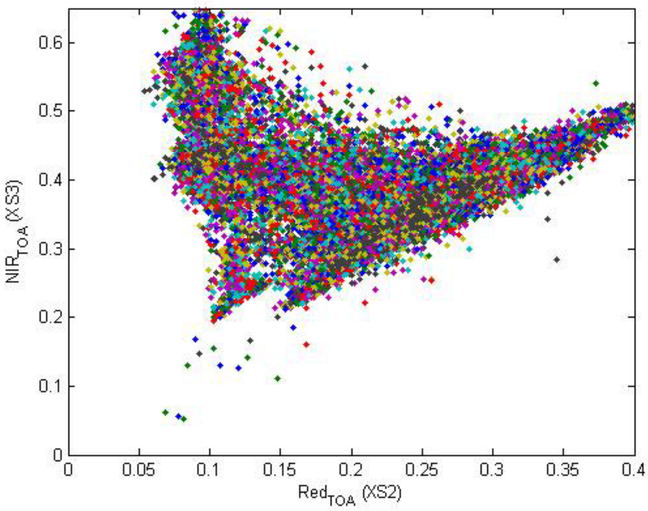

Figure 10.3. Red/NIR relationship on the SPOT image for Barrax, 2003.

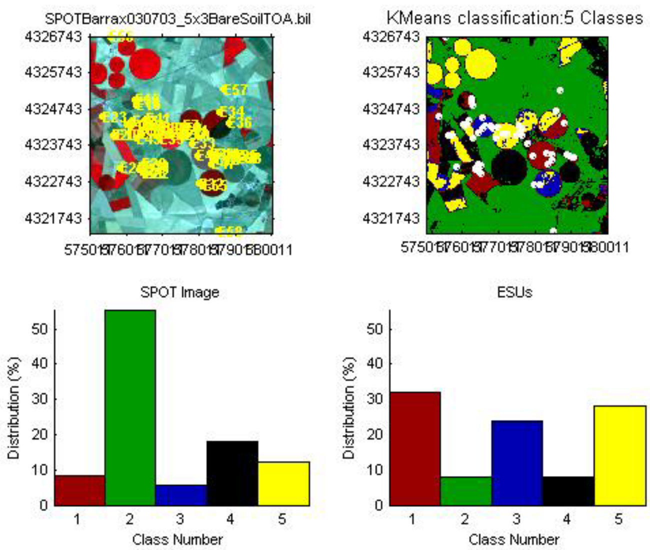

Figure 10.4. Classification of the SPOT image. Comparison of the class distribution between the SPOT image and sampled ESUs.

A non supervised classification based on the k_means method (matlab statistics toolbox) was applied to the NDVI of the SPOT image to distinguish if different behaviours on the image for the biophysical variable-reflectance relationship exist. A number of 5 classes were chosen (Figure 10.4). The repartitions of the classes on the image and on the ESUs are quite different, since bare soils (class 2) are not sampled enough.

10.1.3 Hemispherical images

The hemispherical images were processed by the CAN-EYE software (Version 1.3) to derive the biophysical variables. Figure 10.5 shows the distribution of the different measured variables over the sampled ESUs. Green LAI derived from directional gap fraction and LAI derived from gap fraction at 57.5° are consistent and varies from 0 to 6 (alfalfa fields).
Figure 10.6 shows the different relationships observed between the biophysical variables and corresponding NDVI or the ESUs, as a function of the SPOT classes determined in §10.1.2. No different behaviours between the classes can be observed. However, Figure 10.4 shows that the bare soil class is under-represented in the ESU sampling. Therefore, for this class, for which we know that LAI is null, we use the one transfer function,, using a mean value of 0 and determine a single transfer function for all the other classes.

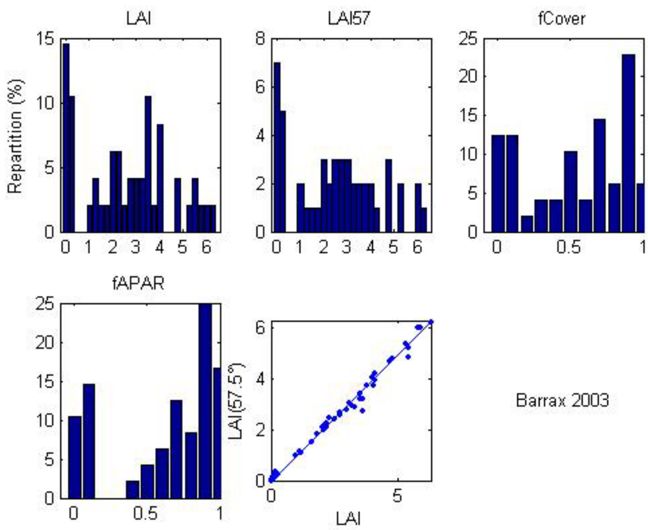

Figure 10.5. Distribution of the measured biophysical variables over the ESUs.

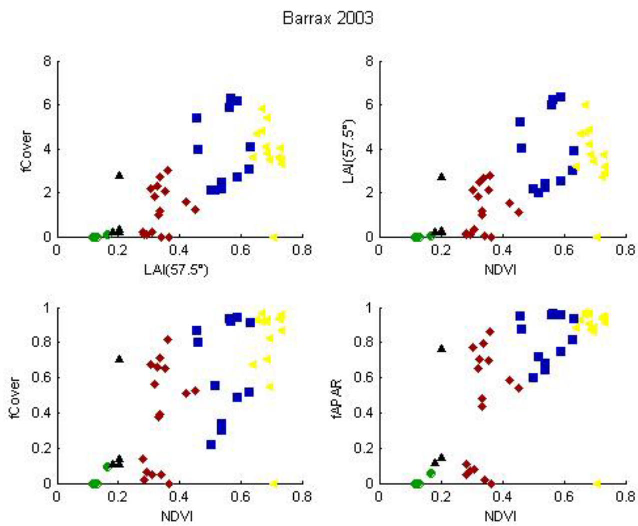

Figure 10.6. NDVI-Biophysical Variable relationships as a function of SPOT classes

10.2 Determination of the transfer function for the 4 biophysical variables

10.2.1 Tested Transfer functions

For each class determined in §10.1.2, three types of transfer functions are tested:

- AVE: If the number of ESUs belonging to the class is too low, the transfer function consists only in attributing the average value of the biophysical variable measured on the class to each pixel of the SPOT image belonging to the class.

- REG: If the number of ESUs is sufficient, multiple robust regression between ESUs reflectance (or Single Ratio) and the considered biophysical variable can be considered: we used the 'robustfit' function from the matlab statistics toolbox. It uses an iteratively re-weighted least squares algorithm, with the weights calculated at any iteration by applying the bisquare function to the residuals from the previous iteration. This algorithm gives lower weight to ESUs that do not fit well. The results are less sensitive to outliers in the data as compared with ordinary least squares regression. At the end of the processing, three errors are computed: classical root mean square error (RMSE), weighted RMSE (using the weights attributed to each ESU) and cross-validation RMSE (leave-one-out method).

- LUT: If the number of ESUs is sufficient, Look-Up-Tables are also enviewed : a look-up table is build using ESUs reflectances and corresponding measured biophysical variable. For a given pixel, a cost function is computed as the sum square difference between the pixel reflectances and the ESU reflectances over the 4 bands, divided by the standard deviation computed on ESU reflectances. The result of the cost function is sorted in ascending order, and the biophysical variable estimated for the given pixel is computed as the mean value of the first n ESUs providing the lowest value of the cost function. Different values of n are considered to get the lowest cost function. This method is reliable only if the ESU NDVI distribution is quite comparable with the whole site NDVI distribution. In §10.1.1, 10.1.2it has been shown that the two distribution are quite different because of the presence of bare soil areas. Therefore, the results of this method will be shown for Barrax site but will not be applied to derive the biophysical variable maps.

Both regression and Look-Up-Tables are tested using either the reflectance or the logarithm of the reflectance for any band combination, plus the simple ratio. As both methods have poor extrapolation capacities, a flag image, based on the computation of convex hull over reflectances, is computed showing:

- Pixels belonging to the class for which AVE method was applied
- Pixels inside the 'strict convex-hull': for each class (not AVE method), a convex-hull is computed using all the reflectance combination used for the transfer function, and corresponding to the ESUs belonging to the class. For those pixels, the transfer function is used as an interpolator, and the degree of confidence in the results obtained is quite high.
- Pixels inside the 'large convex-hull': for each class (not AVE method), a convex-hull is computed using all the reflectance combination (±5% in relative value) used for the transfer function, and corresponding to the ESUs belonging to the class. For those pixels, the transfer function is used as an extrapolator (but not far from interpolator), and the degree of confidence in the results obtained is quite good.
- Pixels outside the two convex-hulls: this means that for these pixels, the transfer function acted like an extrapolator which makes the results less reliable. However, having *a priori* information on the site may help to evaluate the extrapolation capacities of the transfer function.

10.2.2 Results on the Barrax site

Figure 10.4 shows that the bare soil class is under-represented in the ESU sampling. Therefore, for this class, for which we know that LAI is null, we use the AVE method, using a mean value of 0. For the other classes (1,2,4,5 = 44 ESUs), we have tested REG and LUT methods using all the classes together to keep a reasonable number of data for the regression.

10.2.1.1 Choice of the method for classes (1,2,4,5)

Figure 10.7 and Figure 10.8 show the results obtained for all the possible band combinations using either the reflectance or the logarithm of the reflectance:

- As, the NDVI distribution of the ESUs (Figure 10.2) does not well represent the whole site, which could represent a risk for establishing the map since the LUT method works only for interpolation purposes. Moreover, the REG method provides similar and even better results for all the variables and is therefore selected as the transfer function.
- Using either the logarithm of the reflectance or the reflectance itself provides very similar results in terms of cross-validation RMSE. However, the number of points with a weight lowers than 0.7 in the robust regression is higher when using the logarithm of the reflectance. Therefore we choose to use the robust multiple regression using the ESUs reflectance value.

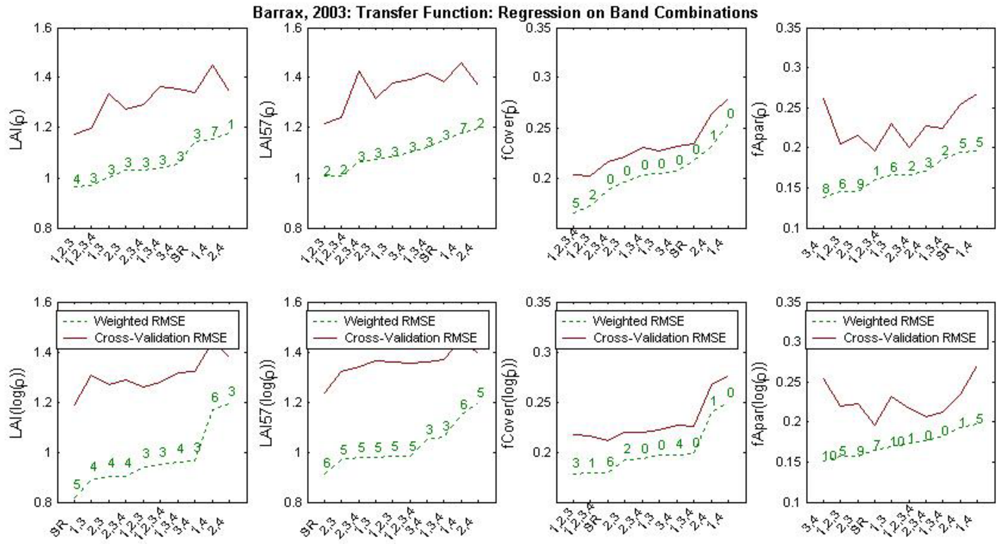

Figure 10.7. Transfer function: test of multiple regressions applied on different band combinations. Band combinations are given in abscissa. The estimated biophysical variable is given in ordinate. Top graphs correspond to regression made on reflectance (ρ): the weighted root mean square error (RMSE) is presented in green along with the cross-validation RMSE in red. The numbers indicate the number of data used for the robust regression with a weight lower than 0.7. Bottom graphs correspond to regression made on the logarithm of the reflectance.

10.2.1.2 Choice of the band combination for classes (1,2,4,5)

For the effective LAI and LAI at 57.5°, Figure 10.9 and Figure 10.12 show that some ESUs have systematically a weight lower than 0.7 for all tested band combination: E41 and E42 (LAI and LAI57) correspond to dense alfalfa fields and E52 to grassland. For these canopies, hemispherical photographs are taken from above and the pixels corresponding to bare soil on the images may not be easy to be identified during the classification process of the CAN-EYE Software. Indeed, when comparing the processing of two different users (B. Martinez, university of Valencia, Spain and F. Baret, INRA-CSE, France) on the ESUs, the results are quite different (Figure 10.10). Note that the RMSE value is quite high (around 1).

The (XS1,XS2,XS3,XS4) combination for LAI and (XS1,XS2,XS3) for LAI at 57.5° were selected since it presents a good compromise between the RMSE values and the number of points with a weight lower than 0.7 (Figure 10.11).

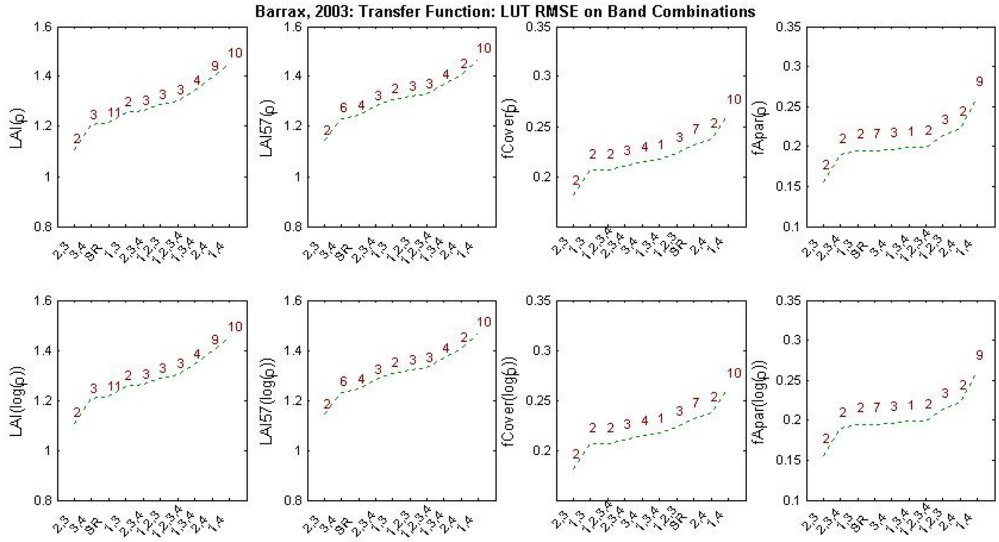

Figure 10.8. Transfer function: test of LUT applied on different band combinations. Band combinations are given in abscissa. The estimated biophysical variable is given in ordinate. Top graphs correspond to regression made on reflectance (ρ): the root mean square error is presented in green. The numbers indicate the number of elements selected in the LUT to compute the resulting biophysical variables. Bottom graphs correspond to LUT using the logarithm of the reflectance.

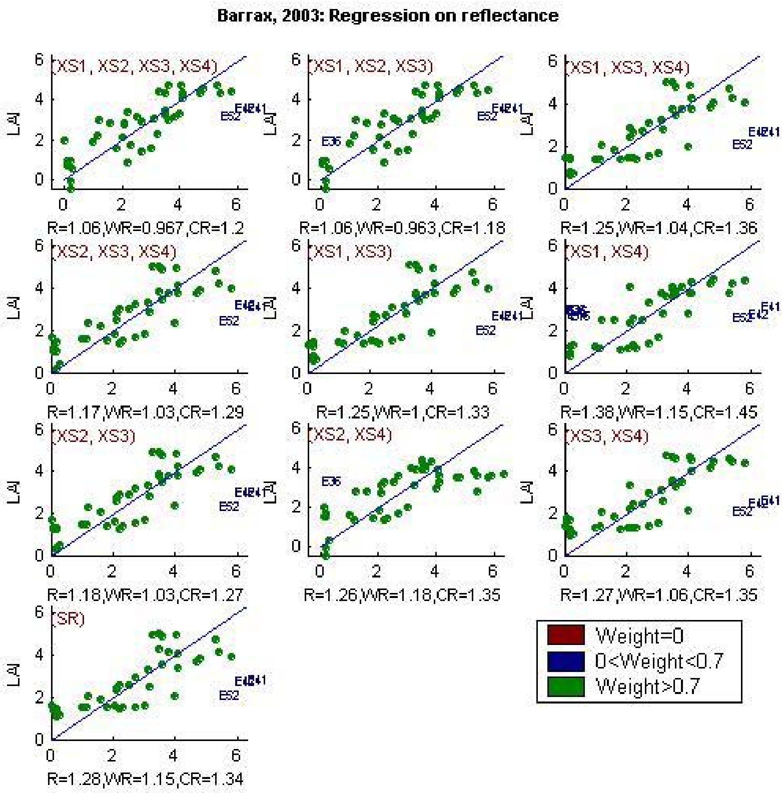

Figure 10.9. Effective Leaf Area Index: results for regression using different band combinations. R is the root mean square error computed between LAI and estimated LAI. WR is the weighted root mean square error and CR is the cross validation root mean square error.

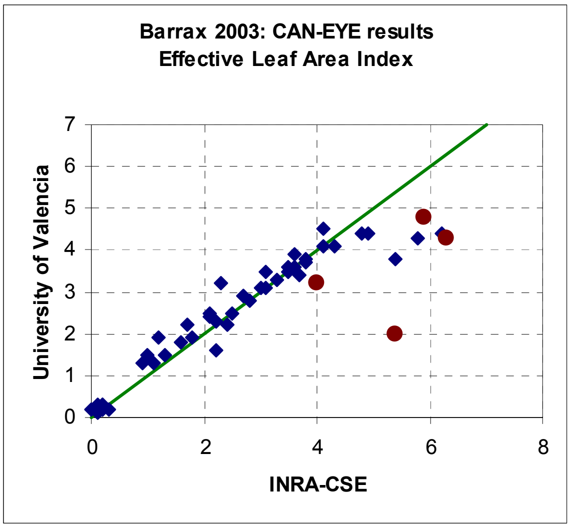

Figure 10.10. Comparison of CAN-EYE processing results from two different users. Points in red correspond to ESUs which have systematically a weight lower than 0.7 regarding the tested band combination.

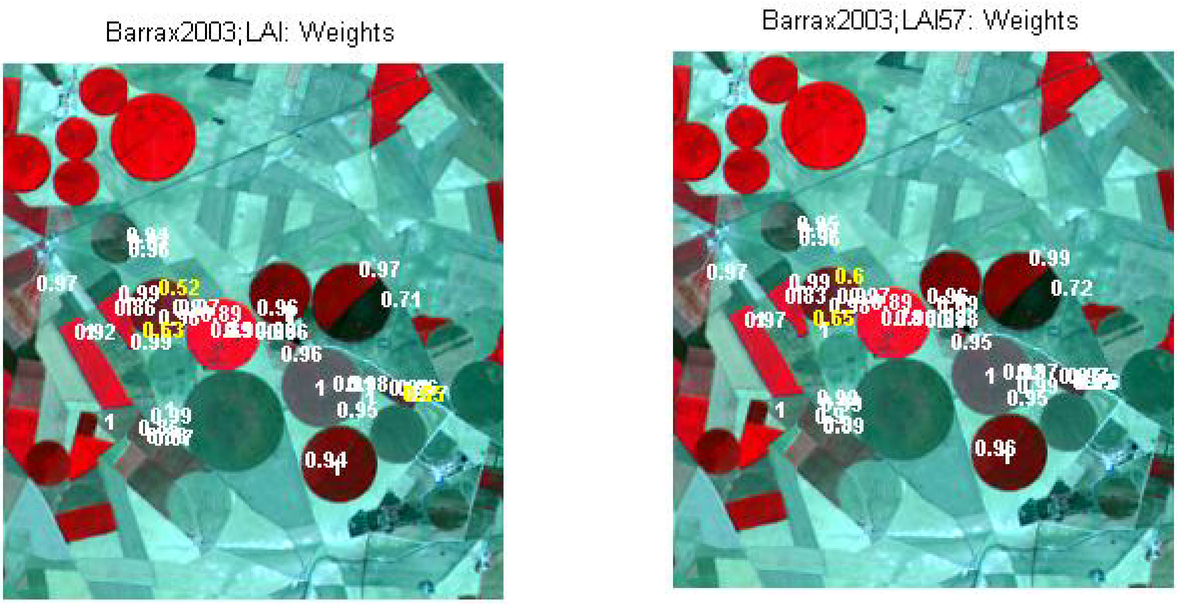

Figure 10.11. Weights associated to each ESU for the determination of LAI (left) and LAI57 (right) transfer function.

For fCover (XS2, XS3, XS4), and fAPAR (XS1, XS2, XS3, XS4), compromise has to be made between RMSE values and the number of ESUs with weight lower than 0.7. Note that the ESUs causing problems for LAI are not the same for fCover and fAPAR. ESUs 21 and 22 correspond also to dense canopies (alfalfa and sugar beet) and the result may depend on the CAN-EYE processing. For fAPAR, ESU 14, 15, 16 and 36 correspond to fields which are mostly in the senescent phase; therefore the corresponding reflectance may be disturbed by the senescent vegetation. Moreover, during the classification phase in the CAN-EYE processing it may be sometimes difficult to make a separation between green parts and yellow ones.

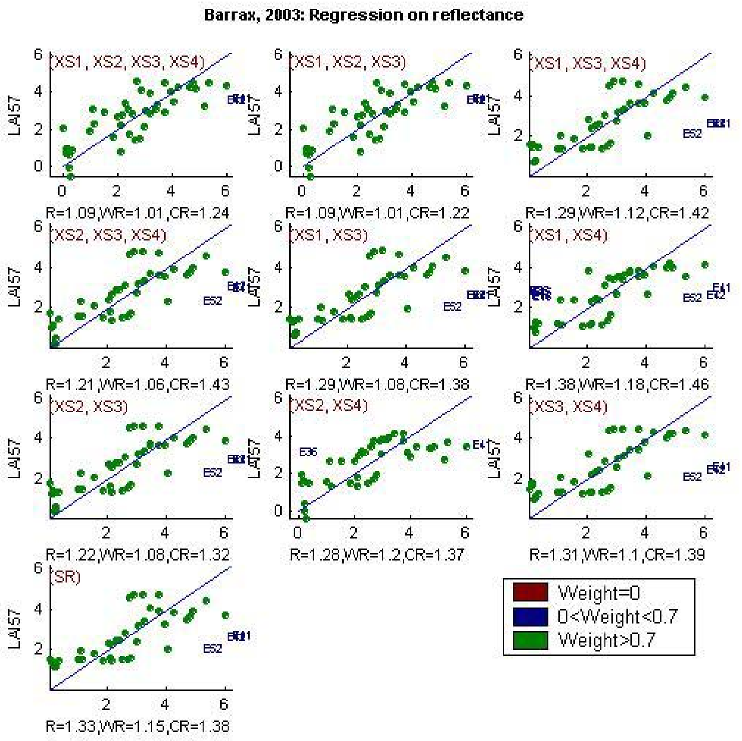

Figure 10.12. Effective Leaf Area Index at 57.5°: results for regression using different band combinations

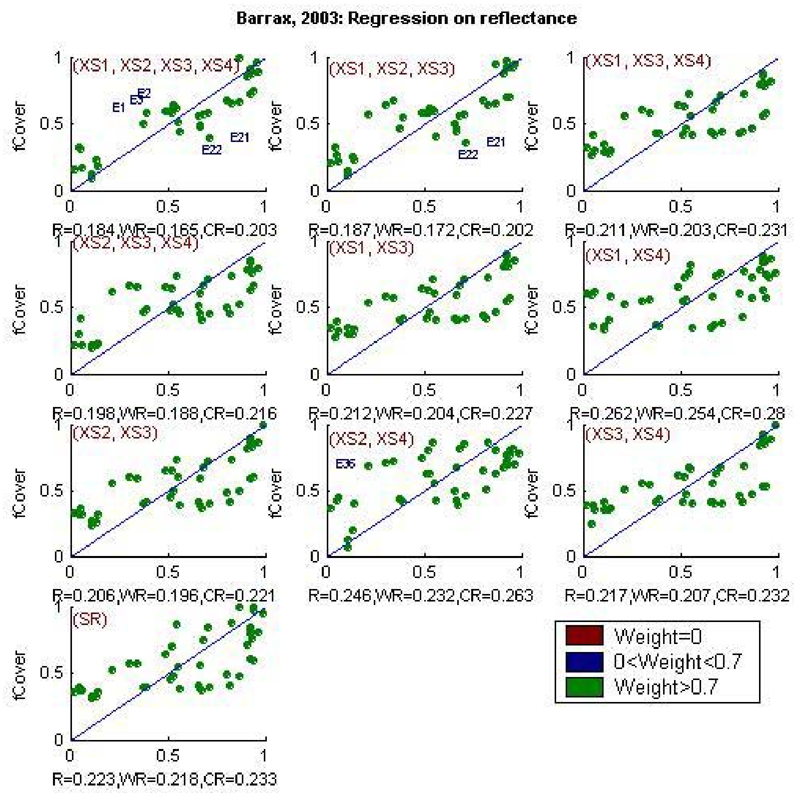

Figure 10.13. fCover: results for regression using different band combinations

Table 10.1. Transfer function applied to the whole site for the different biophysical variables, and corresponding errors

Variable	Band Combination	RMSE	Weighted RMSE	Cross-valid RMSE
Effective LAI	0.24 +99.21XS1-76.84XS2-2.31XS3+ 0.53XS4	1.06	0.97	1.20
Effective LAI (57.5°)	0.26+112.54XS1-83.51XS2-4.38XS3	1.09	1.01	1.22
fCover	-0.11-4.97XS2+1.88XS3+2.04XS4	0.20	0.19	0.22
fAPAR	0.14+12.35XS1-13.61XS2+0.15XS3+ 2.18XS4	0.17	0.16	0.20

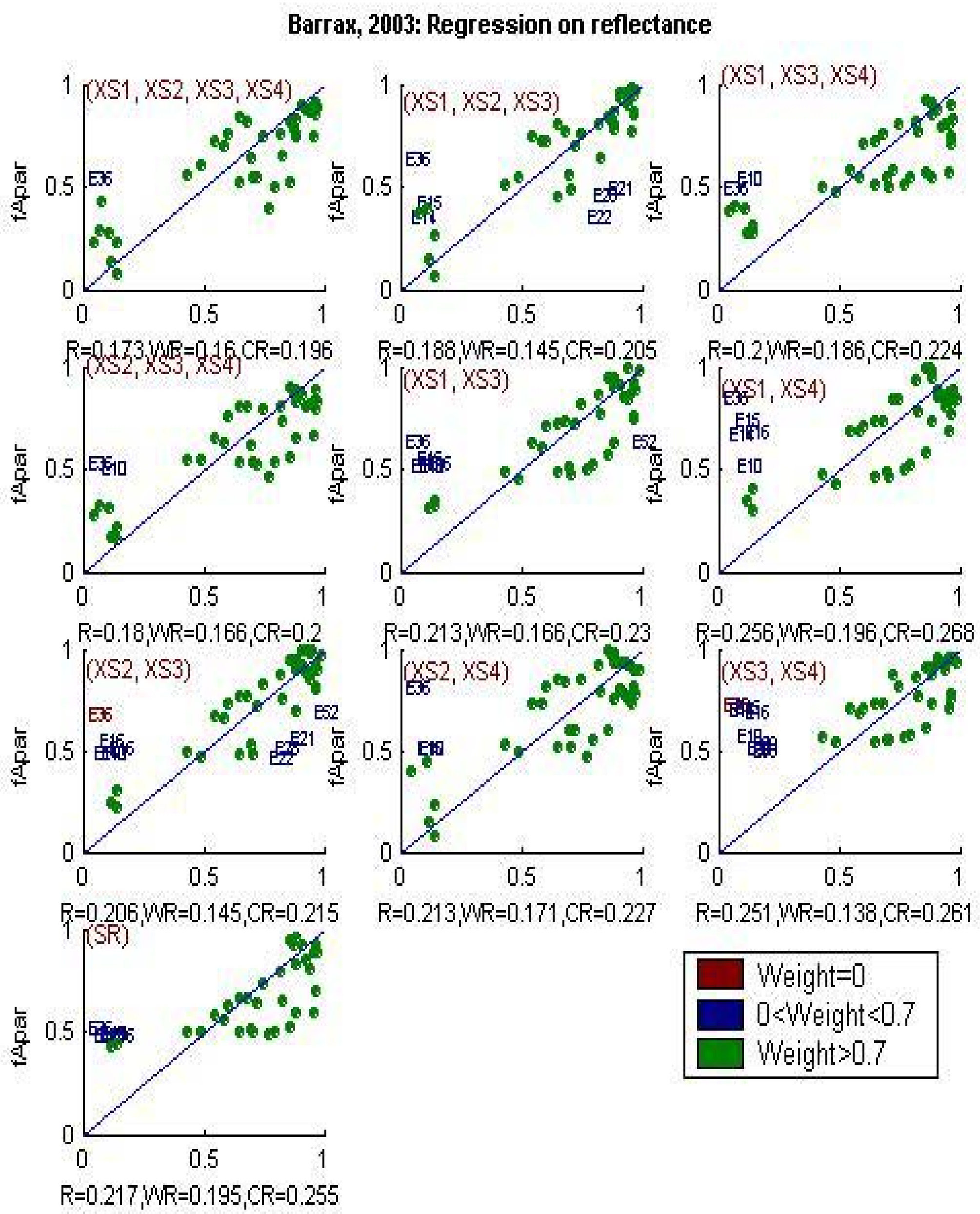

Figure 10.14. fAPAR : Results for regression using different band combinations

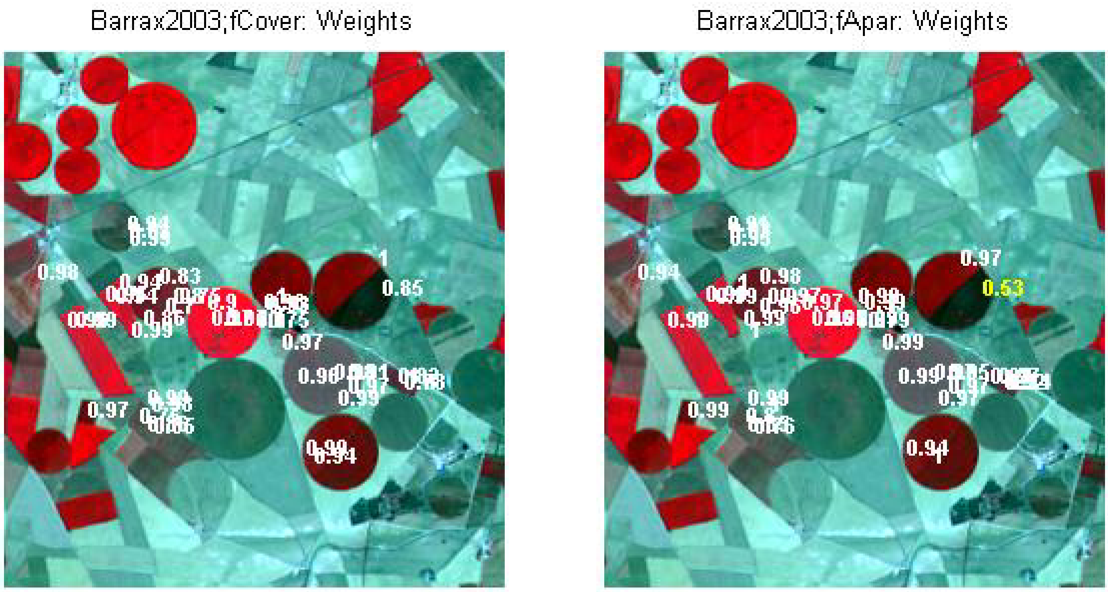

Figure 10.15. Weights associated to each ESU for the determination of fCover (left) and fAPAR (right) transfer function

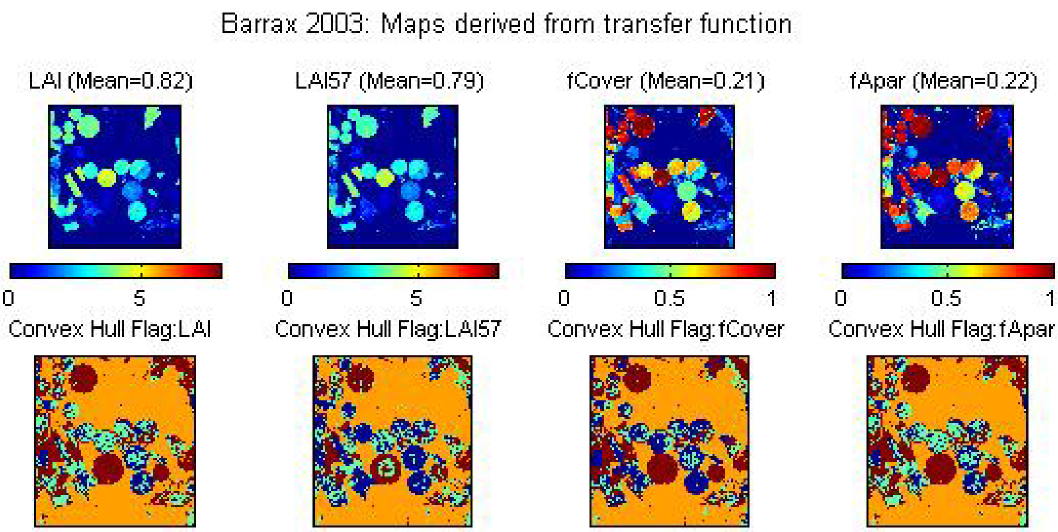

Figure 10.16. High resolution biophysical variable maps applied on the Barrax site (top). Associated Flags are shown at the bottom: orange corresponds to the bare soil class for which we applied the averaging method. dark blue and green corresponds to the pixels belonging to the 'strict' and 'large' convex hulls, and red to the pixels for which the transfer function is extrapolating.

10.3 Applying the transfer function to the Barrax SPOT image extraction

Figure 10.16 presents the biophysical variable maps obtained with the transfer function (REG) described in Table 10.1 for classes (1,2,4,5) and the AVE method for class 3. The maps obtained for the different variables are consistent, showing similar patterns, low LAI values where low fAPAR and fCover are observed and conversely. Note that the average value for LAI and LAI57 are consistent (around 0.8 for both).

The flag maps show also that a large part of the image corresponds to bare soil (55%) and that the transfer function is interpolating for 15% for LAI57, 21% for fCover and 23% for both LAI and fAPAR. These pixels correspond for a big part to two round fields located at the centre and the upper left corner of the image, with a red flag (Figure 10.16) for LAI, fCover and fAPAR. The field in the center presents a sort of dark green colour on the composite SPOT image (Figure 10.4) which corresponds to null LAI. The field at the upper left corner is represented in red in the composite SPOT image showing that dense vegetation can be observed. Figure 10.16 show that the LAI estimated for this field is quite high. Note that for LAI57, the centre of the field appears in blue and green flags, which means that the transfer function is used as an extrapolator for the other variables, but the extrapolation is closed to the boundaries of the convex hull.

10.4 Conclusion

The transfer functions are finally obtained by using Reg and 44 ESUs together for the pixel which do not belong to the bare soil class. A value of 0 was applied to bare soil pixels. For all the variables, the regression coefficients are computed by relating the variable itself to the reflectance. The band combinations are different from one regression to another. Results show good consistency between the variables and the flag associated to each map show that the transfer function is used as an extrapolator (red) in little areas or close to the boundaries of the convex-hull composed of the ESU pixel reflectance.

The biophysical variable maps are available in two projections:

- Plate carrée: latitude/longitude in WGS84 at 1.7857142857e-004° resolution
- UTM, 30N, WGS84 at 20m resolution.

The transfer function was applied on the SPOT image which was geo-located in UTM30N, WGS84. The resampling to obtain the plate carrée projection was performed using the nearest neighbour convolution to get consistent flags.

11 – ANALYSIS OF FIELD MEASUREMENTS OF BIOPHYSICAL PARAMETERS IN SPARC-2004: STATISTICAL AND SPATIAL VARIABILITY

The number of Elementary Sampling Units (ESUs) measured during SPARC-2004 for the biophysical parameters characterization of the different crops and number of measurements per ESU, as it was described in chapter 6 of Part-I (see Table 6.2.), were different depending on the biophysical parameter measured. The strategy scheme designed for each case was described with detail in chapter 6.

The biophysical parameters used for the characterization of the different crops were Dry Matter content (DM), Water Content (WC), Leaf Area Index (LAI) from LAI-Licor, Fractional Vegetation Cover (FVC) from hemispherical photographs and Chlorophyll Content (CC).

Once they were checked per ESUs, mean values per crops with the standard error were calculated to make possible the comparisson and characterization of the different biophysical parameters. Analysis has been focused on each parameter and its relationship with the rest of parameters in order to extract information from the different crops and by using combined data from SPARC-2003 and SPARC-2004 campaigns previously compared (in chapter 6 of this report) to assure robustness for results.

Figures 11.1 and 11.2 show results obtained from estimate mean values (DMC, WC, LAI and CC) for each field of the different crops meassured during SPARC-2004 with the standard error asociated. This estimation allows to do a first characterization for crops and to know the expected values for the parameters under study according to any specie.

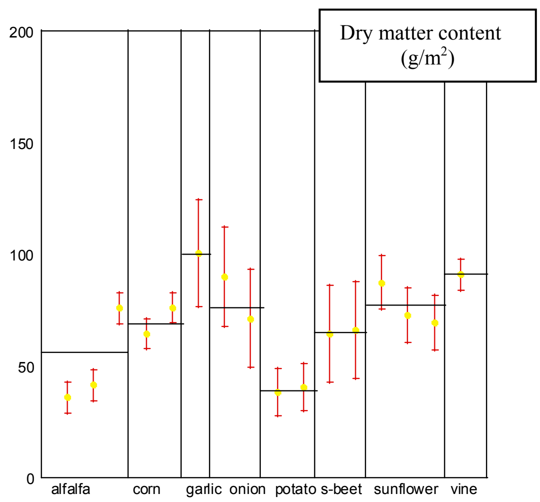

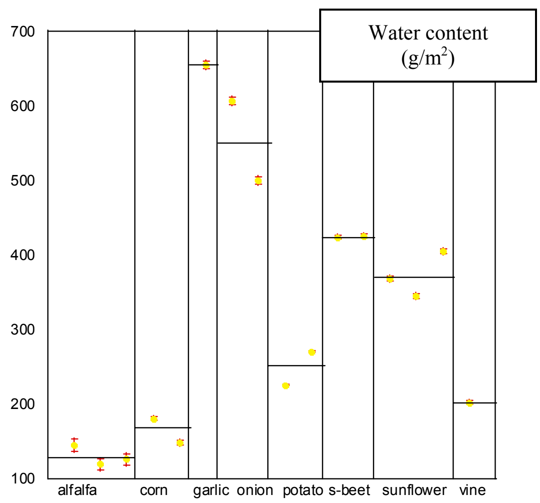

Figure 11.1. SPARC-2004 dry matter and water content data used in the analysis. Values correspond to mean of the ESUs measurements for each field with its standar error associated.

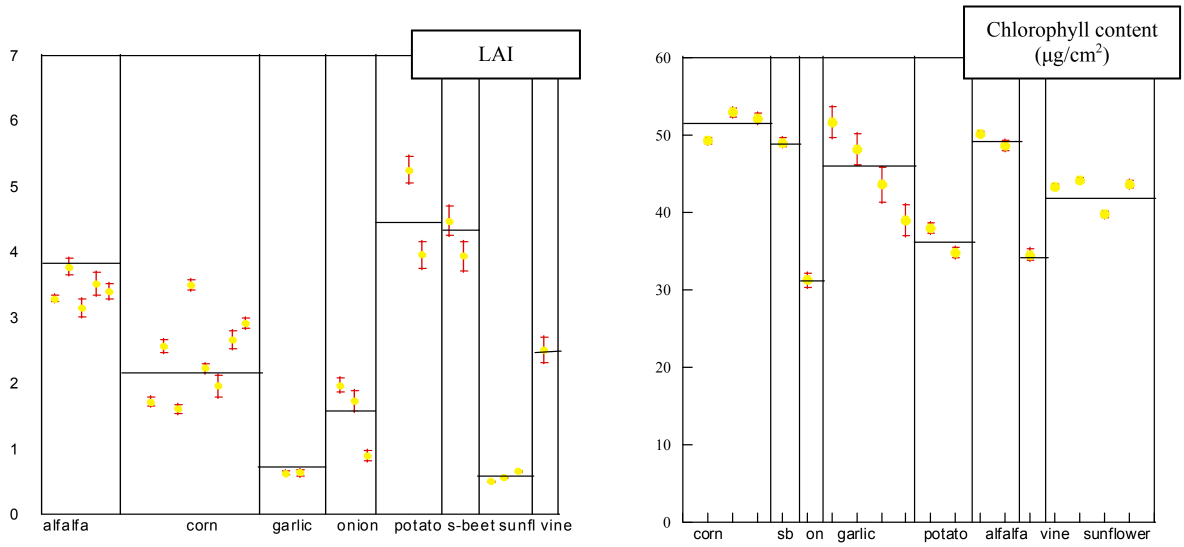

Figure 11.2. SPARC-2004 Leaf Area Index and Chlorophyll content data used in the analysis. Values correspond to the mean of the ESUs measurements for each field with its standar error associated.

For the FVC and LAI derived from the hemispherical photographs taken within an ESU, CAN-EYE software allowed obtaining these structural parameters of the canopy by estimating the gap fraction over the entire hemisphere, as it was described at 6.2.3 in this report. From this result, the true and effective LAI average were derived for this zenith range, and the FVC for the view zenith range of (0º-10º) and the standard deviation of the LAI estimated at the angle 57.5º. Figure 11.3 shows FVC and true LAI mean values with standard deviation obtained for the measured crops.

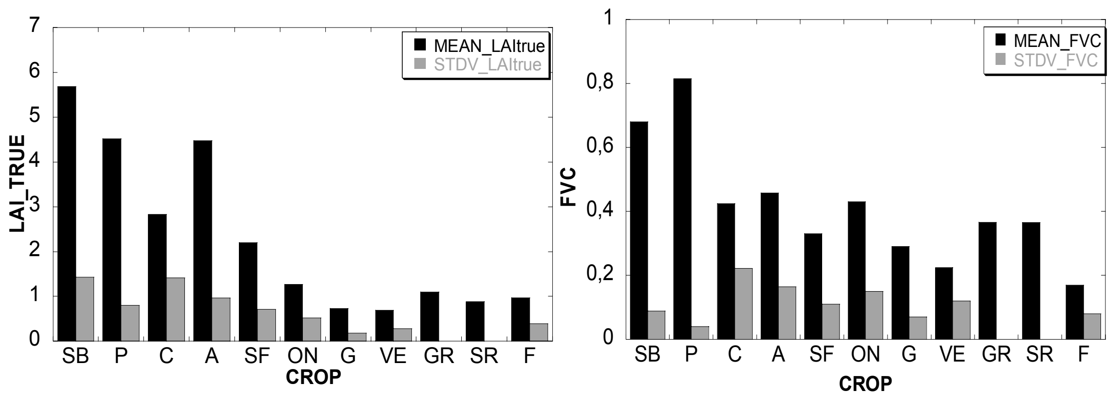

Figure 11.3. SPARC-2004 Leaf Area Index and Chlorophyll content data used in the analysis. Values correspond to mean of the ESUs measurements for each field with its standar error associated.

Mean (true and effective) LAI values have been compared to mean values measured by means of the LAI-LICOR in order to compare both methods. Figure 11.4 illustrates the results:

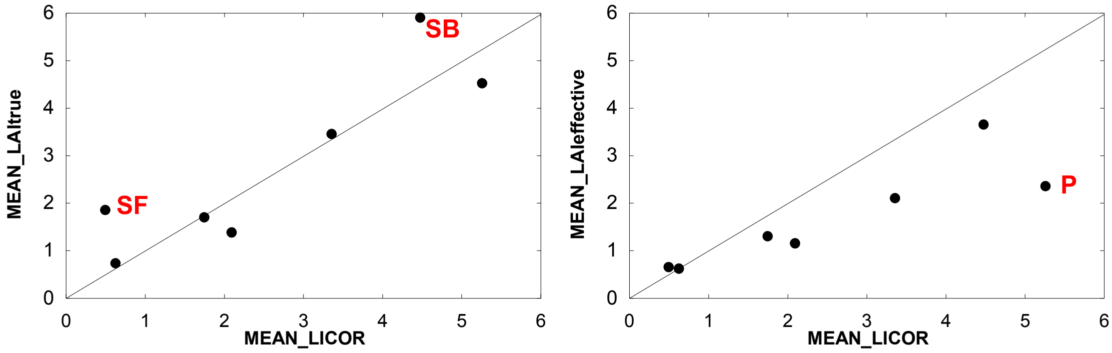

Figure 11.4. SPARC-2004 Leaf Area Index values from LAI-LICOR measurements compared to true and effective LAI outputs from the CAN-EYE shoftware.

In general, it can be observed that the mean true values are better correlated with the mean LICOR values except for the sunflower (SF) which shows a large relative error (see Figure 11.5). This difference is decreased when the effective values are considered and it can be observed an underestimation in the intermediate and dense vegetation canopies (corn C12, alfalfa A2, sugarbeet SB and potato P). The effective LAI correlates quite well for low vegetation canopies (garlic G1 and sunflower SF).

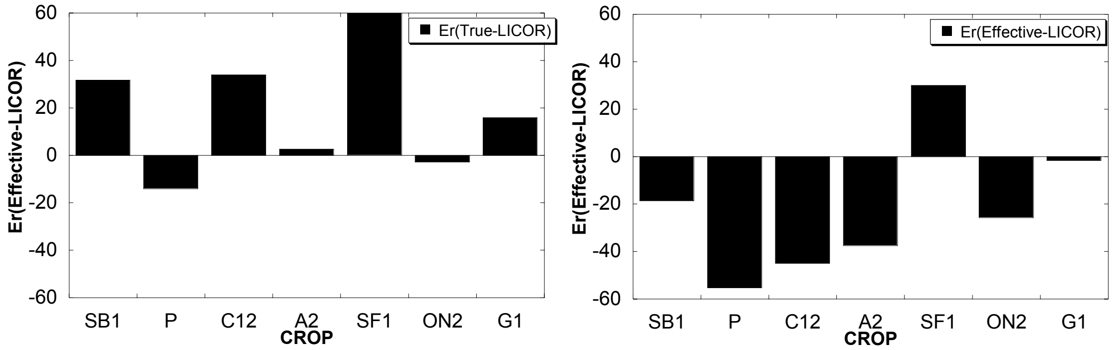

Figure 11.5. Relative error found between LICOR and true and effective LAI outputs.

FVC and true LAI results let to conclude that the hemispherical photographs method subestimes LAI values vs. LICOR measurements. Those differences can be corrected by using results from the comparison between 3D-reconstruction model described at 6.2.6 and CAN-EYE outputs (clumping, gap). True and effective LAI has been fitted to a linear function (Figure 11.6) and compared in order to estimate the infludence of the clumping output and a future task is to correct the discrepances after getting the clumpig from the 3D- recontruction model.

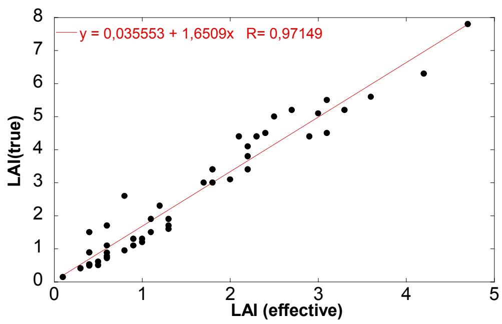

Figure 11.6. True and effective LAI outputs fitted to a linear fuction.

A second step of the analysis has been the characterization of the behavior of LAI, CC, WC and DMC by pairs for the crops measured during SPARC-2003 and SPARC-2004. The objective of this comparisson has been to understand the relationship that exist between the different parameters and extract information from crops for posterior development of vegetation models.
For this reason, the four parameters under study have been fitted to a linear function, as it can be seen in Figure 11.7.

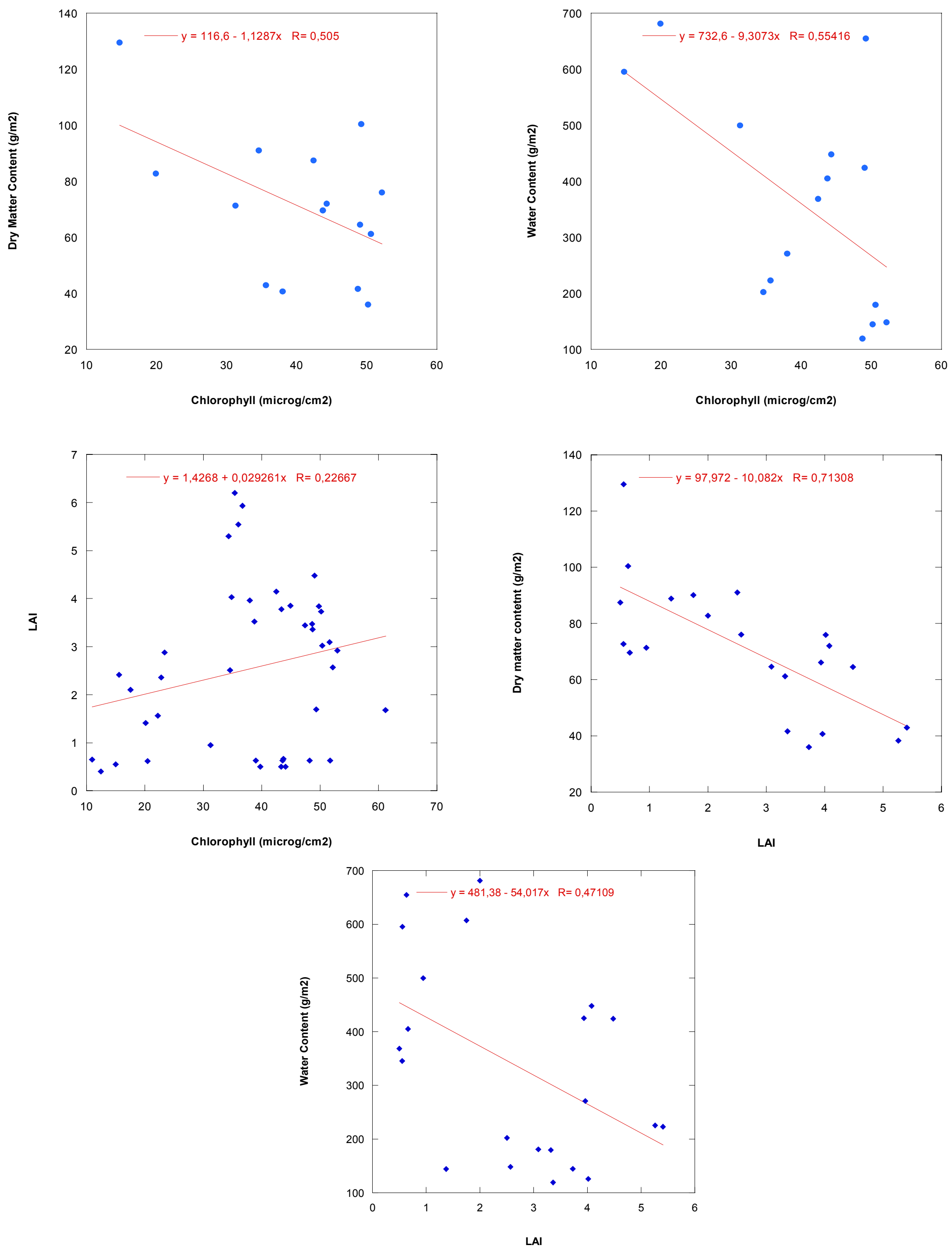

Figure 11.7. LAI, CC, WC and DMC measured for the crops fitted to a linear fuction by pairs.

The dispersion related to the linear function was as expected. The parameters that we are comparing are associated to mechanisms of the plant completely different and this fact justifies these first results. A second analysis has been conducted to check each measurement and, on one hand, to assure the similar behavior for points which correspond to the same crop from the two SPARC campaigns, and on the other hand, to identify the range of values related to each crop for their characterization.

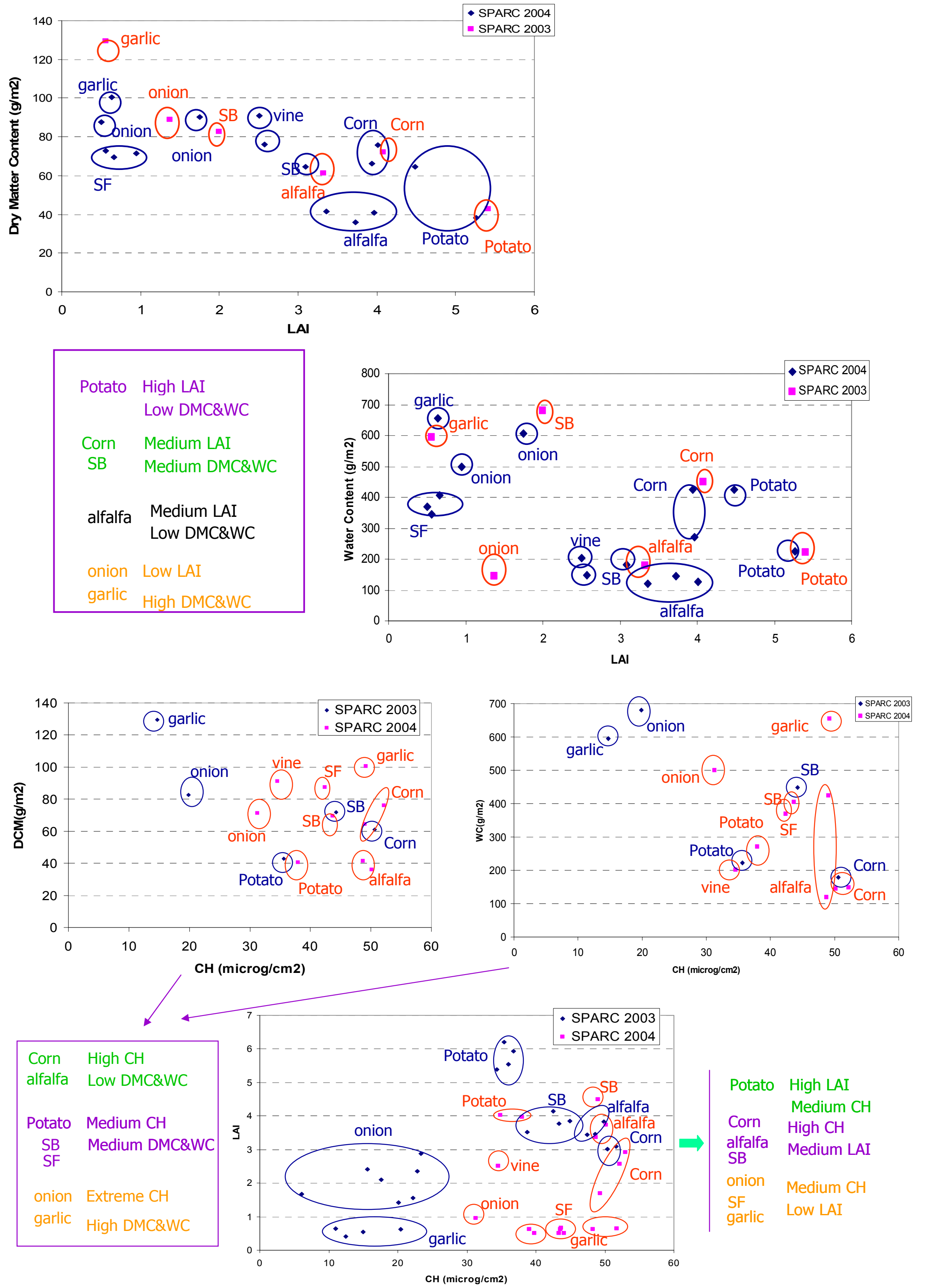

Figure 11.8. SPARC-2003 and SPARC-2004 combined measurements and LAI, CC, WC and DMC characterization.

Figure 11.8 ilustrates results of this second analysis: Points are clarely grouped per crops for the two years and relationship between the biophysical parameters identified for each crop.

Our objectives for future work will be focused on a more exhaustive statistical analysis of variability once SPARC-2004 and SPARC-2003 measurements of biophysical parameters have been analysed. Retrievals from acquired imaging data, CHRIS-PROBA and MERIS, will let to analyse multiscale effects. Furthermore outputs from hemispherical data (ALA, clumping) will be calculated by applying 3D-methodology in order to correct the observed differences between true LAI and effective LAI results.

PART III- Data Base

12 – SPARC-2004 GENERIC CAMPAIGN DATA BASE

A new activity incorporated in SPARC-2004 campaign was the use of the SPARC-2004 data as a "real world" test for the newly developed ESA Campaign Data Base (ESA-CDB) that will collect all the data from ESA supported field campaigns.

The SPARC-2004 CDB is a generic Campaign Data Base that will hold both selected satellite data sets and data from groundbased measurements and computations. Common data definitions (naming conventions and definitions for data and metadata elements) are essential for such complex data exchange. The data definitions constitute a common language, which ensures that the indexing and search terms are subject to one common interpretation by all participants.

12.1 CDB objectives

The campaign database shall provide an online information system that supports users in managing and exploiting campaign datasets for Earth Observation missions and applications. In a more future perspective the overall aim is to provide a data centre that handles Cal/Val data, satellite data and campaign data in an integrated way. This type of integration will provide an add-on value to all types of measurements, as the data centre becomes a one-stop source to look for data. The centre will in this way increase the dissemination potential for all classes of data. The database is built with a strict quality control of incoming data and options for individual file-formatting are very limited. CDB aims to increase the use of geophysical data after a campaign is completed. Measurements are made available for other scientists (only after permission is given from original PI) CDB provides the final archive for the data. Another advantage in using the CDB is the possibility of sharing data within the campaign consortium – both during the campaign and in the analysis phase.

Currently, most of the SPARC-2004 data is stored in CD/DVD. When completed, database will be accessible from:

- FTP server
- Project Web page

ESA selected the HDF 4.1r3 file format for the file exchange, based on the established use of this format within ESA and some of the user groups. It will include data from all future ESA campaigns.
Actually we are in the demonstration phase and data from some ESA campaigns is being inserted into the system (CDB website **http://ariane.nilu.no/cdb/**).

12.2 Specific process to input data into the CDB

The system components are here described in a logical order when we follow a data file as it passes from the originator (DO) to the data submitter (DS) that converts it to the proper format, then into the storage and forward to an end-user. Figure 12.1 shows a schematic diagram of how the various components are connected.

The data originator (DO) is the person involved in the acquisition or generation of the data and/or who performs post processing of measurements or numerical simulations. This person has detailed knowledge about the data, therefore has the proper condition to fill the metadata related to the measurements. The DO is responsible for the quality of the data and for providing the data and metadata to the Data Submitters (DSs). An EXCEL template has been prepared in order to make the metadata fill up process easier. Any problem or requirement about this task should be addressed to the DSs, who will try to solve it adequately.

The data submitter (DS) is the person responsible for formatting of HDF files and upload of data to the data centre. This person should preferably be someone with a scientific knowledge of the data. The DS has to know how to use the data centre, as explained in the previous section, but additional information is needed in order to start formatting of data files.

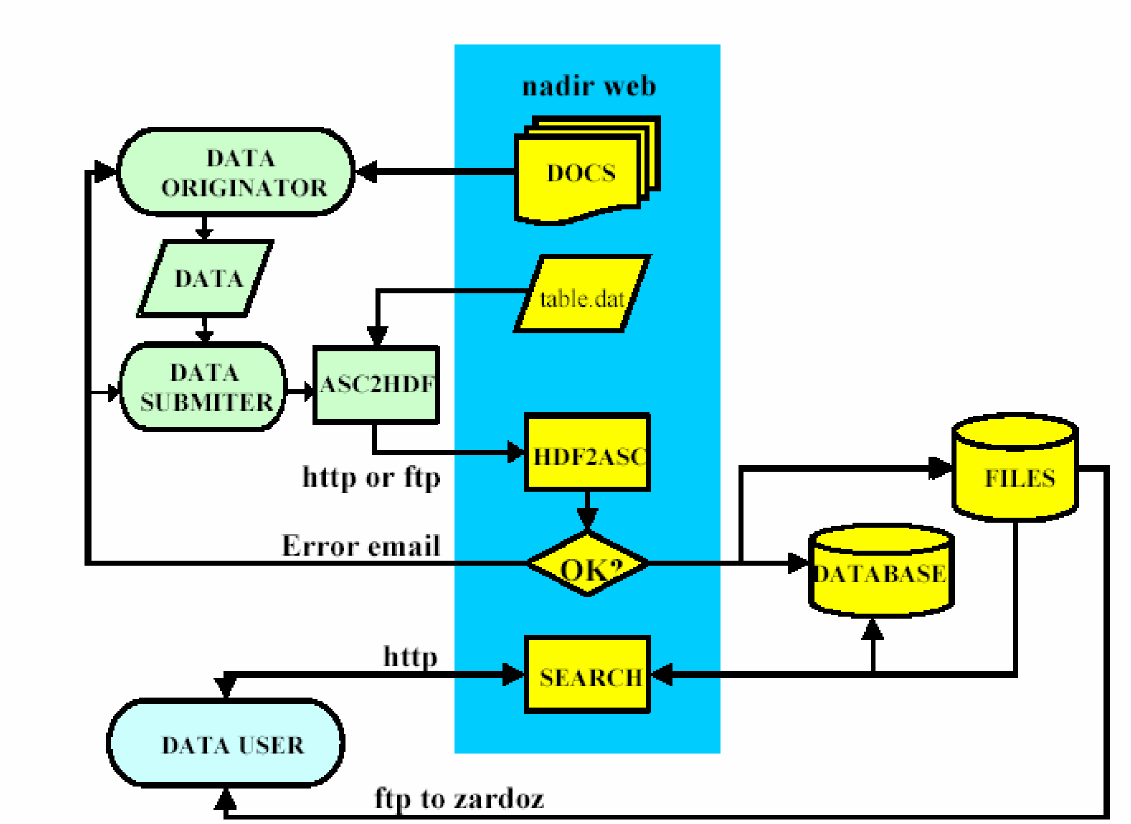

Figure 12.1. Diagram of the CDB system components

For the SPARC2004 campaign the DSs are:

- Luis Alonso from LEO group at University of Valencia
  luis.alonso@uv.es

- Julia Amoros from GPDS group at University of Valencia
  julia.amoros@uv.es

- Luis Gomez-Chova from GPDS group at University of Valencia
  luis.gomez-chova@uv.es

Anyone involved in the project can consult the data stored in the data base, and are considered as Data Users, with access to the search interface and possibility to plot or download data. A user-name and password is needed.

The main end-user tool on this site is the “Search Data” page, which allows the user to sort through the data files with advanced criteria selections (**http://ariane.nilu.no/cdb/restricted/index.cfm?fa=search.showSearchForm)**. Filtering by data supplier, project, location, data source, data type, component and other metadata elements is supported. Data files may also be filtered by a “4-D box algorithm” (any file with data relevant for a given geographical location and time). Furthermore, files can be filtered by submission date and update status. Metadata content in various files can be browsed on-line and plots can be generated to visualise data content. An example of this is shown in Figure 12.2.

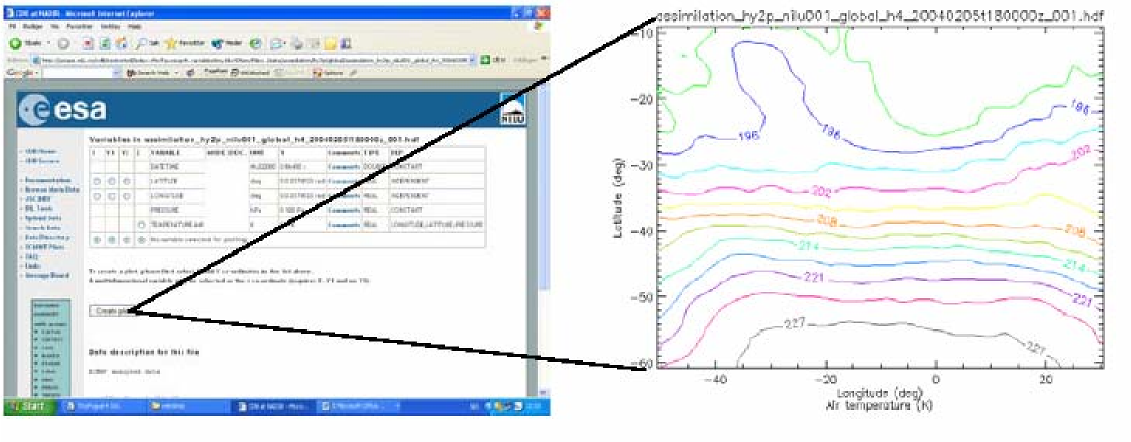

Figure 12.2. An example of the search interface data base for data users.

All data files that match the search criteria are listed in a new web page, with links to HDF data file download, to comments, and to a variable list. In the variable list page the user may select variables and generate an on-line plot. In the file list the user may also select multiple files for download as a tar-ball. The user may save the search criteria in the index database for convenient re-use at a later time. A new feature of CDB was the implementation of Project Internal Pages (PIP), where users may share campaign specific information through a web-portal. The PIP is available at http://www.nilu.no/pipdev and contains sections for documents, a link archive, contact information, an image gallery and a discussion board. A user account is also needed to access these pages.

CDB Advantages:

- Extensive search criteria of data files: by project, by originator, by data variables, by location, by time, etc.
- Preview of simple plots, data variables and comments.
- Download a single data file or a large set of zipped files.

12.3 SPARC Requirements

Main requirements, not allowed by the present CDB, in order to include SPARC data were the following:

- To include binary data besides the ASCII file.
- To declare new instruments (DATA_SOURCE) and new measurements (DATA_VARIABLES) not included in CDB
- To include data acquired with no homogeneous sampling
- To use labels (sites) instead of the mandatory variables DATETIME, ALTITUDE, LATITUDE and LONGITUDE
- To include pictures and files with no numerical data.

12.4 SPARC Template and Conversion Tool

Filling all the metadata of the CDB with its proper format is not straight forward but is mandatory and an interactive user interface is currently under development (NILU), but it is not ready yet. A generic Excel-Template (see Figure 12.3) has been created by the *DS team* to make this task easier in SPARC-2004. The information is converted by a VB-macro from this template into the proper data and metadata files.

C4 | University of Valencia, Facultad de Fisica;UVAL.FISICA

	A	B	C	D
1	***Metadata Category***	***Section***	***Entry***	***Comments…***
2				
3	*PI_NAME*	4.1.1	Moreno; Jose	Principal Investigator's (PI) Name. The PI has the main scientific and/or institutional responsibility for the given data. Format: **Family name; Given Name**
4	*PI_AFFILIATION*	4.1.2	University of Valencia, Facultad de Fisica;UVAL.FISICA	Principal Investigator's official affiliation name and affiliation acronym. **Select from list.**
5	*PI_ADDRESS*	4.1.3	Istituto di Metodologie per l'Analisi Ambientale del CNR;CNR.IMAA Instituto Tecnico Agronomico Provincial (Albacete);ITAP Laboratoire des Sciences de l'Image, de l'Informatique et de la Télédéte	Principal Investigator's official mailing address. Format: **Address; Postal code; Country name**
6	*PI_EMAIL*	4.1.4	Universidad de Castilla-La Mancha;UCLM Università degli Studi di Napoli "Federico II";USN	Principal Investigator's e -mail address.
7	*DO_NAME*	4.1.5	University of Valencia, Facultad de Fisica;UVAL.FISICA University of Valencia, Escuela Tecnica Superior de Ingenieria;UVAL.ET University of Washington;UWAS	Data Originator's (DO) Name. The person that has performed the measurements. Format: **Family name; Given Name**
8	*DO_AFFILIATION*	4.1.6	University of Valencia, Facultad de Fisica;UVAL.FISICA	Data Originator's official affiliation. **Select from list.**
9	*DO_ADDRESS*	4.1.7	Dpto. Termodinamica, C/Dr Moliner 50; 46100 Burjassot; Spain	Data Originator's mailing address. Format: **Address; Postal code; Country name**
10	*DO_EMAIL*	4.1.8	luis.alonso@uv.es	Data Originator's e -mail address
11	*DS_NAME*	4.1.9	Alonso;Luis	
12	*DS_AFFILIATION*	4.1.10	University of Valencia, Facultad de Fisica;UVAL.FISICA	
13	*DS_ADDRESS*	4.1.11	C/ Dr. Moliner, 50; 46100 Burjassot; Spain	
14	*DS_EMAIL*	4.1.12	luis.alonso@uv.es	
15				
16	*DATA_DESCRIPTION*	4.2.1	Radiometric measurements of ground targets for calibration purposes	A brief sentence describing the data content. (**Free Format**)
17	*DATA_DISCIPLINE Field*	4.2.2a	LAND.SURFACE.GEOPHYSICS	Field of research to which the data in the file belongs. **Select from the list.**
18	*DATA_DISCIPLINE Class*	4.2.2b	INSITU	Class to which the data in the file belongs. **Select from the list.**
19	*DATA_DISCIPLINE Subclass*	4.2.2c	GROUNDBASED	Subclass to which the data in the file belongs. **Select from the list.**
20	*DATA_DISCIPLINE*	*4.2.2*	LAND.SURFACE.GEOPHYSICS;INSITU ;GROUNDBASED	
21	*DATA_GROUP Type*	4.2.3a	EXPERIMENTAL	Origin of the data (experimental or model or a combination of both). **Select from the list.**
22	*DATA_GROUP Subtype*	4.2.3b	SCALAR.MOVING	Spatial characteristics of the data. **Select from the list.**
23	*DATA_GROUP*	*4.2.3*	EXPERIMENTAL;SCALAR.MOVING	

Global Attributes / Variable Attributes / Hoja1

Figure 12.3. Generic Excel-Template created by the *DS team* to SPARC-2004 CDB.

12.5 Project Internal Pages (PIP)

CDB Project Internal Pages are the dedicated website for each ESA campaign On-line interchange of data/knowledge about SPARC campaign and is available at http://www.nilu.no/pip (username and password have been delivered to all responsibles). Contents and sections that it can be found are:

- ✓ Documents Section: Any campaign member is allowed to upload
  - Working Files
  - Data Collection Reports
  - Documentation related to the Campaign Data Base
  - SPARC Experimenter Handbooks
- ✓ Related Links: VALERI, CHRIS/PROBA, … web pages
- ✓ Contact information: Email and telephone of all SPARC members
- ✓ Image gallery: Upload pictures, plots, maps…
- ✓ Forum: Discuss matters, comments, and doubts about anything related to SPARC or the ESA-CDB**.**

Documentation of data is essential to obtain maximum reuse of data after the campaign is finished. For this purpose, we recommend the data submitters to report as much metadata as possible in the actual data files. The structure of CDB offers plenty of possibilities to report both general file metadata and specific information on each variable. Secondly, it is important also to store an overview and any additional information of the campaign data in the Project Internal Pages (PIP).

The PIP has been set up by the campaign data manager together with NILU, and will typically contain a section for documentation connected to the campaign. The PIP is accessed with a user-name and password that is common to all member of a specific campaign. The campaign data manager will arrange the "documents" section of the PIP into sub-folder as needed, and the entire campaign member will be able to upload any type of files through this system. In addition to documents, the PIP is a natural place to put contact information and links to external key resources on the Internet. A discussion board is available and an image gallery allows users to upload pictures, plots, maps, etc. to the web pages. Users are encouraged to use the PIP before, during and after the campaign.

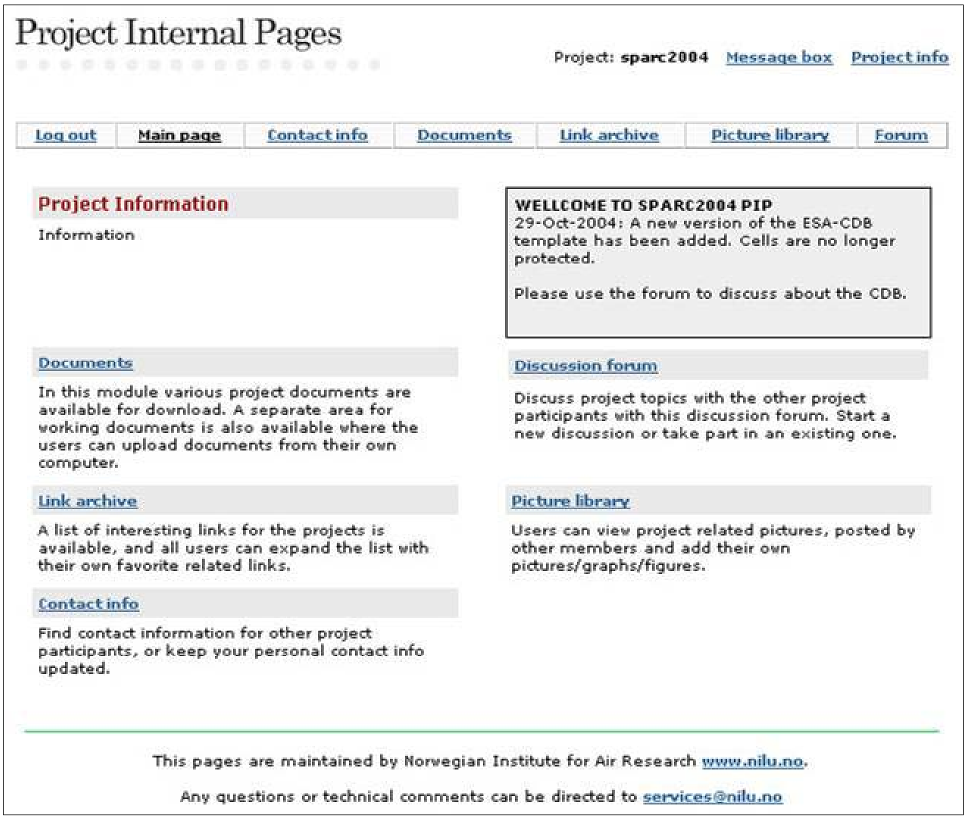

12.6 Main Risks and Contingency Plans

The amount of data of SPARC is huge and the specificity of the metadata format does the input process slow and hard. Furthermore this specifity on the format implies DOs need training in order to fill properly the template and *DS team* should not correct mistakes in all template files. For these reasons two contingency plans has been propoused by the *DS team* and follow the next scheme:

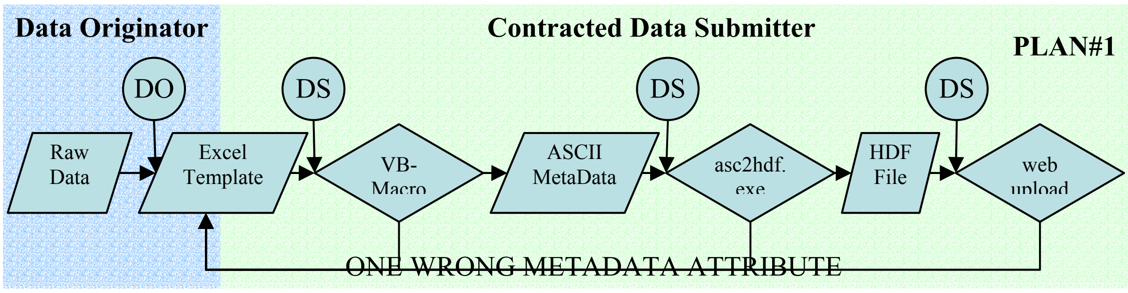

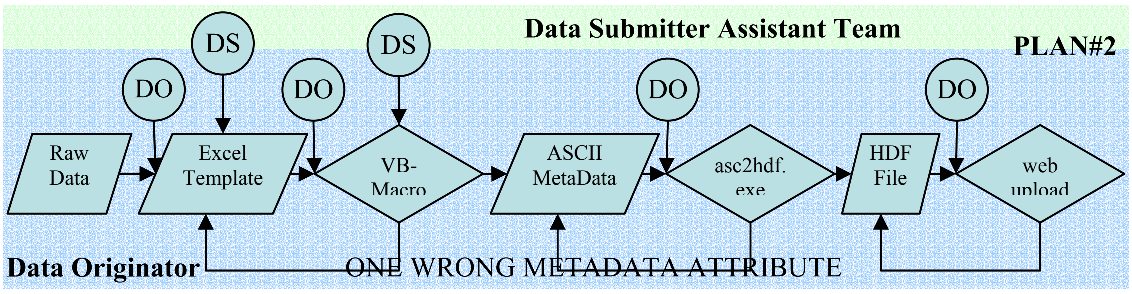

The first one implies Dedicated *DS* must be a contractual element to input all data files into CDB and to assist the *DO*s. A second plan suggests *DO*s must be DSs using the SPARC template and the Nilu conversion tool and the present *DS team* will be the *DS assistant team* helping the DOs when necessary.

Conclusions

SPARC-2004 is the first campaign that makes use of the CDB for data storage as part of the campaign design. Because of that the structure for the work distribution is not yet well defined. This is the first time that CDB is used under real conditions and it will be a powerful instrument of information exchange among researchers. Although CDB kernel is completed, the definition and introduction of data is in an improvement stage. We must use a provisional CDB interface that is rudimentary and time consuming. Although not all the acquired data campaign will be available in the CDB, a significant amount of data, representative of all the data set, will be collected in the SPARC-2004 CDB.

REFERENCES

ANNAN A.P., 1977. Time-domain reflectometry air gap problem for parallel wire transmission lines. Geol. Survey of Canada, paper 77-IB, pp. 59-62.

BARET, F., WEISS, M., LEROY, M., ALLARD, D., GARRIGUES, S., BOHBOT, H., BOSSENO, R., BELLA, C.D., ESPANA, M., GOND, V., GUINOT, J.-P., GUYON, D., LELONG, C., MOUGIN, E., NILSON, T., VINTILLA, R. 2004. VALERI: a network of sites and a methodology for the validation of land satellite products. Remote Sensing of Environment. (in press).

BAKER J.M. and LASCANO R.J., 1989 - The spatial sensitivity of time-domain reflectometry. Soil Sci., 147: 378-384.

BAKER J.M. and ALLMARAS R.R., 1990 - System for automating and multiplexing soil moisture measurement by Time-domain reflectometry. Soil Sci. Soc. Am. J., 54: 1-6.

BAKER J.M. and LASCANO R.J., 1991 - Response to the letter to the editor. Soil Sci, 151: 256-257.

CHEN, J. M., CIHLAR, J., 1995. Quantifying the effect of canopy architecture on optical measurements of leaf are index using two gap size analysis methods. IEEE Transaction of Geoscience and Remote Sensing, 33: 777-787.

DALTON F.N. and VAN GENUCHTEN M.Th., 1986 - The time - domain reflectometry method for measuring soil water content and salinity. Geoderma, 38: 237-250.

DE BRUIN, H.A.R., B.J.J.M. VAN DEN HURK AND W. KOHSIEK, 1995, The scintillation method tested over a dry vineyard area, Boundary-Layer Meteorol., 76: 25-40.

DEAN T.J., BELL J.P. and BATY A.J.B., 1987 - Soil moisture measurement by on improved capacitance technique: I. sensor design and performance. J. Hydrol., 93: 67-78.

D'URSO G., 1992 - Impiego della riflettometria in dominio temporale (TDR) per la misura del contenuto d'acqua dei suoli in presenza di profili di umidità non uniformi - Rivista di Ingegneria Agraria, 23, 35-44.

D'URSO G., MANCINI M. and SANTINI A., 1994 - Satellite S.A.R. data sensitivity to soil dielectric and moisture patterns. Proc. XII World Congress on Agricultural Engineering, CIGR, Marelbeke, Belgium, vol.I: 35-43.

D'URSO G., COPPOLA A., SANTINI A., 1996 - Spatial and temporal variability of soil dielectric patterns on the Sele test site.. Proceed. 2nd Workshop on "Spatial and Temporal Soil Moisture Mapping (Proj. EV5V-CT94-0446), Rennes, giu.'95; Lab. Hydrology, Gent University (Belgium)

F.MOLERO, L.NÚÑEZ, M.PUJADAS AND F.JAQUE, "Design of a differential absorption lidar (DIAL) system and assessment of its performance" Anales de Fisica 95 pp 229-239, 2000.

HASTED J.B., 1973 - Aqueous dielectrics. Chapman and Hall Ltd. London, pp.302

HAYHOE H.N., TOPP G.C. and BAILEY W.G., 1983 - Measurement of soil water contents and frozen soil depth during a thaw using time-domain reflectometry. Atnas-Ocean, 21: 299-311.

HEIMOVAARA T.J., 1993 - Design of triple-wire time domain reflectometry probe in practice and theory. Soil Sci. Soc. Am. J., 57: 1410-1417.

HEIMOVAARA T.J. and BOUTEN W., 1990 - A computer controlled 36-channel time domain reflectometry system for monitoring soil water content. Water Resour. Res., 26: 2311-2316.

HEIMOVAARA T.J., BOUTEN W. and VERSTRATEN J.M., 1994 - Frequency domain analysis of time domain reflectometry waveforms 2. A four-component complex dielectric mixing model for soils. Water Resour. Res., 30: 201-209.

HERKELRATH W.N., LIAMBURG S.P. and MURPHY F., 1991 - Automatic, real - time monitoring of soil moisture in a remote field area with time domain reflectometry. Water Resour. Res., 27: 857-864.

HILHORST M.A. and DIRKSEN C., 1994 - Dielectric water content sensors: Time-Domain versus Frequency-Domain, personal communication

HOKETT. S. L., CHAPMAN J.B. and CLOUD S. D., 1992 - Time domain reflectometry response to lateral soil water content heterogeneities. Soil Sci. Soc. Am. J., 56: 313-316.

HOEKSTRA P. and DELANEY A., 1974 - Dielectric properties of soil at VHF and microwave frequencies. J. Geophys. Res, 79: 1699-1708.

JACOBSEN O.H. and SCHJØNNING P., 1995 - Comparison of TDR calibration functions for soil water determination. In A.Correll (Ed.); Proceed. Symposium on TDR applications in Soil Science, Foulum (D) 1994; Danish Institute of Plant and Soil Sci.,SP Report n.11 Vol.3: 25-33

KACHANOSKI R.G., NAN WESENBEECK I.J., VON BERTOLDI P., WARD A. and HAMLEN C., 1990 - Measurement of soil water content during three - dimensional axial - symmetric water flow. Soil Sc. Soc. Am. J., 54: 645-649.

KNIGHT J.H., 1992 - Sensitivity of time domain reflectometry measurements to lateral variation in soil water content. Water Resour. Res., 28: 2345-2352.

KUTÍLEK M. and NIELSEN D.R., 1994 - Soil hydrology. CATENA VERLAG, Germany, 370 pp.

MANCINI M., GIACOMELLI A., TROCH P. and D'URSO G., 1994 - Remote sensing of surface soil moisture from spaceborne SAR sensors over the Sele plain. Proceed. The European Symposium on Satellite Remote Sensing, Europto, 26-30 sett. 1994, C.N.R., Roma; SPIE, Bellingham, Washington 98227-0010 (U.S.A.); Vol.2314: 516-523

MARTÍNEZ, B., BARET, F., CAMACHO-DE COCA, F., GARCÍA-HARO, F.J., VERGER, A., AND.MELIÁ, J. 2004a. Validation of MSG vegetation products. Part I: Field retrieval of LAI and FVC from hemispherical photographs. Remote Sensing for Agriculture, Ecosystem and Hydrology. SPIE. (in press)

M.M. MILLAN, B. ARTÍÑANO, L. ALONSO & M. NAVAZO "The effects of meso-scale flows on regional and long-range atmospheric transport in the western mediterranean area". Atm. Environ.25A 949-963 (1991)

NADLER A., DASBERG S. and LAPID I, 1991 - Time domain reflectometry measurements of water content and electric conductivity of layered soil columns. Soil Sci. Soc. Am. J., 55: 938-943.

NIELSEN D.C., LAGAE H.J., ANDERSON R.L., 1995 - Time-Domain Reflectometry measurements of surface soil water content. Soil Sci. Soc. Am. J., 59: 103-105

R.A. Mc CLATCHEY, M.J. BOLLE, K.Ya. KONDRATYEV, "A preliminary cloudless standard atmosphere for radiation computation", Boulder, Colorado, U.S.A. (1982).

ROTH, SCHULIN R. FLUEHLER H. and ATTINGER W., 1990 - Calibration of TDR for water content measurement using a composite dielectric approach. Water Resour. Res., 26: 2267-2273.

ROTH C.H., MALICK M.A. and PLAGGER., 1992 - Empirical evaluation of the relationship between soil dielectric constant and volumetric water content as the basis for calibrating soil moisture measurements by TDR, - J. Soil. Sci, 43: 1-13.

RUBIO, E., CASELLES, V., COLL, C., VALOUR, E. AND SOSPEDRA, F., 2003, Thermal–infrared emissivities of natural surfaces: improvements on the experimental set-up and new measurements, Int. J. Remote Sensing, 24, 5379–5390.

SHAUN F.K., SELKER J.S. and GREEN J.L., 1995 - Using short soil moisture probes with high - bandwidth time domain reflectometry instruments. Soil Sci. Soc. Am. J., 59: 97-102.

SHUMUGGE T.J., JACKSON T.J. and MCKIM H.L., 1980 - Survey of methods for Soil moisture determination. Water Resour. Res., 16: 961-979.

SPAANS E.J.A. and BAKER J.M., 1993 - Simple baluns in parallel probes for Time Domain Reflectometry. Soil Sci. Soc. Am. J., 57: 668-673

TOPP G.G., DAVIS J.L. and ANNAN A:P., 1980 - Electromagnetic determination of soil water content measurements in coaxial transmission lines. Water Resour. Res., 16: 574-582.

TOPP G.C. and DAVIS J.L., 1985 - Time - domain reflectometry (TDR) and its application to irrigation scheduling. Advance in irrigation, vol.3 (Hillel D. ed.), Academic Press. Inc. New York pp. 107-127.

TOPP G.C., YANUKA M., ZEBCHUK W.D. and ZEGELIN S., 1988 - Determination of electrical conductivity using time Domain Reflectometry soil and water experiments in coaxial lines. Water Resour. Res., 24: 945-952.

WHALLEY W.R., 1993 - Considerations on the use of time-domain reflectometry (TDR) for measuring soil water content. Journal of Soil Science, 44: 1-9

WORLD METEOROLOGICAL ORGANIZATION (CAS)/RADIATION COMMISSION OF IAMAP. Meeting of experts on aerosols and their climatic effects, WCP 55, Williamsburg, Virginia, U.S.A., 28-30 March 1983

ZEGELIN S.J. and WHITE I., 1989 - Improved field probes for soil water content and electrical domain reflectometry. Water Resour. Res., 25: 2367-2376.

ZEGELIN S.J., WHITE I. and RUSSEL G.F., 1992 - A critique of the time domain reflectometry technique for determining field Soil - water content, in "Advances measurement of soil physical properties: bringing theory into practice (Topp G.C., Reynolds W.R. and Green R.E. ed.). Soil Sci Soc. Am. publ. n°30, Madison, Wisconsin, USA